The University of Maine
DigitalCommons@UMaine

Electronic Theses and Dissertations | Fogler Library

2001

Current Voltage Characteristics of a Semiconductor Metal Oxide Sensor.

Huilin Ren

Follow this and additional works at: http://digitalcommons.library.umaine.edu/etd

Recommended Citation
Ren, Huilin, "Current Voltage Characteristics of a Semiconductor Metal Oxide Sensor." (2001). *Electronic Theses and Dissertations*. 371.
http://digitalcommons.library.umaine.edu/etd/371

This Open-Access Thesis is brought to you for free and open access by DigitalCommons@UMaine. It has been accepted for inclusion in Electronic Theses and Dissertations by an authorized administrator of DigitalCommons@UMaine.

Current Voltage Characteristics of a Semiconductor Metal Oxide Sensor

By

Huilin Ren

B.S. Shandong University of Technology, China, 1996

A THESIS

Submitted in Partial Fulfillment of the

Requirements for the Degree of

Master of Science

(in Electrical Engineering)

The Graduate School

The University of Maine

August, 2001

Advisory Committee:

John F. Vetelino, Professor of Electrical & Computer Engineering, Advisor

Brian G. Frederick, Assistant Professor of Chemistry

David E. Kotecki, Associate Professor of Electrical & Computer Engineering

CUURRENT VOLTAGE CHARACTERISTICS OF A SEMICONDUCTOR METAL OXIDE SENSOR

By Huilin Ren

Thesis Adviser: Dr. John F. Vetlino

An Abstract of the Thesis Presented

in Partial Fulfillment of the Requirements for the

Degree of Master of Science

(in Electrical Engineering)

August, 2001

The current versus voltage (I/V) characteristics of undoped and gold doped WO_3 thin film sensors were studied both experimentally and theoretically. A simplified equivalent circuit was formulated for the WO_3 sensor. It includes forward and reverse biased Schottky diodes which represent the contact region between the electrodes and the film and a resistor which represent the sum of crystallite resistance and the intercrystallite resistance between the individual crystallites. According to the electron transport mechanisms through the Metal Semiconductor (M/S) boundaries and intercrystallite boundaries, two kinds of I/V and corresponding Resistance/Voltage(R/V)characteristics are possible, one based on thermionic emission theory and the other based on tunneling theory.

A one channel gas delivery system was built to experimentally determine the I/V characteristics. The experimental results were obtained for both gold-doped WO_3 and undoped WO_3 sensors. The WO_3 films were R-F sputtered onto a sapphire substrate and annealed in compressed air at 400°**C** for 24 hours. The voltage range for the tests was from –20V to 20V and the temperature range was from room temperature to 400°C. The experimental results for the I/V characteristics were taken in compressed air , 30 PPM H_2S and in ethylene. The I/V experimental results are approximately linear except in the lower voltage region where they are nonlinear. The R/V results are more sensitive and nonlinear. Besides, the sensor performance was also examined in the AC case. The preliminary results on real and imaginary components of the impedance were also presented as a function of frequency and voltage.

Comparing the experimental results of the I/V characteristics and the corresponding R/V characteristics taken in compressed air or target gases such as H_2S with the theoretical curve predicted by thermionic emission and tunneling theories, it is obvious that the tunneling effect is the dominant electron transport mechanism in the WO_3 thin film sensor. The depletion width is the key parameter which determines the appropriate electron transport mechanism associated with M/S and intercrystallite boundaries. Since the depletion width is related to the argon oxygen ratio in the R-F magnetron sputtering system one can apriori design a sensor which will exhibit either themionic emission or tunneling at the M/S and intercrystallite boundaries.

ACKNOWLEDGEMENTS

I am grateful to my advisor, Dr. John F.Vetelino, for providing me with the precious opportunity to continue my education at UMaine, and also for all of the time and energy he has spent with me during my two-year graduate study. I wish to thank for Dr. David Frankel who really gave me valuable guidance. I also would like to Thank Dr. Brian G. Frederick and Dr. Rich Morrow for their help in understanding the theory. At the same time, I also wish to thank my thesis committee member, Dr. David E. Kotecki for all of his time and assistance with this thesis. Thanks also go to Dr. George Bernhardt, Dr. Scott Moulzolf and Dr. Jay Legore from the Laboratory of Surface Science and Technology at UMaine for their continuous support. I also want to thank all the other faculty members in Electrical and Computer Engineering Department and members in the Laboratory of Surface Science and Technology who have given me help during my graduate study at UMaine. Finally I would like to thank my family, especially my husband, Jack, for his constant support and care, without which this thesis couldn't have been done. I also extend my thanks to all my friends for their encouragement and assistance.

TABLE OF CONTENTS

ACKNOWLEDGEMENTS ii

LIST OF TABLES vi

LIST OF FIGURES vii

1. INTRODUCTION 1

1.1 BACKGROUND 1

1.2 METAL OXIDE SEMICONDUCTOR SENSOR 3

1.3 OBJECTIVE 10

1.4 ORGANIZATION 11

2. THEORY OF THE I/V CHARACTERISTICS OF SEMICONDUCTING METAL OXIDE SENSORS 13

2.1 STRUCTURAL MODEL FOR THE THIN FILM SENSOR 13

2.2 ELECTRON TRANSPORT IN SEMICONDUCTING METAL OXIDE FILMS 16

2.3 METAL ELECTRODE SEMICONDUCTOR JUNCTION 29

2.3.1 Origins of the Schottky Barrier 29

2.3.2 Electric Field and Potential Distribution in the Depletion Region 36

2.3.3 Current Voltage Characteristics 42

2.4 EQUIVALENT CIRCUIT MODEL 55

3. EXPERIMENTAL PROCEDURE FOR THE MEASUREMENT OF THE I/V CHARACTERISTICS OF WO_3 THIN FILM SENSORS 57

3.1 CURRENT VERSUS VOLTAGE MEASUREMENT TECHNIQUES 57

3.2 GAS DELIVERY SYSTEM 61

3.3 DATA ACQUISITION SYSTEM 63

4. EXPERIMENTAL RESULTS AND DISCUSSION 66

4.1 WO_3 THIN FILM SENSOR STRUCTURE AND PREPARATION 66

4.2 TEMPERATURE EFFECT ON CURRENT VERSUS VOLTAGE CHARACTERISTICS IN COMPRESSED AIR 68

4.2.1 I/V characteristics of gold-doped WO_3 sensor as a function of temperature 68

4.2.2 I/V characteristics of an undoped WO_3 sensor as a function of temperature 70

4.3 ELECTRICAL RESISTANCE OF WO_3 THIN FILM SENSOR 71

4.3.1 Resistance of a gold-doped WO_3 sensor as a function of temperature 72

4.3.2 Resistance of an undoped WO_3 sensor as a function of temperature 76

4.4 H_2S GAS EFFECT 78

4.4.1 The resistance of gold-doped WO_3 sensor as a function of voltage under H_2S gas exposure 78

4.4.2 WO_3 sensor's resistance as a function of voltage under H_2S gas exposure for the undoped WO_3 sensor 84

4.5 SENSITIVITY VS. VOLTAGE 90

4.6 ETHYLENE EFFECT 97

4.7 AC MEASUREMENT 99

4.8 EXPERIMENTAL RESULTS DISCUSSION AND THE COMPARISON WITH THEORY FOR THE I/V CHARACTERISTICS OF WO_3 FILMS 102

4.8.1 Discussion 102

4.8.2 Comparison of Experimental Results with Theory 111

5. SUMMARY, CONCLUSIONS AND FUTURE WORK 119

5.1 SUMMARY 119

5.2 CONCLUSIONS 122

5.3 FUTURE WORK 124

REFERENCES 128

APPENDIX A: DEVIATION OF DIFFUSION THEORY (EQUATION 38) 130

APPENDIX B: DEVIATION OF EQUATION (39) 134

BIOGRAPHY OF THE AUTHOR 138

LIST OF TABLES

Table 1: History of the development of some important chemical sensors 2

Table 2: Fitting parameters for Figures 65 to 69 117

LIST OF FIGURES

Figure 1: (a) Taguchi Sensor (b) Sensor structure made in LASST 5

Figure 2 : The electrical conductivity as a function of inverse temperature for WO_3 film. Arrow indicates the direction of increasing and decreasing temperature[7] 6

Figure 3 : Equivalent circuit for the SMO sensor in the DC case................................ 8

Figure 4 : (a) ideal I/V curve (b) real I/V curve of SnO_2 sensors[10] 8

Figure 5 : Equivalent circuit for an SMO sensor in the AC case. R_{ei}, C_{ei}, R_{eo} and C_{eo}-circuit elements of the input and output electrodes; C_s and R_s-circuit elments for the sensing element; C_i and R_i-circuit elements for the sensing element/substrate interface; C_b and R_b-circuit elements for the substrate 9

Figure 6: Structural model for a polycrystalline sensor... 14

Figure 7: The physical structure of SMO sensing element which consists of Metal contact (grey) connected by grains of polycrystalline SMO film (clear) with surface catalyst loading(small black dots). An idealized conduction band diagram indicates the potential barriers between the microcrystals with partial filling of the conduction band in the grains. The one dimensional equivalent circuit of the film and contacts is represented as a RC ladder network.. 15

Figure 8: Band structure for an n-type metal oxide 17

Figure 9: The double layer near a metal oxide surfaces. 18

Figure 10: An accumulation layer in an n-type metal oxide whose surface donor

states are in the conduction band 18

Figure 11: An inversion layer in an n-type metal oxide which has ionized acceptors, ionized donors and holes near the surface region 19

Figure 12: Charge distribution density in the depletion region. x_0 is the depletion region width 20

Figure 13 : Variation of the potential, V(x), across the depletion region 22

Figure 14: Model of the semiconducting metal oxide with surface and bulk film conductivities. The cross-hatched regions are electrodes, the dotted region is the film and the remaining area is the substrate 24

Figure 15: The energy band representation of an n-type polycrystalline semiconductor thin film with a grain size, L_1, and a grain boundary width, L_2. The grain boundary barrier potential is q_b.............................. 25

Figure 16: Resistance-temperature characteristics of single grains and single grain boundaries on a large grained ceramic [12].................................... 26

Figure 17: Band diagram illustrating band bending at grain boundary (a) two crystals have the same orientation in equilibrium (b) two crystals have different orientation in equilibrium (c) under applied voltage (the case of same orientation)(from Cohen et al.[14]).............................. 27

Figure 18: Electron energy band diagrams of metal contact to n-type semiconductor with $_m>_s$, and the materials separated from each other 30

Figure 19: Electron energy band diagrams of metal contact to n-type semiconductor with $_m>_s$ in thermal equilibrium after the contact

has been made 32

Figure 20: Electron energy band diagrams of a metal contact on an n-type semiconductor (a) thermal equilibrium (b) forward bias (c) reverse bias. 35

Figure 21: Electric field and potential distributions in the depletion region of a Schottky barrier. (a) Energy band diagram; (b) electric field distribution; and (c) potential distribution. V is the applied voltage. [20] 36

Figure 22: Normalized current voltage characteristics for thermionic emission which is predicted by equation 42. I/I_0 is the normalized current 51

Figure 23: Normalized current voltage characteristics predicted by equation 46. I/I_0 is the normalized current.. 53

Figure 24:The comparison of I/V characteristics of thermionic emission and tunneling effect with different n values. (a) n=2, (b) n=3 and (c) n=∞ 54

Figure 25: Equivalent circuit model for the SMO sensor in the DC case.................. 56

Figure 26: Two probe measurement of the WO_3 sensor.. 58

Figure 27: (a) Four-probe measurement of an undoped SnO_2 sensor. (b) Equivalent circuit for Four-probe measurement.[27].......................... 58

Figure 28: Three-probe arrangement to measure the contact contribution.[27] 59

Figure 29: Different configurations used to model the conductimetric sensor. Cross-hatch region - electrodes; shaded region - sensing film; White region – substrate 59

Figure 30 : Two possible circuit configurations for conductivity measurement 60

Figure 31: Block diagram of the set-up used for measurement of AC impedance..... 61

Figure 32: Gas delivery system.. 62

Figure 33: Schematic diagram of the sensor gas chamber.. 63

Figure 34: Diagram of data acquisition system 64

Figure 35: Top view of the WO_3 thin film sensor. TOP -MOS sensing element with IDT and sensing film. BOTTOM-MOS sensing element with heater and RTD. The dimensions are given in inches 67

Figure 36: I/V characteristics of gold-doped WO_3 sensor as a function of temperature 69

Figure 37: R/V characteristics of gold-doped WO_3 sensor as a function of temperature 69

Figure 38 : I/V characteristics of an undoped WO_3 sensor as a function of temperature 70

Figure 39: R/V characteristics of an undoped WO_3 sensor as a function of temperature 71

Figure 40: The resistance and temperature relationship of a gold-doped WO_3 sensor. X-axis is time, the temperature is changed in every two hours. The temperature is increased from room temperature to 400°C in steps of 100°C and then decreased form 400°C to room temperature in steps of 100°C. The voltage is 2.5Volts.. 73

Figure 41: The variation of a gold-doped WO_3 sensor's resistance as a function of temperature. The range of temperature was from 200°C to 400°C. The temperature was increased from room temperature to 200°C, and

then from 200°C increased to 400°C in steps of 50°C. After the increasing process the temperature was decreased from 400°C to 200°C in steps of 50°C. The temperature is changed every two hours. The voltage is 2.5Volts 74

Figure 42 : The hysteresis of the variation of a gold-doped WO_3 sensor's resistance asa function of temperature.(a)temperatures from 200°C to 400°C.(b) temperatures from 23°C to 400 °C. The direction of the arrow is the trace of temperature. '+' means the temperature increases,' - 'means the temperature decreases 75

Figure 43: The variation of an undoped WO_3 sensor's resistance with temperature. X-axis is time and the temperature is changed every two hours. The temperature is decreased from 400°C to room temperature in steps of 100°C and then increased room temperature to 400°C in steps of 100°C.The voltage is 2.5Volts 77

Figure 44: The variation of an undoped WO_3 sensor's resistance with temperature. The range of temperatures used is from 23°C to 400°C in steps of 50°C 77

Figure 45: I/V characteristics of a gold-doped WO_3 sensor under compressed air and H_2S gas exposure. The H_2S gas concentration is 30 PPM. The heater temperature is (a) 23°C, (b)100°C, (c) 200°C and (d) 300°C 79

Figure 46 : R/V characteristics of a gold-doped WO_3 sensor under compressed air and H_2S gas exposure. The H_2S gas concentration is 30 PPM. The heater temperature is (a) 23°C, (b) 100°C, (c) 200°C and (d) 300°C 81

Figure 47: The hysteresis behavior of I/V characteristics and the variation of resistance as a function of voltage under H_2S and compressed air. The sensor is a gold doped WO_3 sensor. The environment Temperature is 250°C. The curve (1) and (3) were taken in compressed air and curve (2) and(4) were taken in H_2S gas exposure..... 83

Figure 48: I/V characteristics of an undoped WO_3 sensor under compressed air and H_2S gas exposure. The H_2S gas concentration is 30 PPM. The heater temperature is (a) 23°C, (b)100°C, (c) 200°C and (d) 300°C 85

Figure 49 : The variation of an undoped WO_3 sensor's resistance with voltage under compressed air and H_2S exposure. The gas concentration is 30ppm. The heater temperature is (a) 23°C, (b) 100°C, (c) 200°C and (d) 300°C. 87

Figure 50: The hysterisis behavior of I/V characteristics and the variation of resistance as a function of voltage under H_2S and compressed air. The sensor is an undoped WO_3 sensor. The environment temperature is 250 °C. The curve (1) and (3) were taken in compressed air and curve(2) and(4) were taken in H_2S gas exposure.................................... 89

Figure 51: (a) The variation of sensitivity as a function a voltage, the sensor is gold-doped WO_3. (1) positive means the voltage starts from -20V and increases to 20V. (2) negative means the voltage starts from 20V and goes the other way to -20V. (a), (b), (c) and (d) curve represents the sensitivity at room 23°C, 100°C, 200°C and 300°C respectively....... 92

Figure 52: The variation of sensitivity as a function of voltage, the sensor is

undoped WO_3. (1) positive means the voltage starts from -20V and increases to 20V. (2) negative means the voltage starts from 20V and goes the other way to -20V. (a), (b), (c) and (d) curve represents the sensitivity at room 23°C, 100°C, 200°C and 300°C respectively 94

Figure 53: The hysterisis behavior of sensitivity as a function of voltage. The film is undoped WO_3 film. The environment temperature is 250 °C. The arrow direction is the trace of the voltage. (1),(2),(3) and (4) are the order of the measurement 96

Figure 54: I/V characteristics of gold -doped WO_3 sensor, (1) taken under the synthetic air, (2) taken under the ethylene exposure and the concentration is 5 parts per million. The examining temperature is 400 °C 98

Figure 55: R/V characteristics of gold-doped WO_3 sensor, (1) taken under the compressed air, (2) taken under the ethylene exposure and the concentration is 5 parts per million. The temperature is 400 °C 98

Figure 56: Variation of the sensitivity of gold-doped WO_3 as a function of temperature, voltage and ethylene concentration 99

Figure 57: The real part of the impedance of undoped WO_3 sensor as a function of frequency at different voltages. The temperature is 350°C.(a) full scale (b) zoomed part 100

Figure 58: The imaginary part of the impedance of undoped WO_3 sensor as a function of frequency at different voltages. The temperature is 350°C. (a) full scale (b) zoomed part. 101

Figure 59: The equivalent circuit model for the sensor structure shown in Figure 35. 103

Figure 60: I/V characteristics based on thermionic emission theory. n is the ideality factor 106

Figure 61: I/V characteristics based on the thermionic field emission (tunneling) theory. 108

Figure 62: I/V characteristics of both models, solid line based on tunneling, dotted line based on thermionic emission. The ideality factor for both models is *n*=2. 109

Figure 63: R/V characteristics based on the thermionic emission model.(n=2) 110

Figure 64: R/V characteristics based on the tunneling model.(n=2) 110

Figure 65: Comparison of the experimental and theoretical I/V curves for the undoped WO_3 sensor at 200°C. 112

Figure 66: Comparison of the experimental and theoretical R/V curves for the undoped WO_3 sensor at 200°C. 113

Figure 67: (a) Comparison of the experimental and theoretical I/V curves for the gold-doped sensor at 200°C. (b) the corresponding R/V comparison for the gold-doped sensor at 200°C. 114

Figure 68: (a) Comparison of the experimental and theoretical I/V curves for the undoped sensor exposed to H_2S gas at 200°C. (b) the corresponding R/V comparison for the undoped sensor exposed to H_2S at 200°C 115

Figure 69: (a) Comparison of the experimental and theoretical I/V curves for

the gold-doped sensor exposed to H_2S gas at 200°C. (b) the corresponding R/V comparison for the gold-doped sensor exposed to H_2S at 200°C. 116

1. INTRODUCTION

1.1 Background

The need for sensors for a wide range of applications has been recognized for many centuries. People in the early times used animals and birds as sensors to detect dangerous gases such as methane (CH_4) and hydrogen sulfide (H_2S). In recent years the detection of toxic gases has become more important since environmentally harmful gases such as nitrogen oxide (NO_x), sulfur oxide (SO_x) and warfare agents pose a serious problem to the military, general public and the environment. Toxic gases such as NO_x and SO_x are produced as by products of the mining and refining of fossil fuels, the burning of these fuels for energy and the manufacturing process itself. In large quantities, these gases have a devastating effect on the nation's environment and the health of its population in the form of ozone, acid rain, ground water contamination and smog. More recently, chemical and biological warfare agents have become potential threats not only to soldiers in the battlefield but also to people in congested areas such as airports or sports arena which maybe the target of terrorists.

The need for *in situ* gas sensors which can respond sensitively, selectively and quickly to a target gas has accelerated research on a variety of gas sensors. In the early 20th century rapid advances in technology prompted the development of various types of sensors. Table 1 shows the history of the development of some important chemical sensors.

1923	Catalytic combustion-type sensor
1930	Glass electrode for pH measurement
1938	Humidity sensor using LiCl Film
1952	Galvanic cell-type gas sensor
1961	Ion electrode sensor
1961	Solid electrolyte-type sensor
1962	Metal-Oxide semiconductor gas sensor(Taguchi sensor)
1964	Piezoelectric quartz crystal sensor
1966	Glucose sensor
1970	ISFET
1970	Optical fiber gas sensor
1975	Pd gate FET hydrogen sensor
1976	A/F sensor for the automobile
1977	Enzyme FET
1981	Surface Acoustic wave gas sensor
1989	Acoustic Plate mode sensor
1991	Love mode Sensor

Table 1: History of the development of some important chemical sensors

One of the most interesting and sensitive gas sensors studied is the semiconducting metal oxide semiconductor (SMO) gas sensor. The initial work on this type of sensor may be traced to the work of Bardeen et al. [1] in 1950. Bardeen et al. were working on the development of a novel semiconductor device when they discovered that gas sorption onto the semiconductor surface caused significant changes in the electrical conductivity. They needed to passify the semiconductor surface so as to eliminate the conductivity change due to the sorption of gas. In the early 1960's Seiyama [2,3] made the first deliberate effort to use the active surface on the semiconductor as a gas sensor. Seiyama monitored the change in the conductivity of a host of semiconducting films when they were exposed to gases such as CO,

alcohol and oxygen. Since that time, a large amount of research was performed [4] in order to realize commercial semiconductor devices for gas detection. The first gas sensor and perhaps the most famous did not appear until 1968 and was the result of a tremendous amount of work by Naoyoshi Taguchi[5]. When Taguchi started his work he had no knowledge of gas absorption or even metal oxide semiconductors. His motivation for the development of the gas sensor was triggered by a liquefied petroleum gas explosion in Japan which killed ten people. He went from the beginning to the end of the periodic table before he finally settled on SnO_2 as the sensing element. After an almost superhuman effort he developed a commercial product [5] called the Taguchi sensor resulting in the most widely available commercial SMO sensor to date. These sensors operate on the principle that a chemical reaction between the gas species to be detected and a semiconductor sensing film produces a change in the film resistance. Therefore upon application of a voltage or current to the sensing film, the film resistance becomes a direct measurement of the gas concentration. These sensors have now grown to be very important devices for detecting a wide range of gases.

1.2 Metal Oxide Semiconductor Sensor

Metal oxide semiconductors have been used as gas sensing materials because of their high sensitivity to the presence of various gases in the ambient atmosphere. In order to explain their high sensitivity it is necessary to examine the semiconducting properties of the metal oxides. Metal oxides can be classified as being poor

semiconductors. The electron concentration in these oxides however can change dramatically with the introduction of impurities into the metal oxides. In order to illustrate the dramatic changes in electrical conductivity that trace impurities can cause, consider as an example, silicon. If a silicon wafer is doped with a small amount of phosphorus (less than 1 phosphorus atom in 10^6 silicon atoms), the conductivity will be increase by a factor of 10^9 which illustrates the fact that only a very small concentration of a dopant can change electron concentration significantly.

The SMO sensor can be configured in a variety of different ways. Figure 1 shows two possible structures for the SMO sensor. The early one (Figure 1a) is the Taguchi sensor and the more recent one was made by researchers in the Laboratory of Surface Science and Technology (LASST) at the University of Maine. Typically, the metal oxide semiconducting films, of which tin oxide (SnO_2), tungsten trioxide (WO_3), titanium oxide (TiO_2) and zinc oxide (ZnO) are the most popular, are deposited onto an insulating substrate using vacuum evaporation or sputtering techniques. Metal electrodes are deposited as electrical contacts to the sensing layer. Since a significant interaction of a target gas with the metal oxide film occurs over a narrow temperature range, it is also necessary to have a heating element capable of accurately achieving a desired temperature. The heating element in the Taguchi sensor is a coil of wire shown in Figure 1a while in Figure 1b the desired temperature is achieved with an electrode configuration representing a heater and resistance temperature device (RTD).

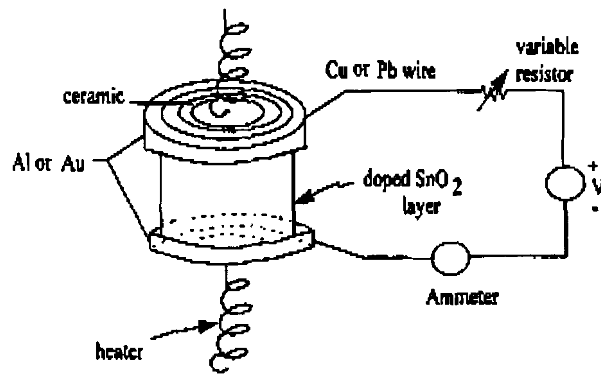

(a)

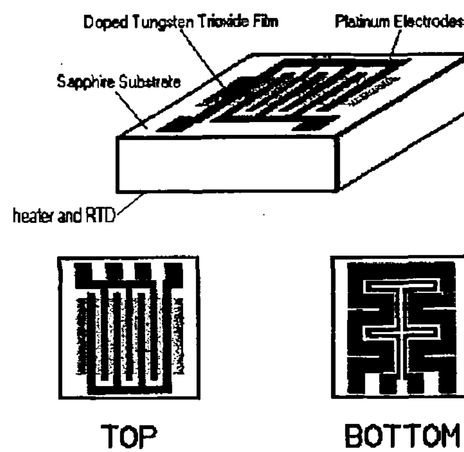

TOP - MOS sensing element with IDT and sensing film.
BOTTOM - MOS sensing element with heater and RTD.

Figure 1: (a) Taguchi Sensor (b) Sensor structure made in LASST

Once the metal oxide film has been deposited the film is heated to a certain temperature for a set period of time. This process is called annealing. Basically the annealing process stabilizes the film in terms of the structure and electrical properties. In the case when the film was deposited at or near room temperature the film is amorphous in structure. The annealing process causes the film to transition from an amorphous structure to a polycrystalline structure. In this process water is irreversibly driven from the film. The annealing process also rids the film of surface impurities or

contaminants which may lead to changes in the film's electrical properties over time. Typically the annealing process is performed in dry air at elevated temperatures for a set period of time. As an example of the stablization of the electrical properties of the film, Figure 2 shows the variation of the conductivity of WO_3 as a function of inverse temperature [6]. At about 315°C a discontinuity in the conductivity is observed indicating the amorphous to polycrystalline phase transition. Repeated heating and cooling will follow the trace from E to D reversibly. This process has been shown to not only stabilize the film structure but hasten the chemical kinetics resulting in a faster and more sensitive response to a target gas.

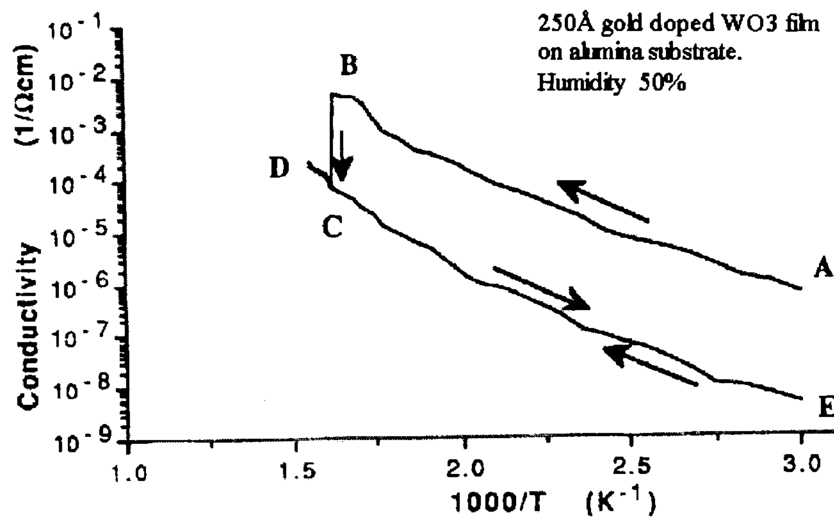

Figure 2 : The electrical conductivity as a function of inverse temperature for WO_3 film. Arrow indicates the direction of increasing and decreasing temperature[7].

It is also possible to improve critical sensor properties such as selectivity, response time and response magnitude by dispersing small metallic particles such as gold or platinum on the metal oxide semiconductor surface. The catalysts can not

only concentrate the reactants by adsorbing the appropriate gas molecules, but also provide a reaction path which requires a small amount of activation energy. As a consequence the response and recovery times are shortened and the sensitivity is increased [8].

In conventional chemiresistive sensors, the resistance is monitored while the sensor is in the test environment. The target gas interacts chemically with the sensing film causing a change in the number of mobile electrical charge carriers. If the absorbing gas is a reducing agent, it injects electrons into the semiconductor and causes the conductivity to increase and if it is oxidizing agent, it extracts electrons from the semiconductor and the corresponding conductivity decreases. The film resistance is typically monitored by an electrometer, which supplies a DC voltage to the test device, measures the resulting current, and uses Ohm's law to calculate the resistance. One could also supply current through a test device and measure the voltage drop between the electrodes. An equivalent circuit for the DC case is shown in Figure 3, where the film resistance, Rs, is an indicator of the gas concentration and R represents the contact resistance. If the sensing element is just a resistor, one should get a linear current voltage characteristic as shown in Figure 4(a). In reality, however, one often obtains a nonlinear behavior as shown in Figure 4(b). This may be due to the effect of grain boundaries in the film and the metal semiconductor junction formed between the metal contacts and the film [9].

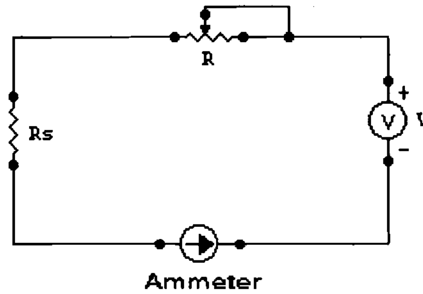

Figure 3 : Equivalent circuit for the SMO sensor in the DC case

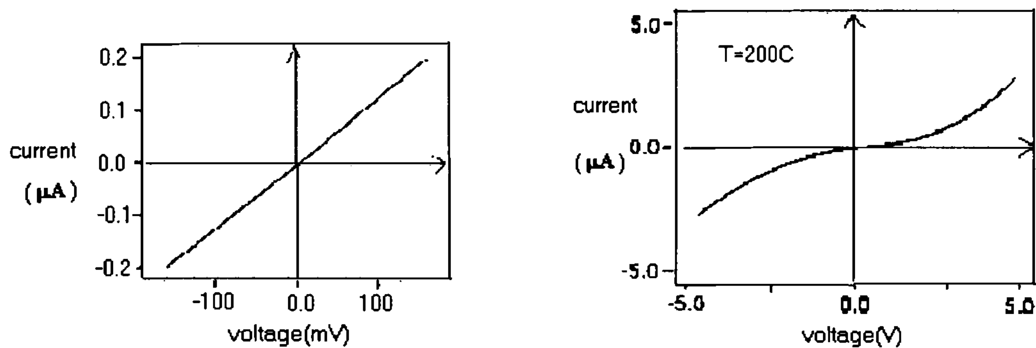

Figure 4 : (a) ideal I/V curve (b) real I/V curve of SnO_2 sensors[10]

The SMO sensor may also be operated in an AC mode. In this case an AC voltage is applied and the impedance of the film is measured. This type of sensor has the advantage that one can choose the frequency of operation and measure the real and imaginary components of the impedance. Therefore when compared to the chemiresistive sensor which has only the film resistance as a measure of gas-film interaction, the impedance based sensor has four parameters, namely the real , imaginary , magnitude and phase components of impedance . This enables one to monitor not only the change in electron concentration but also the accumulation or depletion of charge at the metal oxide interface region and at the intercrystalite boundaries. The resulting current versus voltage characteristic is more complex.

Figure 5 shows a possible equivalent circuit in the AC case. One can clearly see that the equivalent circuit is a complex arrangement of capacitors and resistors, with C_{ei}, R_{ei}, C_{eo}, R_{eo} being the circuit elements associated with the input and output electrodes, C_s and R_s being the circuit elements for the sensing element, C_i and R_i being the circuit elements for the interface between sensing element and substrate and C_b and R_b being the circuit elements for the substrate. Based on preliminary investigations of the impedance of metal oxide films [11], a significant variation in the real and imaginary parts of the impedance as a function of frequency occurs. The Schottky barrier and capacitive effects at the electrodes and intercrystalite boundaries may be responsible in part for these variations.

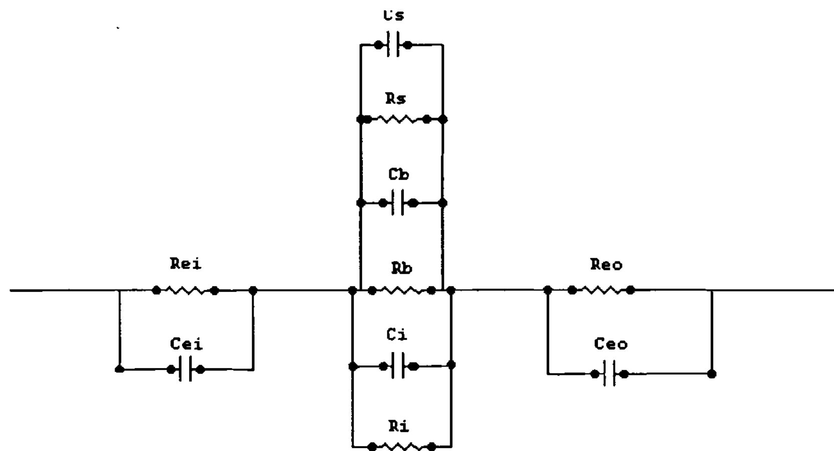

Figure 5 : Equivalent circuit for an SMO sensor in the AC case. R_{ei}, C_{ei}, R_{eo} and C_{eo}-circuit elements of the input and output electrodes; C_s and R_s-circuit elements for the sensing element; C_i and R_i-circuit elements for the sensing element/substrate interface; C_b and R_b-circuit elements for the substrate.

Little or no work has been done on the current voltage characteristics in the DC or AC case. In the DC case, one should expect a linear behavior if the sensing element is a pure resistor, however preliminary measurements [10] indicate a nonlinear behavior. In the AC case, the behavior is more complex because one must take into account the behavior of the capacitor's charging and discharging.

1.3 Objective

The transport properties of the mobile carriers in polycrystalline semiconductor compounds constitute the basis for understanding the sensing function of semiconductor gas sensors. If there is no bias voltage across the film, the carriers are in an equilibrium state, however, if one applies a voltage, the applied voltage would cause the electrons to move and overcome the potential barriers at the metal electrode semiconductor junction and intercrystallite grain boundaries and become free. Because the conductivity is directly proportional to the free charge concentration and the resistance is proportional to the inverse of the conductivity, a change in voltage may change the resistance. There is charge on the depletion region boundaries giving rise to capacitive effects. In the DC case, since the frequency is 0Hz the impedance due to the capacitor is infinity which corresponding to an open circuit. When frequency is increased the corresponding impedance is not infinity and one must taken into account the capacitive effects in the AC case.

The major objective of this thesis is to perform an experimental and theoretical

study of the voltage versus current characteristics of an undoped and gold doped WO_3 thin film sensor exposed to air and air plus a target gas. In order to determine the current voltage characteristics of a WO_3 film, a one-channel gas delivery system was built. In order to examine the effect of temperature, the current versus voltage characteristics were taken in synthetic air from room temperature (23°C) to 400°C. For the gas effect, two candidate gases were chosen, hydrogen sulfide (H_2S) and ethylene (CH_2), both of which are reducing agents. The voltage current characteristic is examined under different gas concentrations. The sensitivity versus voltage and gas concentration at different temperatures is discussed in detail. Band structure theory is used to explain the metal and n-type semiconductor interface and the interface at the crystallite boundaries in the semiconductor. In addition, the sensor performance is also examined in the AC case. The preliminary results on real and imaginary components of the impedance are also presented as a function of frequency and voltage.

1.4 Organization

The thesis consists of four major segments, which include the theory of a metal semiconductor interface and intercrystallite boundaries, the experimental setup for measuring the current versus voltage characteristic, the experiment results and comparison with theory, conclusions and future work.

The thesis is divided into 5 chapters. Chapter one presents the introduction, background, objective and organization. The second chapter presents the equivalent circuit model for the WO_3 thin film sensor. A real circuit was built and the current versus voltage characteristics were measured. The electron transfer behavior was explained using band theory. The third chapter presents a general description of the experimental gas delivery system for controlling the temperature and the ambient and target gas concentrations. The testing system for measuring the current versus voltage relationship and resistance versus time is also presented. The fourth chapter presents the experimental results of the I/V characteristics under ambient and different gas exposures. For the ethylene gas, the detailed I/V relationship under different ethylene concentration is presented. The sensitivity versus temperature, voltage and gas concentration is discussed in detail. In addition, the real and imaginary components of impedance in the AC case are presented as a function of frequency and voltage. In the DC case a comparison of the behavior of an equivalent circuit model and the real SMO thin film sensor is presented and conclusions are drawn. The fifth chapter presents a summary of the present work and discusses future work.

2. THEORY OF THE I/V CHARACTERISTICS OF SEMICONDUCTING METAL OXIDE SENSORS

This chapter presents the structural and equivalent circuit models and the theory of electron transport for the WO_3 thin film sensor. The electron transport behavior is explained using band theory. Four different electron transport mechanisms are discussed in this chapter. These transport mechanisms are drift and diffusion, thermionic emission and thermionic field emission which is the tunneling effect.

2.1 Structural Model for the Thin Film Sensor

The WO_3 films may exist in either an amorphous or polycrystalline state or a combination of both. An amorphous film is highly disordered and exhibits no periodicity while a polycrystalline film consists of many randomly oriented microcrystalline regions, each of which exhibits periodicity. Since the films are deposited at elevated temperatures or annealed after deposition, they typically exhibit a polycrystalline microstructure.

The structure of the metal oxide thin film sensor can roughly be modeled physically as shown in Figure 6. In this figure, the basic sensor structure consists of a polycrystalline film and the contact electrodes. Microscopically each semiconductor crystallite is connected with its neighbors by a grain-boundary. Electrons can move

across the potential barrier at each boundary. The gas film interaction can change the barrier height and the number of free carriers which results in a change of the electrical resistance of the film. The non-ohmic contact of the metal-semiconductor junctions may also lead to potential barriers, the effects of which can be compared to, and compete with, those already mentioned for grain boundaries.

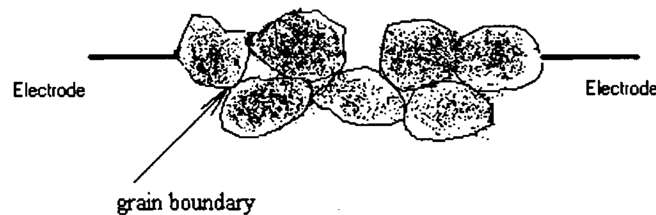

Figure 6: Structural model for a polycrystalline sensor

The chemistry and physics associated with the semiconductor gas sensor is complex in regard to both the sensor's reactivity towards gases and structure. In order to simplify the problem, it is assumed that the film consists of only a single layer of crystallites as shown in Figure 7. The energy band diagram along with a possible equivalent circuit representation is also presented in Figure 7.

An examination of the band structure reveals the existence of various potential barriers introduced by metal semiconductor junctions and crystallite or grain boundaries. The height of the potential barrier is dependent on a variety of parameters, which include specific film deposition parameters, temperature, gas environment, SMO film type and metal electrodes. These barriers and the bulk crystallites can be represented in terms of an equivalent ladder network consisting of combinations of resistors and capacitors.

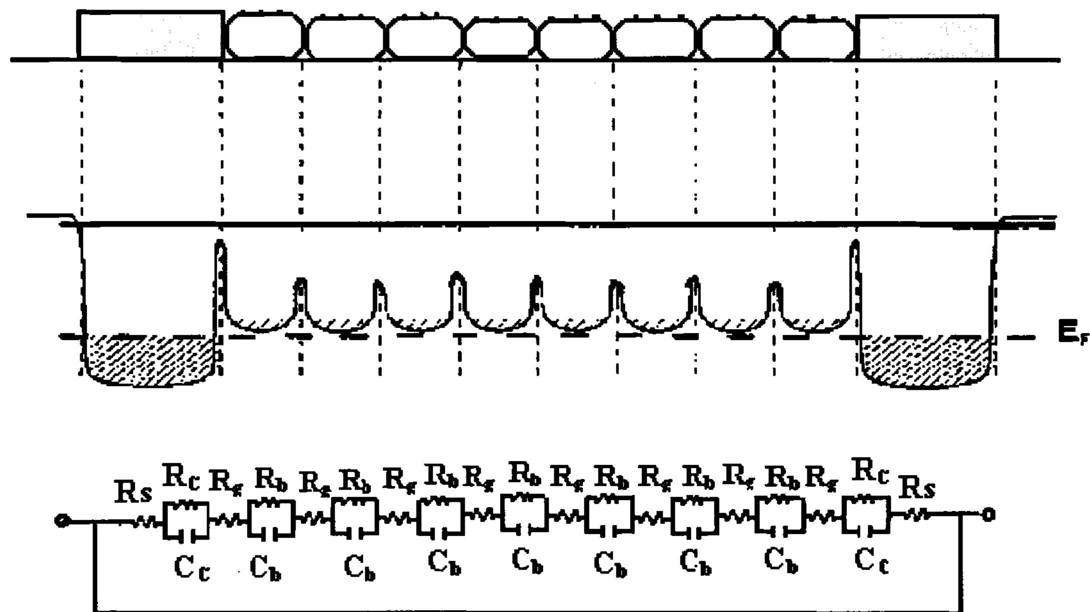

Figure 7: The physical structure of SMO sensing element which consists of metal contact (grey) connected by grains of polycrystalline SMO film (clear) with surface catalyst loading(small black dots). An idealized conduction band diagram indicates the potential barriers between the microcrystals with partial filling of the conduction band in the grains. The one dimensional equivalent circuit of the film and contacts is represented as a RC ladder network.

The equivalent circuit for the sensor includes the crystallite resistance, R_g, the grain boundary resistance, R_b, grain boundary capacitance C_b, the metal-semiconductor junction resistance and capacitance, R_c and C_c and the electrode finger resistance R_s. One can combine each of the circuit elements to an equivalent impedance for the sensing element. When significant interactions occur between the

sensing element and the measurand, the values of the circuit elements, R_c, C_c, R_g, R_b and C_b, may change.

The electrodes used in conductimetric sensors are noble metals such as platinum. If one used oxidizing metal such as aluminum as electrodes one must consider the contact with the semiconductor as a metal-insulating oxide semiconductor contact. This is due to that fact that oxidizing metals are prone to oxidize. However if a noble metal such as platinum is used for the electrodes the contact is a metal semiconductor contact.

2.2 Electron Transport in Semiconducting Metal Oxide Films

Most semiconducting metal oxide films such as WO_3 are n-type semiconductors. The n-type behavior is due to the fact that oxygen vacancies exist in the film. Therefore the ratio of oxygen ions to tungsten ions is not exactly three to one but slightly less. This gives rise to weakly bound electrons around some of the tungsten ions. These weakly bound electrons readily enter the conduction band causing the metal oxide to be n-type. The oxygen vacancies are then said to act as donors in the film. The geometry of the film is severely interrupted at the surface. This can lead to localized allowed energy levels which may occur in the energy gap. Since metal oxides are more ionic than covalent in nature, the metal ion is referred to as the cation and oxygen is the anion. The surface metal ions have a complete outer shell of electrons but capture extra electrons due to their net charge and therefore act as acceptors. For a single crystal, Figure 8 shows the band structure of the metal

oxide semiconductor surface. In this case, there is no net surface charge and it is called the flat-band case. The surface states are shown as narrow bands with the donor state occupied and the acceptor states unoccupied.

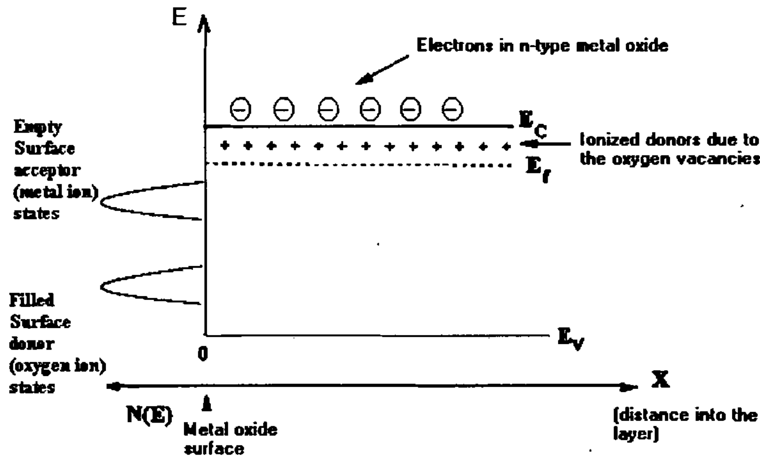

Figure 8: Band structure for an n-type metal oxide.

Since the allowed energy levels for the acceptor state is less than the conduction band electron energy, the electrons from the donor sites in the n-type metal oxide move into the acceptor states creating partially occupied acceptor states. A so-called double layer is then formed which has positively charged donor ions in the semiconductor and negatively charged surface acceptor states as a sheet of charges on the surface. The double layer is shown in Figure 9. The region $0 < x < x_0$ is called the space charge layer or depletion layer and is depleted of any mobile charges.

In the previous discussion the majority of the carriers in the metal oxide semiconductor were electrons and they migrated to the surface giving rise to a so-called double layer. This is a normal case for semiconductor metal oxide gas sensors.

There are, however, two other cases. One related to the situation when there is an excess of majority carriers on the surface or an accumulation layer. The other case has an excess of minority carriers on the surface which is called an inversion layer.

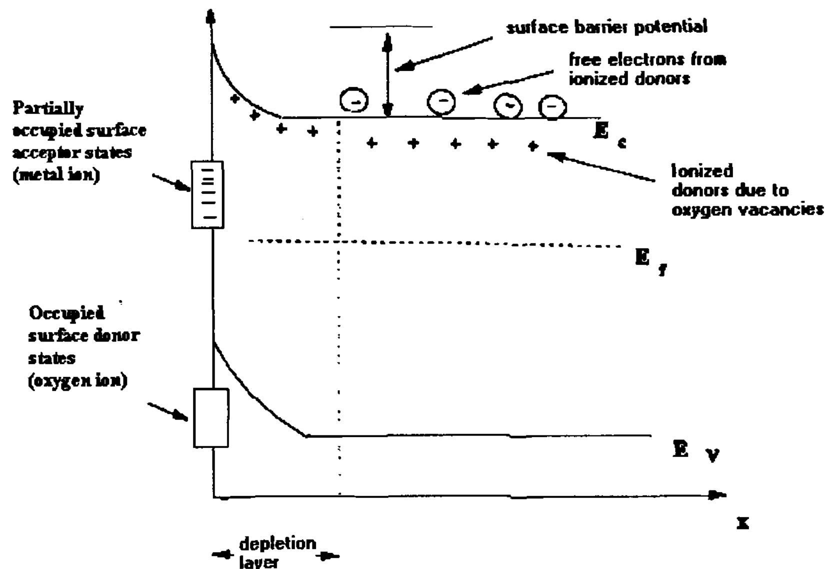

Figure 9: The double layer near a metal oxide surfaces.

The accumulation layer is caused by surface donor states that are located near the conduction band of the semiconductor as shown in Figure10. The donor electrons are injected into the conduction band and positively ionized donor states appear on the surface along with an excess of electrons.

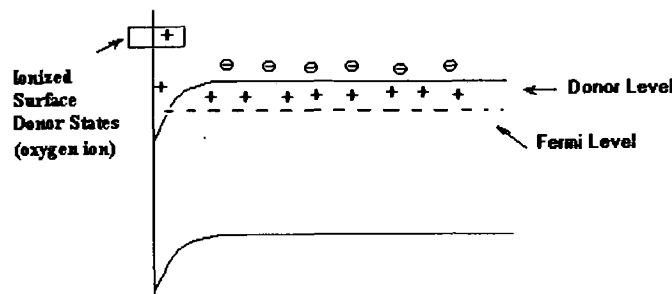

Figure 10: An accumulation layer in an n-type metal oxide whose surface donor states are in the conduction band.

A surface inversion layer is formed if the surface acceptor states can obtain electrons from the valence band as shown in Figure 11. The surface has negatively charged ionized acceptors, positively charged donors and holes. This is called an inversion layer since it has excess holes on the surface while the metal oxide is n-type. Although the majority of carriers in the metal oxide semiconductor bulk are electrons, the positively charged holes near the surface form a p-type channel. Holes then move through this channel and increase the conductivity. This type of channel is the dominant transport mechanism in the silicon field effect transistor (FET) based sensors.

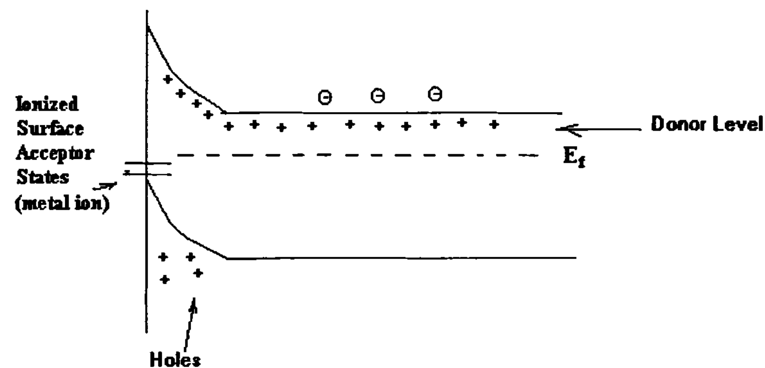

Figure 11: An inversion layer in an n-type metal oxide which has ionized acceptors, ionized donors and holes near the surface region.

The semiconducting metal oxide film structure is assumed to be polycrystalline, and therefore consists of several crystallites combined together as shown in Figure 6. Since intergranular boundaries appear in polycrystalline films, it is worthwhile to examine these boundaries more closely. In the present work it is assumed that the depletion region and the associated double layer as shown in Figure

9 occur. The surface of the crystallites are negatively charged with partially occupied surface acceptor states due to the surface metal ions. The positively charged donor ions in the depletion region are due to the oxygen vacancies. Figure 12 shows the charge distribution density in the depletion region.

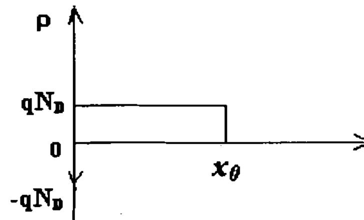

Figure 12: Charge distribution density in the depletion region. x_0 is the depletion region width.

The charge density in this region is given as follows:

$$\rho = qN_D; 0 \le x \le x_0$$

and (1)

$$\rho = -qN_D; x = 0,$$

where

N_D = concentration of oxygen vacancies in the metal oxide.

The separation of charge in the depletion layer causes an electric field and hence surface barrier potential to appear. In order to determine the variation of the potential, φ, across the depletion region one must solve the one-dimensional Poisson's Equation given as follows,

$$\frac{d^2\varphi}{dx^2} = -\frac{qN_D}{\varepsilon},$$

where (2)

ε = the metal oxide dielectric constant.

It is assumed that the doping is homogeneous and ε is homogenous, therefore N_D does not vary with x.

It is convenient to define a parameter, V, so as to be able to relate more directly to the band structure, as follows,

$$V(x) = \varphi_b - \varphi(x),$$

where (3)

φ_b = potential in the metal oxide bulk.

Solving equation (3) for $\varphi(x)$, substituting into equation (2) and integrating twice from x to x_0 using the two boundary conditions, $dV/dx = 0$ and $V=0$ at $x=x_0$, one obtains,

$$V(x) = \frac{qN_D}{2\varepsilon}(x - x_0)^2.$$

(4)

The surface potential, Vs , at $x=0$ then becomes

$$V_s = V\,|_{x=0} = \frac{qN_D}{2\varepsilon} x_0^{\,2}.$$

(5)

The variation of the potential across the depletion region is shown in Figure 13. Electrons must overcome the surface potential barrier to become free.

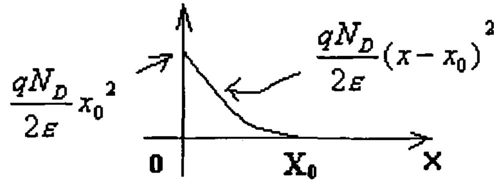

Figure 13 : Variation of the potential, V(x), across the depletion region.

Since a separation of charge occurs near the surface of the metal oxide, a space charge capacitance exists. The resulting capacitance can be approximated as a parallel plate capacitor and represented as follows,

$$C = \frac{\varepsilon A}{x_0}, \tag{6}$$

where ε is the dielectric constant and A is the contact area. Solving equation (6) for x_0 and substituting into equation (5) one obtains,

$$\frac{1}{C^2} = \frac{2V_s}{qN_D \varepsilon A^2}. \tag{7}$$

If a bias voltage, V , is applied across the depletion region equation (7) may be written as

$$\frac{1}{C^2} = \frac{2(V_s - V)}{qN_D \varepsilon A^2}.$$

(8)

It is interesting to note that if one plots $1/C^2$ as a function of V, two important parameters can be obtained, namely, the oxygen vacancy concentration, N_D, and the surface barrier potential, V_S.

Basically two types of conductivity can exist in a metal oxide semiconductor. In a single crystal with no surface states or surface barrier present the conductivity is given as follows,

$$\sigma_b = qN_D \mu_n,$$

(9)

where

N_D = donor density in the metal oxide (number of carriers per unit volume in the film)

And

μ_n = carrier mobility.

A surface conductivity arises when surface states are located at the semiconductor metal oxide surface. These surface states can cause a depletion , accumulation or inversion layer to appear at the surface which in turn modify the carrier concentrations. The surface conductivity, σ_s, may be defined as follows,

$$\sigma_s = qN\mu_n, \tag{10}$$

where

$N =$ the number of carriers at the surface per unit area of the film.

Basically the semiconducting metal oxide can be modeled as shown in Figure 14.

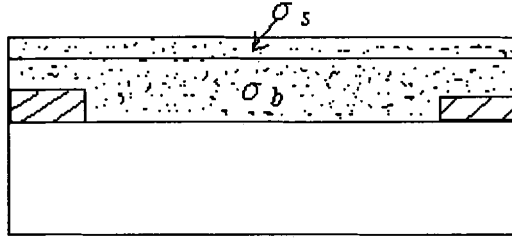

Figure 14: Model of the semiconducting metal oxide with surface and bulk film conductivities. The cross-hatched regions are electrodes, the dotted region is the film and the remaining area is the substrate.

Since the two conductances are in parallel, the overall sheet conductance, G, of this structure is given as,

$$G = G_s + G_b, \tag{11}$$

where

$$G_s \approx \frac{\sigma_s W}{l},$$

$$G_b \approx \frac{\sigma_b W t}{l},$$

$t =$ film thickness

$l =$ length of the layer between the electrode

and W = width of the film.

Between the two crystallite boundaries there forms a potential barrier, it may due to an inherent space charge region or due to the lack of periodicity of the crystallite. This barrier can be represented schematically for an n-type semiconductor in Figure 15. The grain size is L_1 and the grain boundary width is L_2.

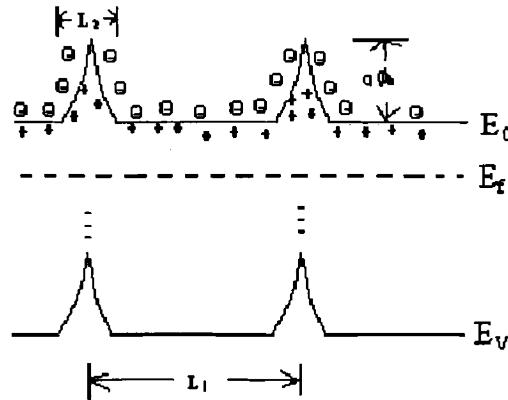

Figure 15: The energy band representation of an n-type polycrystalline semiconductor thin film with a grain size, L_1, and a grain boundary width, L_2. The grain boundary barrier potential is $q\phi_b$.

In the case of a single grain boundary between two crystallites the total resistivity, ρ_T, can be written as

$$\rho_T = \rho_B + \rho_C. \qquad (12)$$

where the ρ_B and ρ_C signify boundary and crystallite resistivities respectively. Normally, $\rho_B > \rho_C$, since the electron must overcome the double potential barrier

shown in Figure 15 in order to cross from one grain to another. This is further substantiated experimentally in Figure 16, which shows that the resistance, when measured across a crystallite or grain (essentially a small single crystal), is much lower at all temperature than the resistance across a single grain boundary.

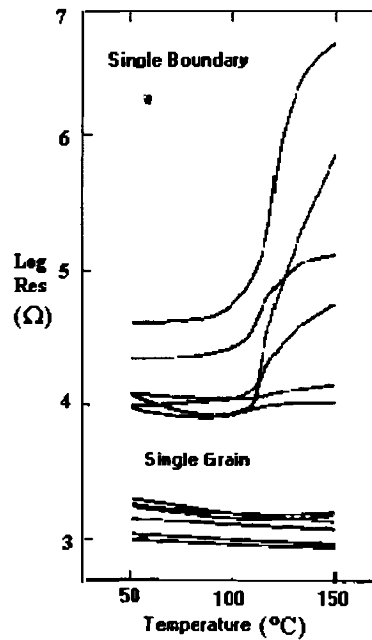

Figure 16: Resistance-temperature characteristics of single grains and single grain boundaries on a large grained ceramic [12]

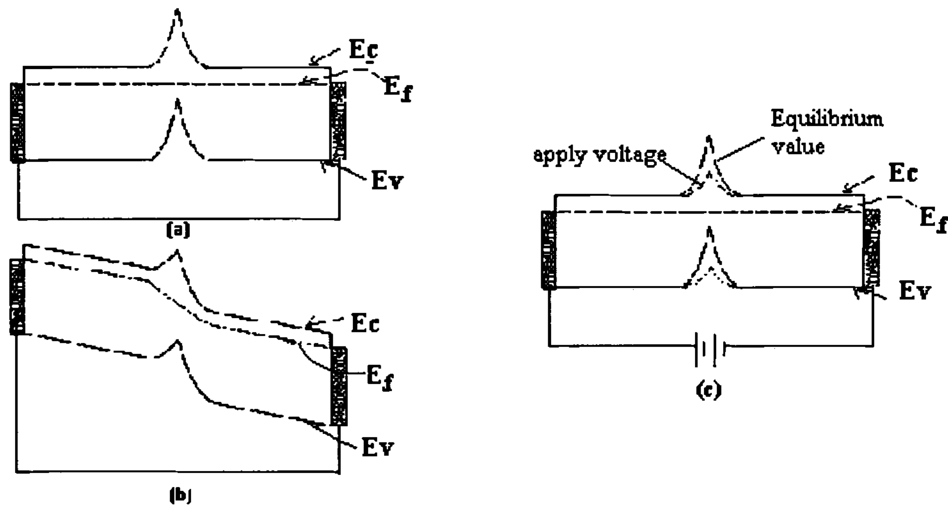

Figure 17: Band diagram illustrating band bending at grain boundary (a) two crystals have the same orientation in equilibrium (b) two crystals have different orientation in equilibrium (c) under applied voltage (the case of same orientation)(from Cohen et al.[14])

Generally, the different crystallite has different orientation which may result different surface band diagrams. In order to keep the continuity of the boundary the Fermi level will be tilted and the difference between the two conduction band will cause a potential barrier as presented in Figure 17b. But one may end up with a situation that all the crystallites have the same orientation which is presented in Figure 17a. If a potential is applied to the polycrystalline sample, the barrier height will decrease with the increase voltage as presented in Figure 17c. Generally speaking there are two ways for electrons to move across the crystallite boundaries. One way is for the electrons with sufficient kinetic energy to go over the potential barrier.This transport mechanism is also called thermionic emission. The other way is that when the width of potential barrier is small the electron will tunnel through the barrier. The

detailed information regarding different electron transport mechanisms will be presented in the metal-semiconductor junction part[Section 2.3.3]. If one assumes that the electron transport mechanism between the crystallites obeys the themionic emission, the current voltage relationship for the barrier can be expressed as [13],

$$j = Mn_1 \exp\left(-{q\phi_b}/{kT}\right)\left[\exp\left({q|V_b|}/{kT}\right)-1\right]. \tag{13}$$

where j is the current density, n_1 ,the mean majority carrier density in the grains, ϕ_b, the potential height of the barrier, $|V_b|$, the absolute voltage drop across the barrier, and M is a factor that is barrier height dependent. The derivation of this I/V relationship is similar to the themionic emission theory for the metal semiconductor junction which is given in Appendix B.

Since typically the resistivity of the grain boundary is much higher than that of the crystallite one could neglect the contribution from the crystallite and assume that all the applied voltage will appear across the crystallite boundaries. Considering that there are N_1 crystallites in series, if one applies a total voltage V across the film then the voltage across one crystal boundary, $|V_b|$, is

$$|V_b| = V / N_1 = V / nL, \tag{13a}$$

where n is the number of crystallites per unit length of the film and L is the length of the film in the direction of current flow.

Because of the many crystallite boundaries in the film the voltage drop across any one crystallite, $q|V_b|$, is small compared to kT, $0 < \frac{q|V_b|}{kT} < 1$ and

$0 < \exp\left(q|V_b| \Big/ kT \right) - 1 < 1$. Since $e^x = 1 + \frac{x}{1!} + \frac{x^2}{2!} + ...$, if $0<x<1$, x^2 is very small

and can be neglected then $e^x - 1 \approx x$. According to this approximation, equation (13) becomes

$$j \approx Mn_1 \exp\left(-q\phi_b \Big/ kT \right) \frac{q|V_b|}{kT}. \tag{13b}$$

Using equation (13a) and (13b), one obtains the total current:

$$I = jwd = Mn_1 \exp\left(-q\phi_b \Big/ kT \right) \frac{qVwd}{kTnL} \tag{13c}$$

where w and d are the width and thickness of the film respectively.

When a gas sorbs on a semiconductor and chemical kinetics occurs, a change in electron concentration takes place causing a change in the height of barrier potential. This in turn will effect the electron transport properties across the barriers and hence the current versus voltage characteristics(conductivity) of the film.

2.3 Metal Electrode Semiconductor Junction

2.3.1 Origins of the Schottky Barrier

The metal semiconductor junction between Pt and WO_3 forms what is commonly called a Schottky barrier. The earliest model put forward to explain this kind of barrier is due to Schottky and Mott [15,16]. According to this model, the barrier results from the difference in the work functions of the two materials. The energy band diagrams in Figure 18 represents the situation before the metal and

semiconductor are brought together. It is assumed that there are no charges at the surface, so the band structure of the surface is the same as that of the bulk. The work function of a metal, ϕ_m, is defined as the amount of energy required for an electron to go from the Fermi level to the vacuum level. The vacuum level is the energy level of the electron with zero kinetic energy just outside the metal. The work function, ϕ_s, of the semiconductor is defined similarly and is a variable quantity because the Fermi level in the semiconductor changes with the doping. Another important parameter that does not depend upon doping in the semiconductor is electron affinity, χ_s, which is defined as the energy difference between vacuum level and the lower edge of conduction band. The energy levels are usually expressed in electron volts *(eV)*.

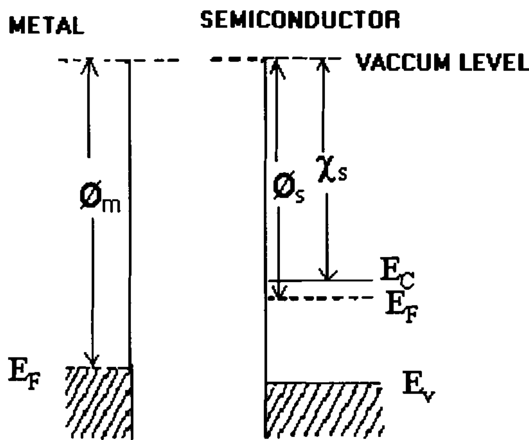

Figure 18: Electron energy band diagrams of metal contact to n-type semiconductor with $\phi_m > \phi_s$, and the materials separated from each other.

In a contact between two different materials, the electrons from the conduction band in one material, which have higher energy, flow into the other material until the Fermi level on the two sides are brought into coincidence. The energy levels in the two materials are rearranged relative to the new common Fermi

level. The electrons in the metal and semiconductor obey Fermi-Dirac statistics. Therefore the probability that an electron has an energy E , namely, $f(E)$, is defined as follows[17],

$$f(E) = \frac{1}{e^{E-E_f/kT} + 1},$$

(14)

where k is Boltzman's constant, T is the absolute temperature and E_f is the Fermi level of the material. The probability that a state is occupied by a hole is $f_p(E) = 1 - f(E)$.

There are two classes of metal and n-type semiconductor contacts. One is a contact between a metal and a semiconductor where the work function of the metal is greater than that of the semiconductor and the other is a contact between a metal and a semiconductor where the work function of the semiconductor is greater than that of the metal. The ϕ_s of WO_3 is unknown but typically the metal semiconductor junction is less than 3eV and the ϕ_m of platinum is 5.9eV[18], the contact between platinum and WO_3 may belong to the first class.

Figure 19 shows the energy band diagram after the contact is made and equilibrium has been reached and illustrates the process of barrier formation.

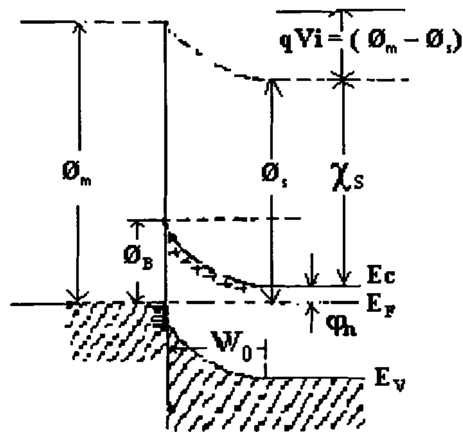

Figure 19: Electron energy band diagrams of metal contact to n-type semiconductor with $\phi_m > \phi_s$ in thermal equilibrium after the contact has been made.

W_0 is the width of the depletion region. Because electrons in the conduction band of the semiconductor have a higher energy than electrons in the metal, the electrons will move from the semiconductor side to the metal. As the electrons move out of the semiconductor, the free electron concentration in the semiconductor region near the Pt/semiconductor interface decreases. Since the separation of E_C (conduction band edge) and E_F (Fermi level) increases with the decreasing electron concentration, and in thermal equilibrium E_F remains constant, the conduction band will bend up as shown in Figure 19. The conduction band electrons which cross over into the metal leave a positive charge of ionized donors or oxygen vacancies behind, so the semiconductor region near the metal is depleted of mobile electrons. Thus a positive charge is established on the semiconductor side of the interface and the electrons which cross over into the metal form a negatively charged surface atomic layer. This is due to the fact that the electron concentration of the negative electronic charges from the semiconductor is small compare to the concentration of free charge

electrons in the bulk of the metal. Therefore the negative electronic charges will remain at the surface of the metal instead of diffusing into the bulk. As a result an electric field is established from the semiconductor to the metal. The width of the space charge layer in the semiconductor is appreciable because the donor concentration in the semiconductor is several orders of magnitude smaller than the free electron concentration in the metal.

Let us investigate how much the energy bands in the semiconductor will bend up. It should be evident that since the band gap of the semiconductor is not changed by making contact with the metal, the valence band edge E_V will move up and is parallel to the conduction band edge, E_c. Also because the electron affinity of the semiconductor is assumed to remain unchanged even after the metal contact is made the vacuum level in the semiconductor will follow the same variations as E_c. Thus, for a metal-semiconductor system in thermal equilibrium the important point which determines the barrier height is the fact that the vacuum level on the semiconductor side must approach the vacuum level on the metal side. The amount of band bending is equal to the difference between the two work functions. This difference is given by qV_i, where V_i is known as the contact potential difference or the built-in potential of the barrier. Electrons moving from the semiconductor into the metal have to climb over this barrier. However, the barrier looking from the metal toward the semiconductor is different and is given by

$$\phi_B = \phi_m - \chi_S . \tag{15}$$

Since

$$\phi_s = \chi_s + \phi_n, \tag{16}$$

solving equation (16) for χ_s and substituting into equation (15) and noting that $qV_i = \phi_m - \phi_s$, one obtains

$$\phi_B = (qV_i + \phi_n). \tag{17}$$

Let us examine the barrier under bias voltage. Figure 20a represents the thermal equilibrium energy band diagram of the contact. At equilibrium, there is no net current flow because the rate of electrons moving from the metal to the semiconductor and from the semiconductor to the metal are balanced. The applied voltage will change the equilibrium band diagram by changing the total curvature of the bands and at the same time modifying the potential drop across the depletion region. When the forward voltage V_F is applied that means the semiconductor is negative relative to the metal, the voltage across the depletion region is reduced to V_i-V_F as shown in Figure 20(b) and the corresponding depletion width is reduced.

The electrons on the semiconductor side see a reduced barrier and as a result the electron flux from the semiconductor towards the metal is increased above its value under thermal equilibrium. The electron flux from the metal to the semiconductor is not changed because ϕ_B is unchanged by the bias voltage. Noting that the traditional definition of current flow is opposite to electron flow, a net current flows from the metal to the semiconductor.

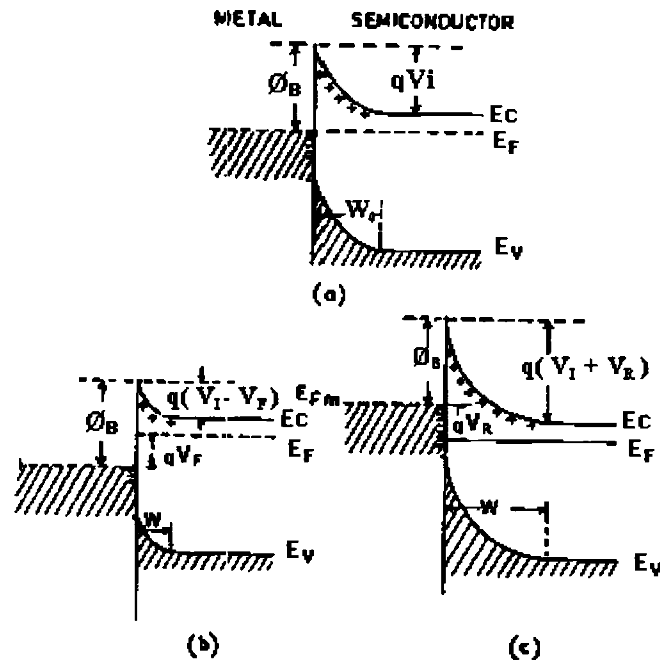

Figure 20: Electron energy band diagrams of a metal contact on an n-type semiconductor (a) thermal equilibrium (b) forward bias (c) reverse bias.

For the reverse bias contact, the semiconductor is biased positively with respect to the metal by a voltage $-V_R$, the potential drop across the depletion region is increased to (V_i+V_R) as shown in Figure 20(c) and the corresponding depletion width is increased. The electron flow from the semiconductor toward the metal is further impeded while the flow from the metal toward the semiconductor is unaffected. Then leads to a current flowing in the opposite direction. Typically the current transport in metal-semiconductor barriers is mainly due to the majority carriers. But for large barrier heights and low dopant concentrations the injection of minority carriers from the semiconductor into metal may become important for reverse bias. [19]

2.3.2 Electric Field and Potential Distribution in the Depletion Region

Figure 21 shows the energy band diagram of a reverse biased Schottky barrier junction made on an n-type semiconductor. The semiconductor is assumed to be uniformly doped and divided into a space charge region and a neutral region devoid of any space charge.

The electric field and potential distribution, $\phi(x)$, in the depletion region of the Schottky barrier junction depends upon the barrier height, the applied voltage, and the impurity concentration. The electric field and $\phi(x)$ can be obtained by the solution of the one-dimensional Poisson's equation, which can be written as follows,

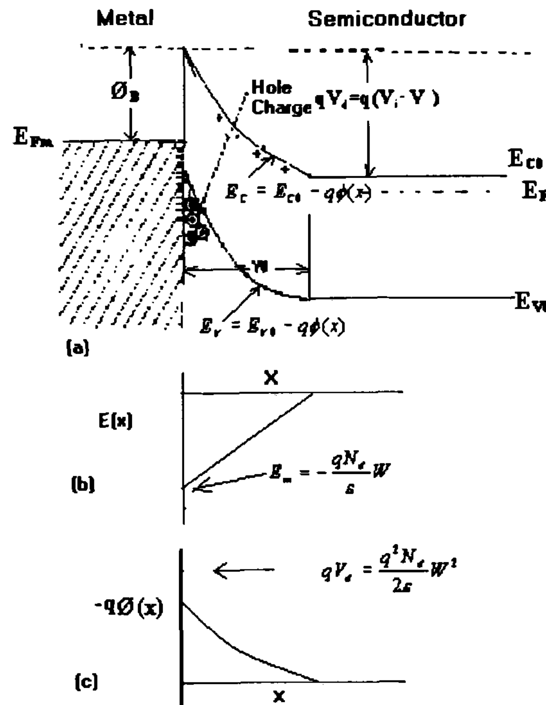

Figure 21: Electric field and potential distributions in the depletion region of a Schottky barrier. (a) Energy band diagram; (b) electric field distribution; and (c) potential distribution. V is the applied voltage. [20]

$$\frac{d^2\phi}{dx^2} = -\frac{q}{\varepsilon}\left[N_d + p(x) - n(x)\right]$$

(18)

In equation (18), ε is the semiconductor permittivity, N_d is the donor concentration or concentration of oxygen vacancies, and *n(x)* and *p(x)* are the electron and the hole concentrations at any point x in the semiconductor, respectively. It is assumed that all the donor are ionized. Referring to equation (14), if E_C-E_f>>kT, the probability function that a state is occupied by an electron can be simplified as follows,

$$f(E) = \exp\left[-\left(E - E_f\right)/kT\right];(E_c - E_f >> kT)$$

(19)

The probability that a state is occupied by a hole can be approximated as,

$$f_p(E) = \exp\left[-\left(E_f - E\right)/kT\right];(E_f - E_V >> kT)$$

(20)

The electron concentration, *n(x)* , in the conduction band may be written as follows,

$$n(x) = \int_{E_c}^{\infty} f(E)g(E)dE.$$

(21)

g(E) is the density of electronic states [21]defined as

$$g(E) = \frac{4\pi(2m^*)^{3/2}E^{1/2}}{h^3},$$

(22)

where m^* is the carrier effective mass and h is the Plank's constant.

The corresponding hole concentration, $p(x)$, in the valence band may be written as,

$$p(x) = \int_0^{E_v} f_p(E) g(E) dE. \tag{23}$$

If one subtracts and adds Ec in the exponential term for $f(E)$ and subtracts and adds E_V in the exponential term for $f_p(E)$, one obtains,

$$n(x) = N_c \exp\left[-\frac{(E_c - E_F)}{kT}\right]$$

and (24)

$$p(x) = N_v \exp\left[-\frac{(E_F - E_v)}{kT}\right],$$

where

$$N_c = \int_{E_c}^{\infty} \exp\left[-\frac{E - E_c}{kT}\right] g(E) dE = 2\left(\frac{2m_e \pi kT}{h^2}\right)^{3/2}$$

and

$$N_v = \int_0^{Ev} \exp\left[-\frac{E_v - E}{kT}\right] g(E) dE = 2\left(\frac{2m_p \pi kT}{h^2}\right)^{3/2}.$$

m_e and m_p are the effective masses of the electron and hole respectively.

In the depletion region E_c and E_V are defined in terms of the potential distribution as follows,

$$E_c = E_{c0} - q\phi(x),$$

and (25)

$$E_V = E_{V0} - q\phi(x),$$

where E_{c0} = conduction band level in the bulk semiconductor

and E_{V0} = the valence band level in the bulk semiconductor.

Substituting E_c and E_V into equation (24) one obtains

$$n(x) = N_c \exp\left(-\frac{E_{c0} - q\phi(x) - E_F}{kT}\right) = n_0 \exp\left(\frac{q\phi(x)}{kT}\right).$$

$$p(x) = N_V \exp\left(-\frac{E_F - (E_{V0} - q\phi(x))}{kT}\right) = p_0 \exp\left(-\frac{q\phi(x)}{kT}\right).$$

where (26)

$$n_0 = N_c \exp\left(-\frac{E_{c0} - E_F}{kT}\right).$$

and

$$p_0 = N_v \exp\left(-\frac{E_F - E_{v0}}{kT}\right).$$

It is interesting to note that n_0 and p_0 represent the equilibrium electron and hole concentrations in the neutral semiconductor.

Substituting the values of $n(x)$ and $p(x)$ given in equation(26) into equation(18) one obtains

$$\frac{d^2\phi}{dx^2} = -\frac{q}{\varepsilon}\left\{N_d - n_0 \exp\left[\frac{q\phi(x)}{kT}\right] + p_0 \exp\left[-\frac{q\phi(x)}{kT}\right]\right\}. \tag{27}$$

A closed form solution of this equation is impossible. An additional simplifying assumption made in the analysis is the so-called depletion approximation. In this approximation the free carrier concentrations are assumed to fall abruptly from their equilibrium values, n_0 and p_0 in the bulk neutral semiconductor region, to a negligibly small value in the space charge region. In reality this transition occurs smoothly over a distance in which the bands bend but the calculations made using the depletion approximation are sufficiently accurate for our purposes. Thus, equation (27) can be approximated as

$$\frac{d^2\phi}{dx^2} = -\frac{q}{\varepsilon}N_d; (0 < x < W), \tag{28}$$

where W represent the width of the depletion region. Integrating equation (28) with respect to x and using the condition that $d\phi/dx = 0$ at $x=W$ one obtains the following expression for the electric field $E(x)$, in the depletion region,

$$E(x) = -\frac{d\phi}{dx} = E_m\left(1 - \frac{x}{W}\right), \tag{29}$$

where

$$E_m = -\frac{qN_d}{\varepsilon}W.$$

E_m is the maximum electric field which occurs at $x = 0$. A second integration with the boundary condition $\phi = 0$ at $x = W$ leads to the following relation,

$$\phi(x) = -\frac{qN_d}{2\varepsilon} W^2 \left(1 - \frac{x}{W}\right)^2 . \tag{30}$$

The negative sign in the above equation shows that the potential at $x=0$ is negative with respect to that at $x=W$. The variations of $E(x)$ and $\phi(x)$ into depletion region are shown in Figure 21. If one applies a voltage across the potential barrier, the height of the potential barrier will either increase or decrease depending upon the voltage bias. According to Figure 21, the surface potential barrier and the applied voltage relationship can be expressed as $-\phi(0) = V_d = V_i - V$. Substituting into equation (30) one obtains

$$V_d = (V_i - V) = -\phi(0) = \frac{qN_d}{2\varepsilon} W^2 . \tag{31}$$

Depending upon whether the bias is forward ($V = V_F$) or reverse ($V = -V_R$) the depletion width will change. Solving equation (31) for the depletion width one obtains

$$W = \sqrt{\left(\frac{2\varepsilon}{qN_d} |Vi - V|\right)}. \tag{32}$$

The width of the depletion region at zero bias, W_0, is obtained by setting $V = 0$. From equation (32) it is obvious that W decreases below its equilibrium value of W_0 in case of a small forward bias($<V_i$) and increases above W_0 in the case of a reverse bias.

Since a separation of charge occurs near the metal semiconductor junction a space charge capacitance exists. This can be approximated as a parallel plate capacitor whose separation between the two plates is equal to the depletion width W. The relationship is as follows,

$$C = \frac{S\varepsilon}{W}. \tag{33}$$

where S is the contact area of metal and semiconductor junction .

If one applies a voltage, the width of the depletion region will change according to equation (32) resulting in a corresponding change in capacitance. This is particularly significant in the AC case.

2.3.3 Current Voltage Characteristics

Electrical current in a semiconductor arises from the movement of electrons and holes upon application of a voltage. The electrical current, in general, can be divided into two types, the drift current and the diffusion current. The drift current is the hole and/or electron current which arises from the application of an external electric field or voltage and can be represented as follows,

$$J_n = e\mu_n nE$$

and (34)

$$J_p = e\mu_p pE.$$

μ_n and μ_p are the mobilities of the electrons and holes respectively. The second type of current is called the diffusion current. This current results from a large concentration of electrons or holes which may have been created by an external source such as heat or light. These electrons or holes then diffuse through the material giving rise to the diffusion current. The diffusion currents are proportional to the spatial gradient of the carrier concentration as given below,

$$J_n = eD_n \nabla n$$

and (35)

$$J_p = -eD_p \nabla p,$$

where the terms D_n and D_p are the diffusion constant for electrons and holes respectively.

In general, the current in a semiconductor is the sum of both the drift and diffusion currents and may be written as follows,

$$J = J_{drift} + J_{diffusion},$$

where

$$J_{drift} = e(\mu_n n + \mu_p p)E$$

and (36)

$$J_{diffusion} = e(D_n \nabla n - D_p \nabla p)$$

It is interesting to point out for the diffusion current the electrons and holes are moving in the same direction whereas for the drift current the electrons and holes are moving in opposite directions.

In the case of the PN junction, the acceptor atoms on the p-type material introduce holes which are the majority carriers while the donor atoms on the n-type material introduce electrons which are the majority carriers. If one applies a voltage, there is majority carrier flow (electron flow from n-type material to p-type material and hole flow from p-type material to n-type material) and minority carrier flow (electron flow from p-type material to n-type material and hole flow from n-type material to p-type material. The carrier diffusion and drift are the dominant mechanisms in a PN junction. Assuming that when an external voltage is applied, a small change in minority carriers is more noticeable than a corresponding charge in majority carriers, it may be shown that the I/V relationship in a PN junction based on diffusion and drift theory is as follows[22],

$$I = I_s\left[\exp\left(\frac{eV}{kT}\right) - 1\right]$$

where (37)

$$I_s = A\exp\left[\left(\frac{D_n}{L_n N_a} + \frac{D_p}{L_p N_d}\right)n_i^2\right].$$

I_s is called the saturation current, A , is the diode cross-section area, n_i is the intrinsic carrier concentration, L_n and L_p are the depletion widths in the n-type material and p-type materials respectively and N_d and N_a are the donor and acceptor concentration in the n and p type materials respectively.

In the case of a metal semiconductor junction, the electron concentration in the metal is very high and there are no holes in the metal. In the n-type semiconductor, the majority carriers are electrons while the minority carriers are the holes. The current transport in metal semiconductor barriers is due mainly to majority carriers in contrast to PN junction where the minority carriers are responsible. As mentioned before, a depletion region is formed between the metal and semiconductor interface. Referring to equation (32), the depletion width is determined by the concentration of donors or oxygen vacancies in the semiconductor. When depositing the metal oxide film using R.F magnetron sputtering, the donor concentration can be controlled by changing the Argon/Oxygen ratio in the deposition chamber. The depletion width varies from zero to infinity depending on the donor concentration. The resulting junctions which occur are the metal-insulator junction (stoichiometric metal oxide and no oxygen vacancies present), the metal- n-type semiconductor junction (substoichiometric metal oxide with oxygen vacancies present)and the metal-metal junction (no oxygen present in the deposition process). For the metal-insulator junction there will be no current, and for the metal-metal junction the contact is ohmic.

For the metal - n-type semiconductor junction, if the donor concentration is not very high, the depletion layer thickness may be large compared to the mean free path. The mean free path is defined as average of the distances traveled between two successive collisions for a single particle undergoing Brownian motion for scattering of the electrons by lattice vibrations. The electrons make many collisions as they transverse the depletion region and the electron current through the layer is due to the drift velocity. If the donor concentration is high the corresponding barrier layer width given by equation(32) decreases and can be comparable with the mean free path of the carriers. The electrons which have enough energy will go over the barrier and this transport mechanism is called thermionic emission. In this theory the collisions of carriers with the lattice are neglected and the electrons are treated according to Maxwell-Boltzman statistics . Thermionic emission is usually the dominant mechanism in Schottky barrier junctions and leads to the ideal diode charactersistics which has a constant reverse saturation current. If the semiconductor is heavily doped the corresponding width of barrier is very thin and the carriers can tunnel through rather than cross over the potential barrier. This tunneling can occur at the beginning of the depletion region or a particular distance into the depletion region. This may be seen by refering to Figure 21. As the electrons acquire more energy the barrier become increasingly thin and tunneling may occur at different barrier heights. One concludes that the depletion width is the critical parameter which will decide which electron transport theory is the most appropriate. Since the depletion width can be controlled by the argon oxygen ratio in the sputtering system, one can specifically deposit a film which will obey a particular electron transport theory.

In their original work , Schottky and Spenke[16] assumed that the current was limited by the drift and diffusion process. The diffusion theory is derived from the assumption that (1) the barrier height is much larger than kT; (2) the effect of electron collisions within the depletion region is included; (3) the carrier concentration at $x=0$ and $x=w$ are unaffected by the current flow.

Since the current in the depletion region depends on the local field and the gradient of carrier concentration, it may be shown [23] that diffusion theory leads to the following expression for the diode current,

$$I = \left\{ \frac{q^2 D_n N_c}{kT} \left[\frac{q(V_i - V)2N_d}{\varepsilon} \right]^{1/2} \exp\left(-\frac{q\phi_B}{kT} \right) \right\} \left[\exp\left(\frac{qV}{kT} \right) - 1 \right] = I_0 \left[\exp\left(\frac{qV}{kT} \right) - 1 \right] \tag{38}$$

D_n is the electron diffusion constant, N_c is the effective density of states in the conduction band of the semiconductor, and all other symbols have their usual meanings. Note that the saturation current , I_0, in equation(38) is dependent upon the voltage. The details of the derivation of this I/V relationship is given in Appendix A.

When thermionic emission is the dominate mechanism, the effect of drift and diffusion in the depletion region is assumed to be negligible,the barrier height is assumed to be large compared to kT and the electron collisons wihin the depletion region are neglected. It is obvious that only those electrons whose kinetic energy exceed the height of the potential barrier will be able to reach the top of the barrier. According to thermionic emission theory, it may be shown [20] that the current voltage relationship is as follows,

$$I = I_0\left[\exp\left(\frac{qV}{kT}\right) - 1\right],$$

where (39)

$$I_0 = SAT^2 \exp\left(-\frac{\phi_B}{kT}\right).$$

(40)

A is the Richardson constant for thermionic emission from the metal into the semiconductor defined as

$$A = \frac{4\pi m^* qk^2}{h^3}.$$

m^* is the electron effective mass, h , Planck's constant and S , the metal semiconductor contact area . The derivation of equation (40) is given in Appendix B.

In the original treatment of Bethe [24] it was assumed that once the electrons reach the top of the barrier they are emitted into the metal and do not return back to the semiconductor. Crowell and Sze [25] refined the theory by including the effects of optical phonon scattering in the metal and quantum mechanical reflections from the barrier. An electron after passing over the barrier into the metal may be scattered back to the semiconductor after the emission or absorption of an optical phonon, with a subsequent reduction in the diode current. Moreover not all the electrons incident over the barrier will cross over into the metal. According to quantum mechanics there is a finite probability that an electron with kinetic energy larger than the barrier potential energy may be reflected back into the semiconductor. Also an electron with energy less than the barrier energy has a finite probability of tunneling through the barrier. Crowell and Sze have calculated the probability , fp , of an electron reaching

the metal without scattering into the semiconductor and also the probability , fq , of its transmission through the barrier in the presence of quantum mechanical reflection and tunneling. They have concluded that the combined effect of these processes and the carrier diffusion effects in the depletion region results in replacing the Richardson constant, A, in equation (40) by an effective value $A*$ given by

$$A^{*} = \frac{Af_p f_q}{1 + f_p f_q \, {V_R}/{V_D}}. \tag{41}$$

where V_D is the effective diffusion velocity through the depletion region and V_R is defined as the recombination velocity.

Thermionic emission theory predicts the current voltage characteristics in equation (39), however, a wide variety of practical metal semiconductor diodes follow the following I/V relationship,

$$I = I_0\left[\exp\left(\frac{qV}{nkT}\right) - 1\right], \tag{42}$$

where n is often called the "ideality factor". In the case of an ideal Schottky barrier where the barrier height is independent of the bias and the current flows only due to thermionic emission n=1.

A value for the ideality factor can be obtained as follows. When a bias voltage is applied, the barrier height is modified as can be seen in Figure 21. Assuming that the barrier height is proportional to bias voltage, Φ_B, can be represented as follows,

$$\phi_B = \phi_{B0} + \beta q V. \tag{43}$$

where Φ_{B0} is the zero bias barrier height, β is an unknown parameter and V is taken to be positive in the case of forward bias.

Under the condition of forward bias, assuming a sufficient large forward bias so that the unity term in equation (39) can be neglected with respect to the exponential term, and making use of equation (40) and (43) and replacing A by A*, the forward current I can be written as

$$I = SA^*T^2 \exp\left(-\frac{\phi_{BO}}{kT}\right)\exp\left[\frac{q}{kT}(1-\beta)V\right]. \qquad (44)$$

If one assumes that $1/n = (1-\beta)$ equation (44) is of the same form as equation (42) with $I_0 = SA^*T^2 \exp\left(-\frac{\phi_{BO}}{kT}\right)$. Taking the derivative of both sides of equation (43) with respect to V one obtains $\beta = \left(\partial\phi_B / q\partial V\right)$ therefore $\frac{1}{n} = \left(1 - \frac{\partial\phi_B}{q\partial V}\right)$. Hence if $\partial\phi_B / \partial V$ is known as a function of bias the ideality factor n can be calculated.

Figure 22 shows the current voltage relationship predicted by equation (42) for different values of n.

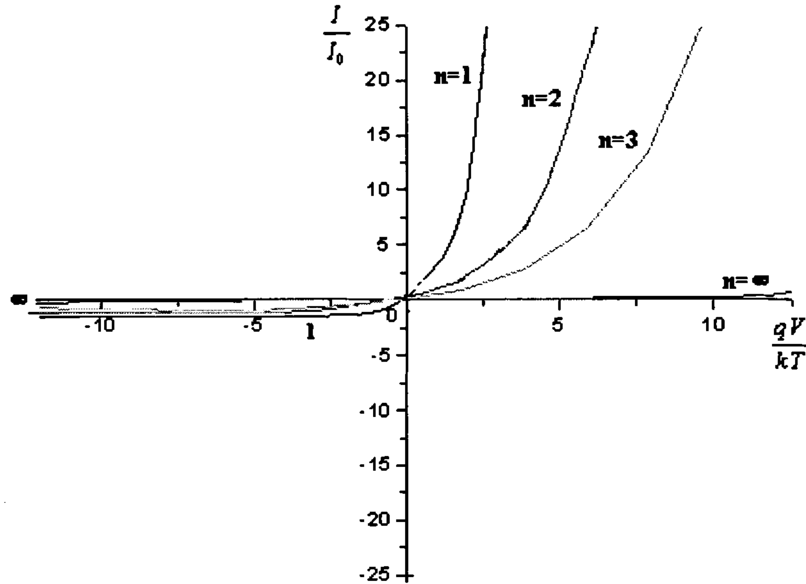

Figure 22: Normalized current voltage characteristics for thermionic emission which is predicted by equation 42. I/I_0 is the normalized current.

In addition to the diffusion and thermionic emission mechanisms, electrons can also be transported across the barrier by quantum mechanical tunneling. There are two ways for electrons to tunnel through the Schottky barrier junction :(1) field emission(FE), this happened when the depletion region is very thin, the electron with energy level close to the Fermi level will tunnel from the semiconductor to the metal and (2) when the temperature is high enough a significant number of electrons are able to rise high above the Fermi level where they can see a thinner and lower barrier, these electrons can then tunnel into the metal before reaching the top of the barrier. This tunneling of thermally excited electrons is known as the thermionic field emission (TFE).

To calculate the tunneling current, the electrons in the conduction band cannot be treated as classical particles but behave as waves. In order to derive the tunneling current one must solve the time independent Schrödinger equation,

$$\nabla^2\psi + \frac{2m}{\hbar^2}(\varepsilon - V)\psi = 0 \tag{45}$$

where $\hbar = h/_{2\pi}$ (h is Planck's constant), m is mass of particles, V is potential energy, ε is the electron energy and ψ is the wave function.

In order to solve Schrödinger equation one needs to substitute the appropriate potential function into equation(45) and solve the equation subject to the various boundary conditions. Normally,one can not get an exact solution and must use approximation techniques such as the WKB approximation [26] to solve the problem.

If one uses the WKB method it has been shown by Rideout and Crowell[25] and J.L.Moll[27] that the I/V characteristics for the tunneling effect may be written as follows,

$$I = I_0\left\{\exp\left(\frac{qV}{nkT}\right) - \exp\left[\left(\frac{1}{n} - 1\right)\frac{qV}{kT}\right]\right\}. \tag{46}$$

where $I_0 = I_m \exp[-q(\varphi_b - \varphi_s)/nkT]$ is the saturation current with φ_b being the metal work function and φ_s the semiconductor work function. I_m is the current density which is a slowly varying function of temperature [25] and n is the ideality factor. The factor, n, is an adjustable parameters which is used to fit the experimental data to the theoretical prediction. Figure 23 shows the current voltage relationship predicted by equation (46) for different values of n.

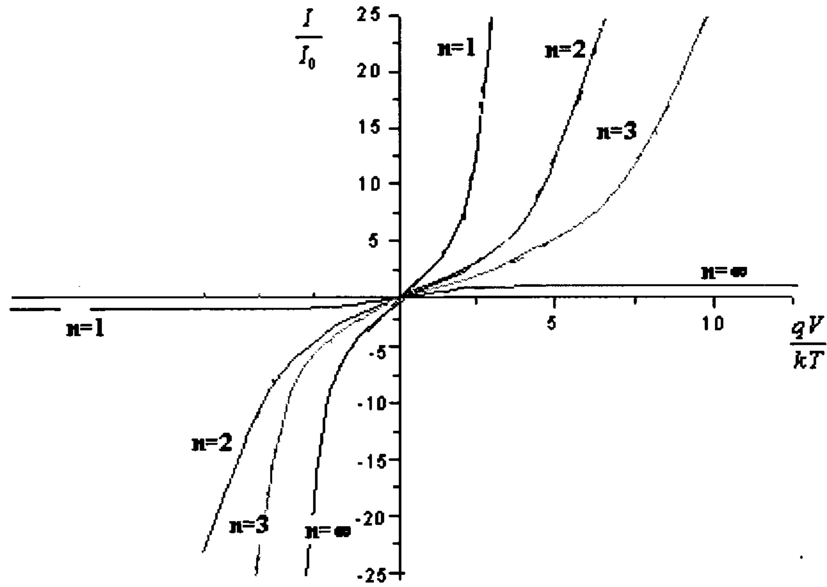

Figure 23: Normalized current voltage characteristics predicted by equation 46. I/I_0 is the normalized current.

At this point it is interesting to compare the thermionic emission and tunneling effect models. When n is chosen to be 1, equation (46) due to the tunneling reduces to equation (39) , which is the ideal case of the Schottky diode. Note that the n=1 curves in Figures 22 and 23 are identical. If n is greater than 1, the current voltage characteristics for both cases deviate. Figure 24 shows the comparison of the I/V characteristics for $n=2$, $n=3$ and $n=\infty$.

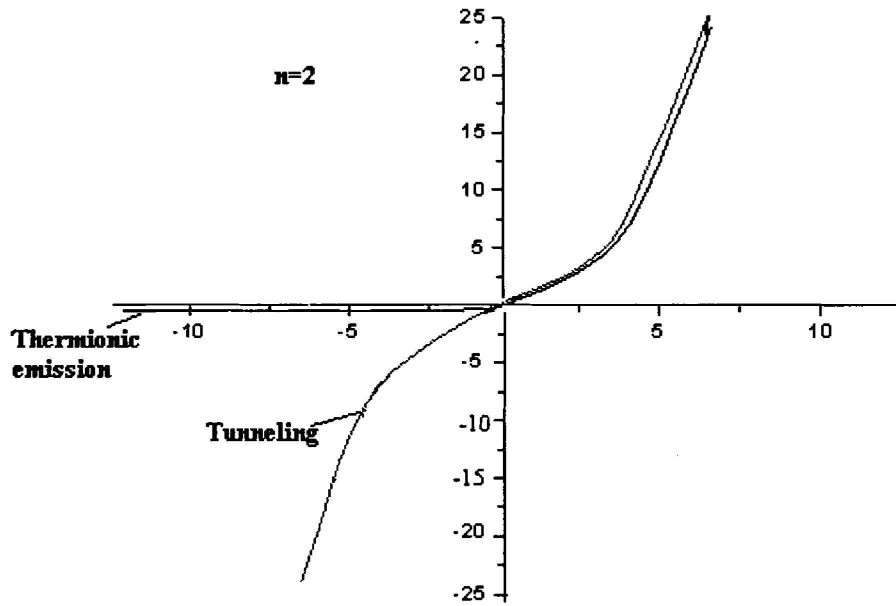

(a)

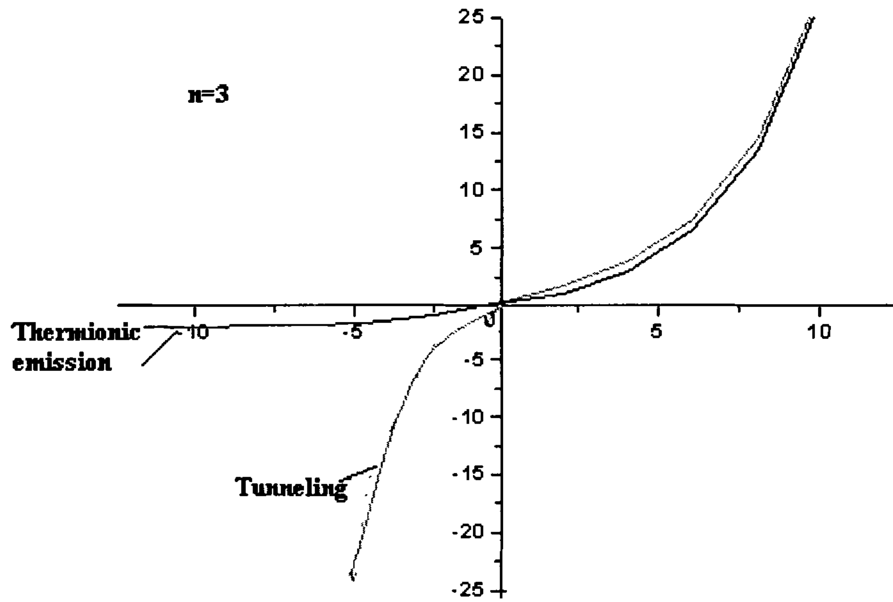

(b)

Figure 24:The comparison of I/V characteristics of thermionic emission and tunneling effect with different n values. (a) n=2, (b) n=3 and (c) n=∞.

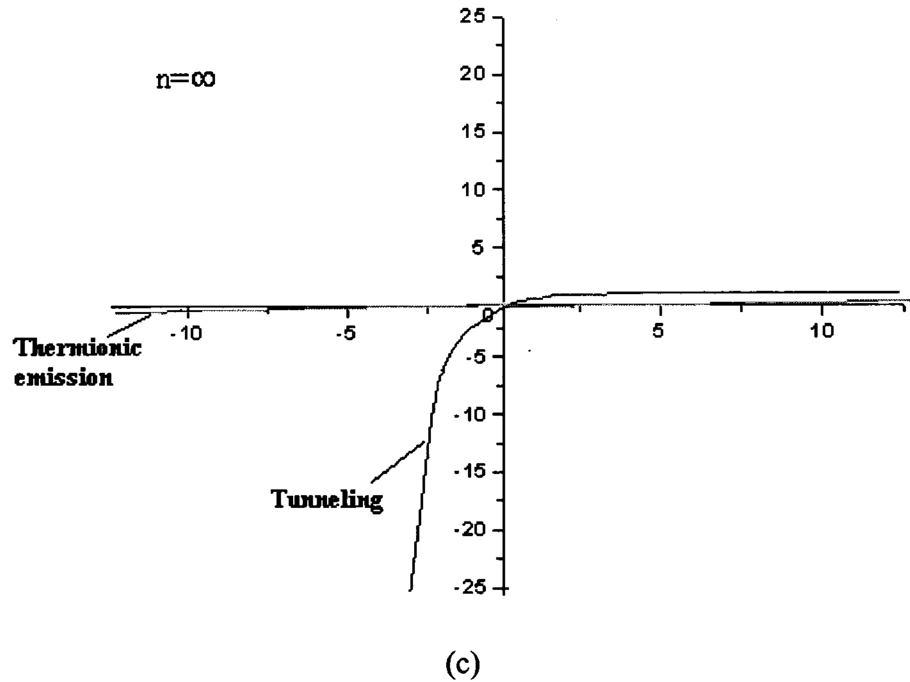

(c)

Figure 24 continues.

From the shape of the I/V characteristics, the major difference between the thermionic emission and tunneling models is the reverse bias part. The shape of the forward bias is almost the same. Since there are large difference for the reverse voltage, one may distinguish the different transport mechanism by examining the reverse bias I/V curve.

2.4 Equivalent Circuit Model

After examining the electron transport mechanisms between crystallites and across the metal electrode semiconductor junctions, a simplified equivalent circuit was used to simulate the current voltage characteristics of the SMO sensor. Figure 25 shows the diagram of the equivalent circuit in the DC case.

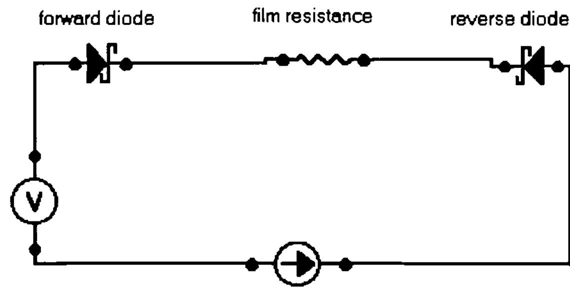

Figure 25: Equivalent circuit model for the SMO sensor in the DC case.

Because a resistance ladder network can be used as an equivalent circuit for semiconducting metal oxide film, one can combine the resistance together and call it a film resistance. As mentioned before, the I/V characteristics of a semiconducting metal oxide may not be linear. In addition to the effect of film resistance, one must take into account the effect of the metal electrode semiconductor contact which can be modeled using two back to back Schottky diodes as shown in Figure 25.

3. EXPERIMENTAL PROCEDURE FOR THE MEASUREMENT OF THE I/V CHARACTERISTICS OF WO_3 THIN FILM SENSORS

In this chapter the current versus voltage measurement techniques and system used to determine the I/V characteristics of a WO_3 thin film sensor is presented. The system consists of two parts, a gas delivery system and a data acquisition system.

3.1 Current versus Voltage Measurement Techniques

Currently, there are three methods commonly used to measure the current versus voltage characteristics in a thin film. These methods are the two-probe current-voltage measurement, the four-probe current-voltage measurement and the three-probe current-voltage measurement method. According to the name of the measurement, the two-probe measurement means two wires actually connected to the two electrodes of the physical device. Figure 26 shows the schematic of the two-probe configuration. The four-probe measurement uses two independent contact pairs, one for applying the calibrated current and the other pair for measuring the voltage. Figure 27 shows the configuration and equivalent circuit for the four-probe measurement. The three-probe measurement uses an additional microelectrode between the two electrodes and is shown schematically in Figure 28. Using the three-probe measurement method, Weimar et al. [27] deduced that the metal electrode semiconductor contact influence is the origin of the non-ohmic current versus voltage behavior of the SnO_2 sensor. The advantage of the four-point probe measurement is that it is possible to eliminate the contact contribution. The two-point probe

measurement is the most commonly used method and it is easy to setup. In our present work, the objective is to study the I/V characteristics of the entire sensor therefore the two-point probe measurement is the most appropriate techniques.

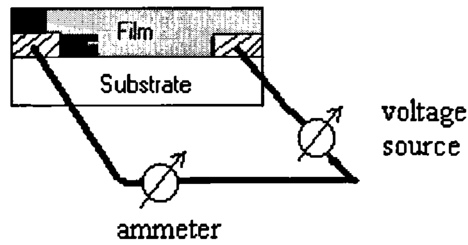

Figure 26: Two probe measurement of the WO_3 sensor.

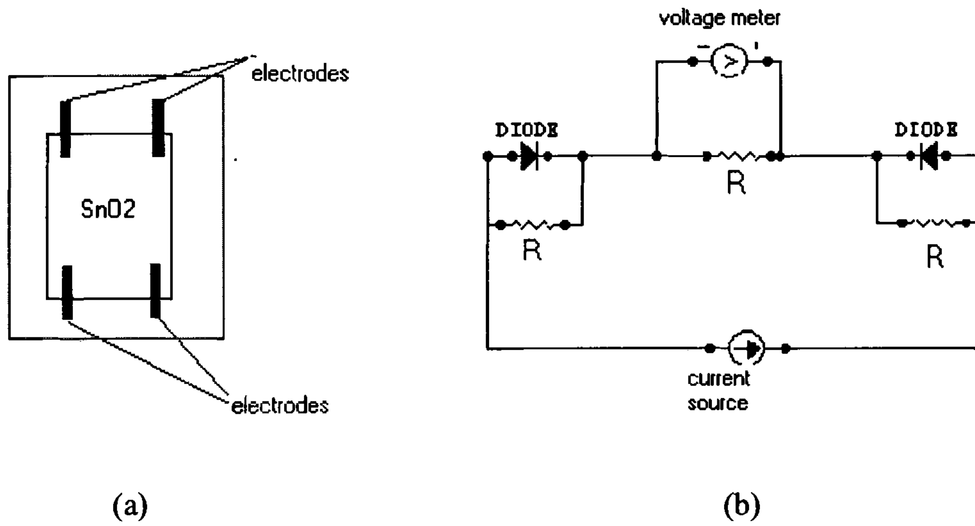

Figure 27: (a) Four-probe measurement of an undoped SnO_2 sensor. (b) Equivalent circuit for Four-probe measurement.[27]

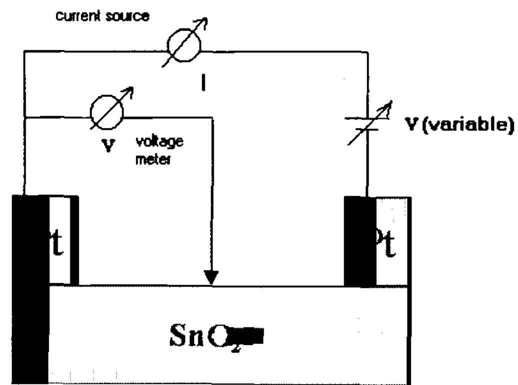

Figure 28: Three-probe arrangement to measure the contact contribution.[27]

The SMO film and appropriate contacts can be made in several configurations. These configurations are shown in Figure 29.

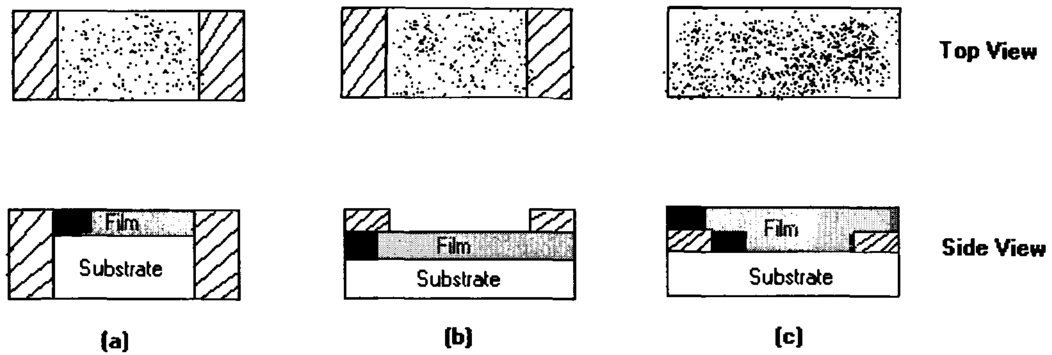

Figure 29: Different configurations used to model the conductimetric sensor. Cross-hatch region – electrodes; shaded region – sensing film; White region – substrate.

The configuration used in the present work is shown in Figure 29(C). This kind of configuration protects the electrodes from external contamination. The two

possible ways to connect the meter to the electrodes for I/V measurements are shown in Figure 30.

Figure 30 : Two possible circuit configurations for conductivity measurement.

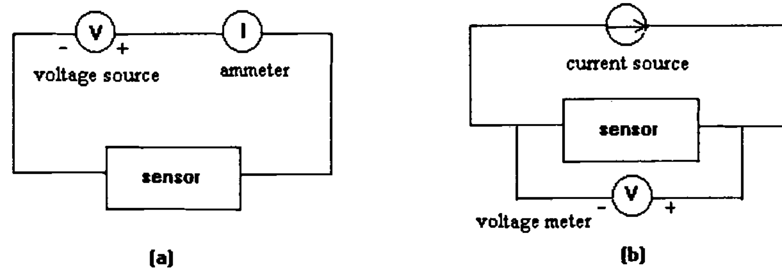

In the conductivity or resistivity measurement, Figure 30(a) is a constant voltage source measurement. The build-in resistances for both voltage source and the ammeter are very close to zero ohms. Since the sensor is a high resistance device most of the voltage drop is across the sensor. Figure 30(b) is a constant current source measurement setup. Ideally the voltage meter has infinite resistance. However, in reality the voltage meter has high resistance. Since the resistance of the voltage meter may be comparable to the sensor resistance, the resistance one measures using this method may not be equal to the sensor resistance. In order to avoid this error the constant voltage source is the one that is used in the present work. A constant voltage is supplied to the sensor electrodes and the current through the sensor is measured from which one calculates the sensor resistance according to Ohm's law. The range of voltage used is between –20V and 20V, in increments of 10mV. In order to observe the hysteresis of the current voltage characteristics, the voltage source goes from –20V to 20V, and then from 20V to –20V.

In the AC case, a similar approach can be used to measure the impedance of SMO sensors by replacing the DC voltage source and ammeter with the frequency generator and the meter to measure the impedance. Figure 31 shows the diagram for AC measurement.

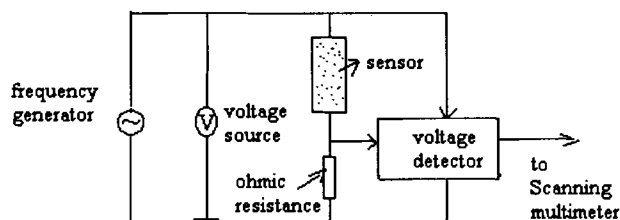

Figure 31: Block diagram of the set-up used for measurement of AC impedance.

Due to the sensing film's high impedance, the current ranges will be in the nanoampere to microampere range. While measuring electrical signals this small is relatively straightforward in the DC case, it becomes increasingly difficult as the frequency is increased. The voltage detector is a phase sensitive lock-in amplifer which should provide an accurate measurement of the AC singal. The commercial device from Solartron makes use of this kind of technique and the working frequency range of 1mHz to 10MHz is used in the present AC measurements.

3.2 Gas Delivery System

Figure 32 displays a diagram of the gas delivery system developed for the present work. The gas delivery system includes regulation of the flow rate for the

carrier gas (typically compressed air or inert gas), regulation of the humidity in the sample cell and regulation of the flow rate for the target gas.

This gas delivery system consists of one Hastings model 202D Mass Flow Controller (MFC1) with a flow rate of 0 - 3 standard liters per minute (SLPM), two Hastings model 202A MFCs (MFC2 and MFC3) with flow rates of 0 -100 standard centimeters per minute (SCCM) and 0 - 10 SCCM respectively, a control circuit for the three MFCs, a bubbler, a sample cell , ¼ inch Teflon and stainless steel tubing and various Swagelock fittings to connect the elements to the system.

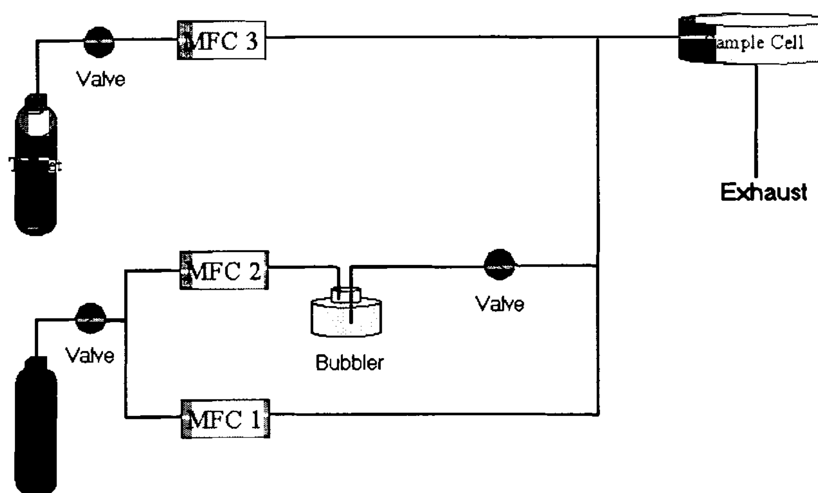

Figure 32: Gas delivery system

MFC1 regulates the flow of the carrier gas. The carrier gas used for present work is compressed dry air. MFC2 provides dry air for the bubbler that produces water vapor. MFC3 regulates the flow of the target gas. Each MFC has the same control circuit, which includes the circuit protection elements, more sensitive potentiometers for flow regulation and a digital display that reads the flow rate in SCCM.

The sample cell consists of a ½ inch Swagelock T and a Teflon receptor for the sensor. The Teflon receptor occupies one of the three openings in the T and the other two openings are connected to the gas delivery system. Figure 33 is a cross section of the sample cell.

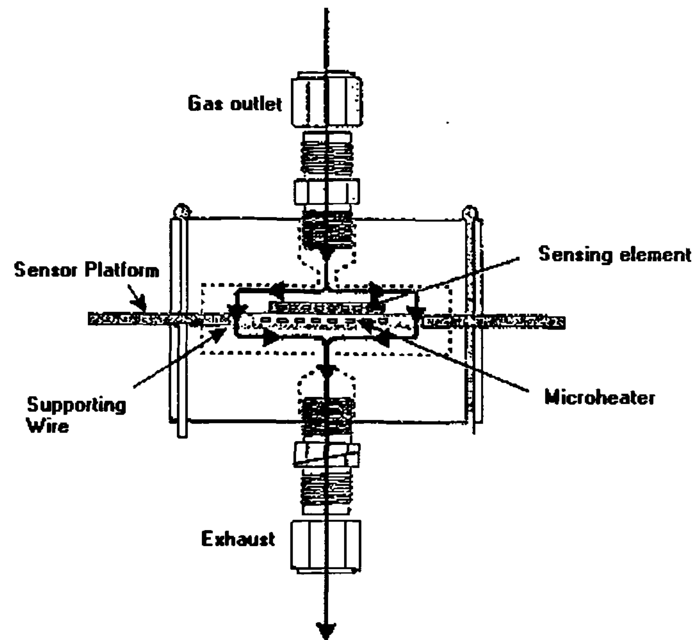

Figure 33: Schematic diagram of the sensor gas chamber

3.3 Data Acquisition System

The data acquisition system consists of a Keithley 2400 source meter, the data acquisition board, a computer and a temperature heater controller as shown in Figure 34.

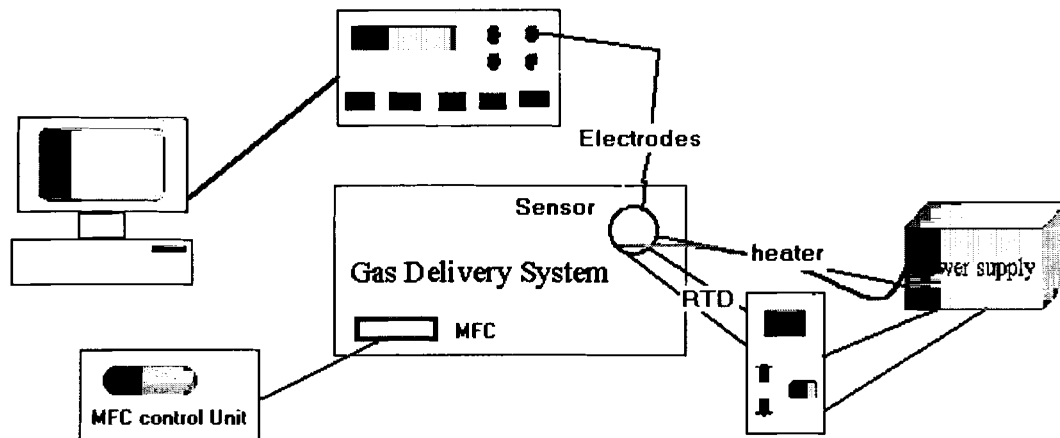

Figure 34: Diagram of data acquisition system

Since a significant interaction of a target gas with the semiconducting metal oxide film occurs over a narrow temperature range, it is also necessary to have a heating element capable of accurately achieving a desired temperature. Controlling the temperature of the sensor is facilitated by a Watlow series 980 model temperature controller and a Kepco model power supply. Setting up the temperature control circuit requires connecting the power supply and the platinum RTD via temperature controller and simultaneously connecting the power supply to the serpentine heater of the sensor. Finishing the setup requires running the Watlow controller Auto-tune program to set the proportional band integral derivative (PID) settings. These settings determine how the Watlow controls the power supply to achieve the desired temperature. Unfortunately, the RTD calibration curve of the sensor platform is different than the curve assumed by the Watlow temperature controller so one must

adjust the reading given by the Watlow controller accordingly. This requires converting the temperature reading of the Watlow to a resistance and using this resistance to determine the actual temperature from the correct RTD calibration curve.

Controlling the Source meter with a computer required installing a computer Boards GPIB(General Purpose Interface Bus) card. This GPIB card has an IEEE-488.2 bus, which is common to the testing meter. The language used for controlling the source meter is Labview graphical programming language, which can provide a friendly user interface.

4. EXPERIMENTAL RESULTS AND DISCUSSION

This chapter presents the experimental results of the current versus voltage characteristics of the undoped and gold doped WO_3 thin film sensor, appropriate discussion and comparison with theory. Initially, the structure and preparation of the WO_3 thin film sensor are presented. The experimental results presented include (a) the DC current versus voltage characteristics under different gas exposures of H_2S and ethylene at different temperatures, (b) the variation of the electrical resistance at different temperatures (c) the sensitivity versus voltage and gas concentration at different temperatures, and (d) the real and imaginary components of impedance as a function of frequency and voltage.

4.1 WO_3 Thin Film Sensor Structure and Preparation

The thin film WO_3 sensors were fabricated in the Laboratory of Surface Science and Technology (LASST) at the University of Maine and consisted of 500 Å WO_3 films deposited on r-cut sapphire substrates. The 3000 Å thick interdigital platinum electrodes were patterned by photolithography. The tungsten was RF sputtered in 50/50 Argon/Oxygen mixture while the gold doping was accomplished using a low temperature effusion cell technique (evaporative process).The rate for the gold-doping is 2 Å/minute and the thickness of the gold-layer is 15 Å. The interdigital platinum electrodes were deposited first onto the sapphire substrate and

the WO_3 film was deposited on the platinum electrodes as shown in Figure 27C. Figure 35 shows the sensor.

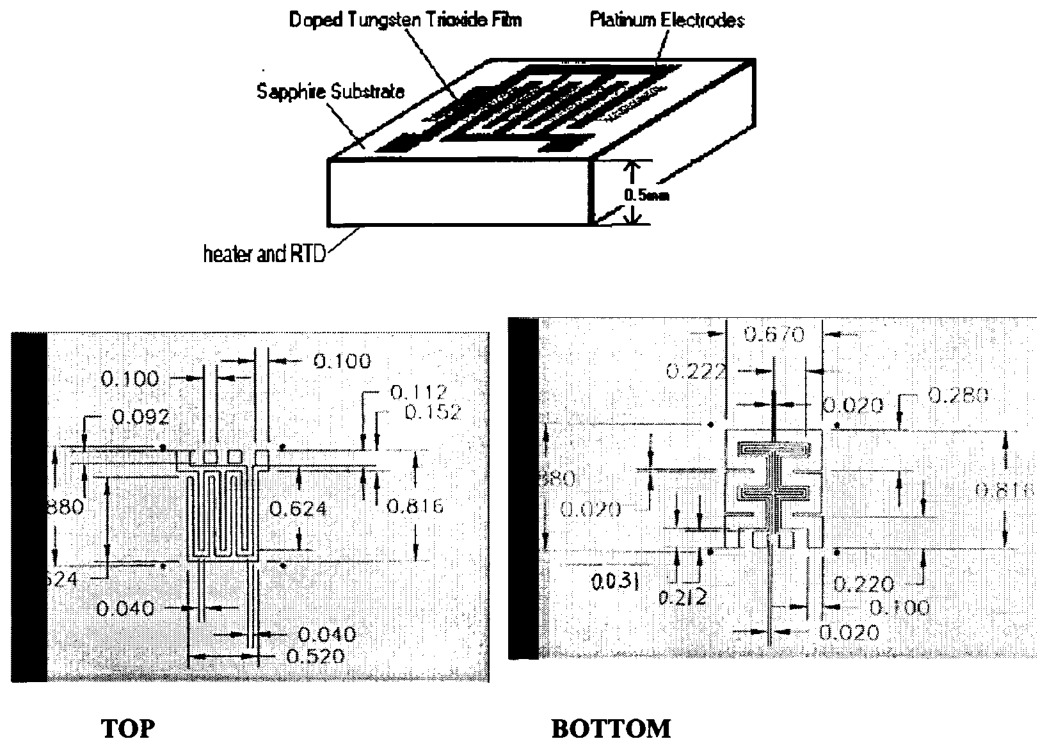

Figure 35: Top view of the WO_3 thin film sensor. TOP –MOS sensing element with IDT and sensing film. BOTTOM-MOS sensing element with heater and RTD. The dimensions are given in inches.

Referring to Figure 35, the backside of the sensor platform includes a serpentine heater made of a platinum resistance temperature device(RTD) for regulating the temperature of the film during testing. Between the platinum and the substrate there is a 200Å layer of zirconium which aids in adhering the platinum to the sapphire substrate[28]. Photolithography techniques are employed to make the platinum heater and RTD patterns. The deposition parameters for platinum and zirconium include a room temperature electron beam evaporation. The deposition

rates for platinum and zirconium were 2~4 Å/s and 2 Å/s respectively. Before depositing WO_3, the tungsten target was presputtered in argon for 5 minutes in order to get a pure tungsten target. The deposition parameters for WO_3 included a 500°C substrate temperature, 50% argon / 50% oxygen gas flow rate leading to a total pressure of 3 mTorr, and deposition rate 1 Å/s. In addition, the sample was rotated during the sputtering process in order to get an evenly sputtered film. After the deposition process, the sample was annealed in compessed air at 400°C in an oven for 24 hours.

4.2 Temperature Effect on Current Versus Voltage Characteristics in Compressed Air

The current versus voltage characteristics were measured for different samples at different temperatures in an environment of compressed air. The total gas flow rate through the sensor was maintained at 300 SCCM.

4.2.1 I/V characteristics of gold-doped WO_3 sensor as a function of temperature

Prior to performing the I/V measurements, the gold-doped WO_3 sensor was annealed in synthetic air at 400°C for more than 24 hours. The range of voltages used was –20V to 20V in steps of 10mV. The temperatures for the I/V measurements were room temperature (23°C), 100°C, 200°C, 300°C. Using the constant voltage source setup shown in Figure 30(a), the I/V characteristics were measured and are presented in Figure 36. The data is also presented in terms of the SMO film resistance

versus voltage in Figure 37 by obtaining V/I or R as a function of voltage from Figure 36.

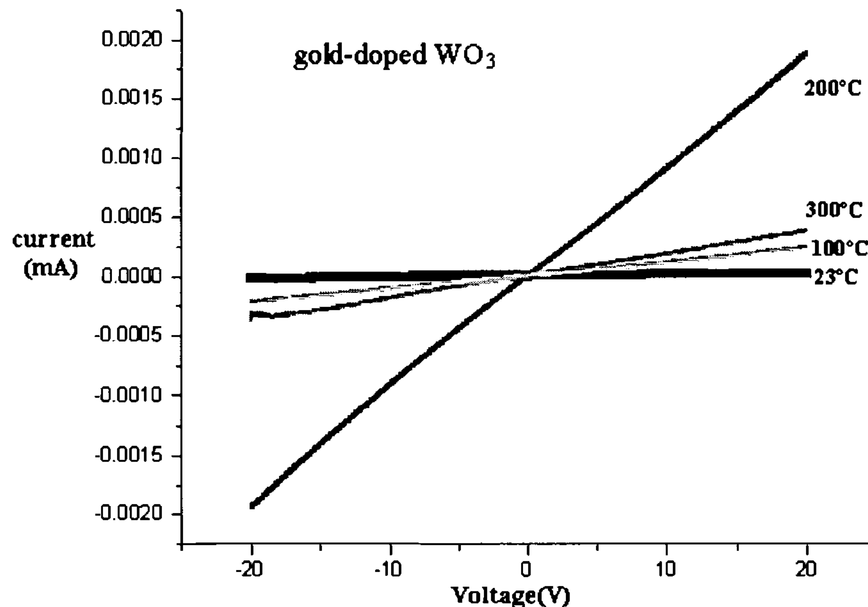

Figure 36: I/V characteristics of gold-doped WO_3 sensor as a function of temperature.

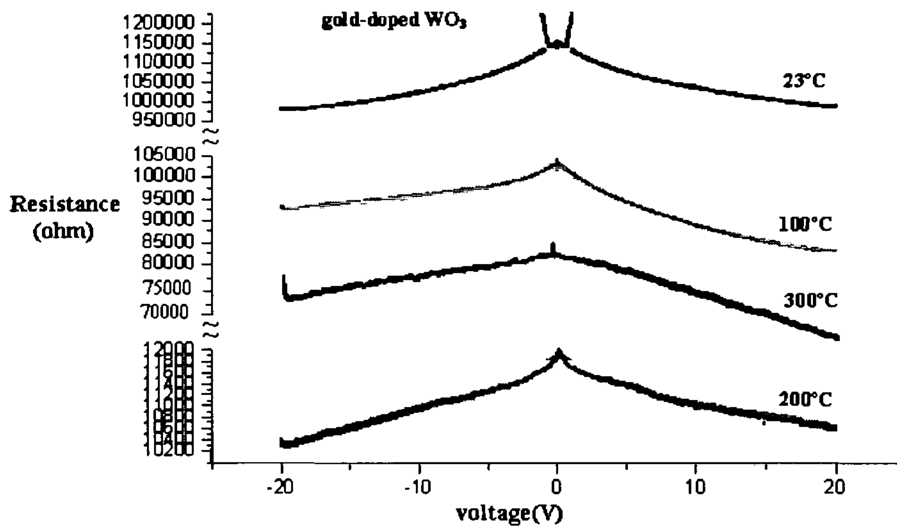

Figure 37: R/V characteristics of gold-doped WO_3 sensor as a function of temperature.

As mentioned before, the film resistance is a function of temperature. The current versus voltage relationship is a nonlinear curve. Although it is not apparent from the I/V curve, one can see more clearly the nonlinear behavior in the R/V curves. If the I/V curves in Figure 36 were perfectly linear, then the corresponding R versus V curve would be constant. Clearly this is not the case. The entire R/V curve is nonlinear with the most pronounced region occurring for low voltages (<5V).

4.2.2 I/V characteristics of an undoped WO_3 sensor as a function of temperature

The undoped WO_3 thin film sensor was deposited and annealed under the same conditions as the gold-doped sensor and the I/V and R/V characteristics were measured. Figure 38 and 39 displays the variation of the current and resistance as a function of voltage respectively for the undoped WO_3 sensor.

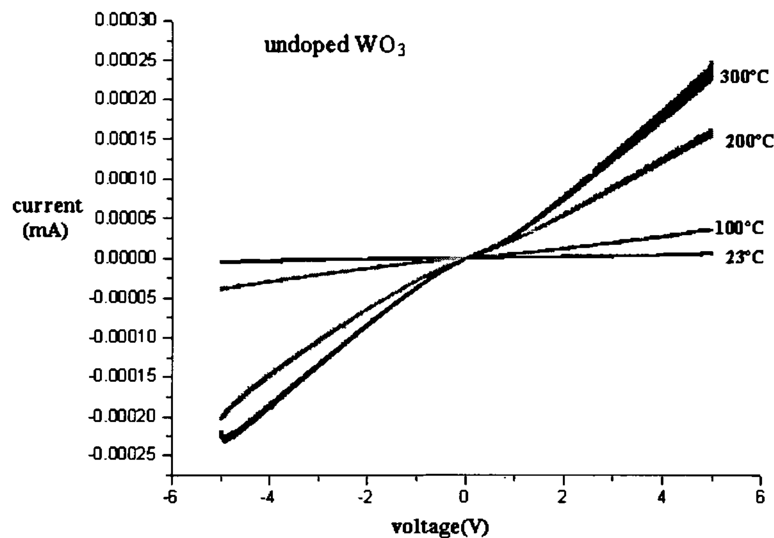

Figure 38 : I/V characteristics of an undoped WO_3 sensor as a function of Temperature.

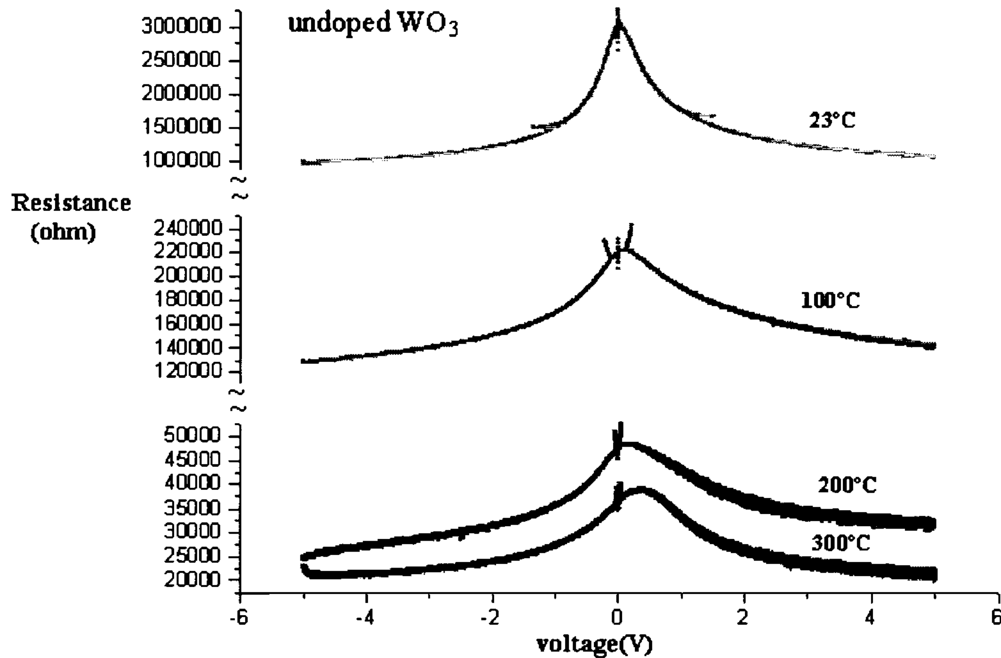

Figure 39: R/V characteristics of an undoped WO_3 sensor as a function of temperature.

As in the case of gold-doped WO_3 sensor, the I/V characteristic is also nonlinear particularly in the low voltage region. The nonlinear variation in the low voltage region of the R/V characteristics is more pronounced in the undoped film than in the gold-doped film.

4.3 Electrical Resistance of WO_3 Thin Film Sensor

From the I/V and R/V characteristics one can observe that the variation of current and resistance is a function of temperature, in order to examine this temperature dependence in detail, the variation of resistance versus temperature was examined. The electrical resistance measurements were performed using the two-point probe technique. Using the data obtained from Figure 37 and 39 one can observe that the resistance data get fuzzy and unstable when the voltage is very

small.This is mainly due to the limited resolution of the electrometer. The data which was taken in the range very close to zero voltage is not good and doesn't represent the real variation of the resistance. The constant voltage source chosen for the resistance versus temperature measurement is 2.5V since it is in the nonlinear region and away from the fuzzy region. The experimental environment was compressed air. The samples (both gold-doped films and undoped films) used for the resistance measurements are not the same as those used for the I/V measurements. Although the fabrication parameters and process are identical for all the samples the characteristics of samples may differ from batch to batch. All the sensors used for resistance measurement were annealed in compressed air at 400°C for more than 24 hours and then used to perform the resistance versus temperature measurements.

4.3.1 Resistance of a gold-doped WO_3 sensor as a function of temperature

The variation of resistance with temperature of a gold-doped WO_3 sensor is presented in Figures 40-43.The range for temperature is room temperature to 400°C. The temperature is changed every two hours. The first process is to increase the temperature from room temperature to 400°C in steps of 100°C and the following process is to decrease the temperature from 400°C to room temperature in steps of 100°C.

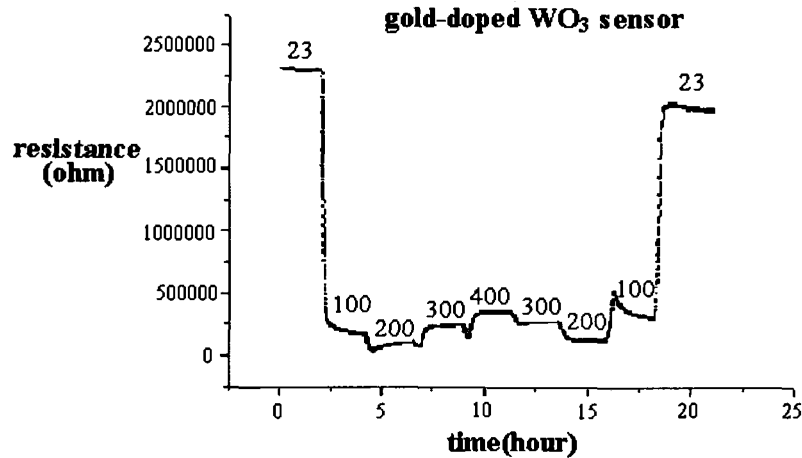

Figure 40: The resistance and temperature relationship of a gold-doped WO_3 sensor. X-axis is time, the temperature is changed in every two hours. The temperature is increased from room temperature to 400°C in steps of 100°C and then decreased form 400°C to room temperature in steps of 100°C. The voltage is 2.5Volts.

From Figure 40, one can clearly see that the resistance of gold-doped WO_3 sensor decreases until the temperature reaches around 200°C, and then the resistance increases with the temperature increasing from 200°C to 400°C. For the decreasing temperature process, the resistance first decreases until 200°C and then increases again with the temperature decreases from 200°C to room temperature. Figure 41 shows more detailed information in the 200°C to 400°C range. The whole curve is divided into two parts. The first part is to increase the temperature from 200°C to 400°C in steps of 50°C and the second part is to decrease the temperature from 400°C to 200°C in steps of 50°C. The temperature is changed every two hours.

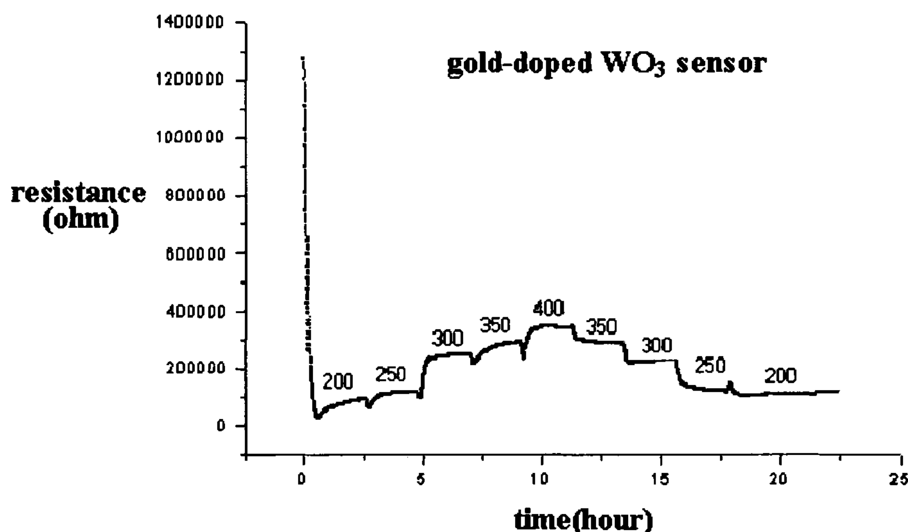

Figure 41: The variation of a gold-doped WO_3 sensor's resistance as a function of temperature. The range of temperature was from 200°C to 400°C. The temperature was increased from room temperature to 200°C, and then from 200°C increased to 400°C in steps of 50°C. After the increasing process the temperature was decreased from 400°C to 200°C in steps of 50°C. The temperature is changed every two hours. The voltage is 2.5Volts.

Let's examine the hysteresis of gold-doped WO_3 sensor resistance as a function of temperature. Figure 42(a) shows the change of resistances in the temperature range of 200°C to 400°C. The temperature starts from 200°C and increases to 400°C in steps of 50°C and then decreases to 200°C in steps of 50°C and this process was repeated for three times. After this examination, the temperatures were performed over a wider range using the same sample. Figure 42(b) shows the change of resistances in the temperature range of room temperature to

400°C in steps of 100°C and then decreases from 400°C to room temperature in steps of 100°C. This process was repeated five times.

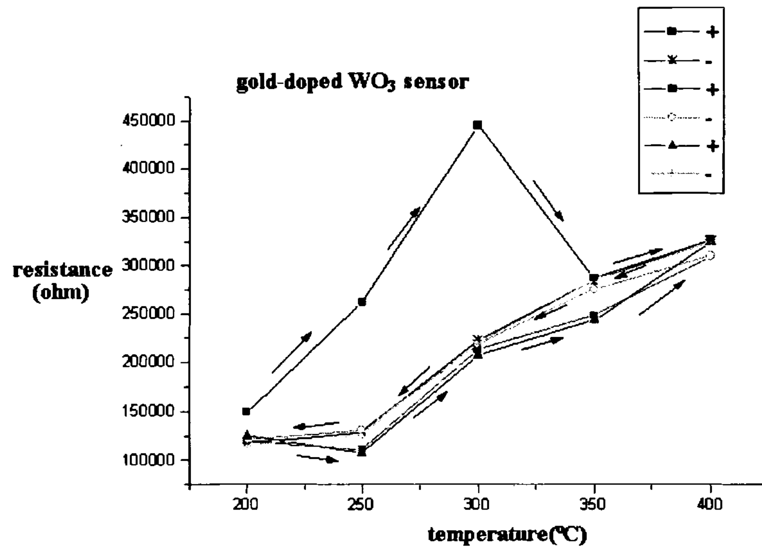

(a)

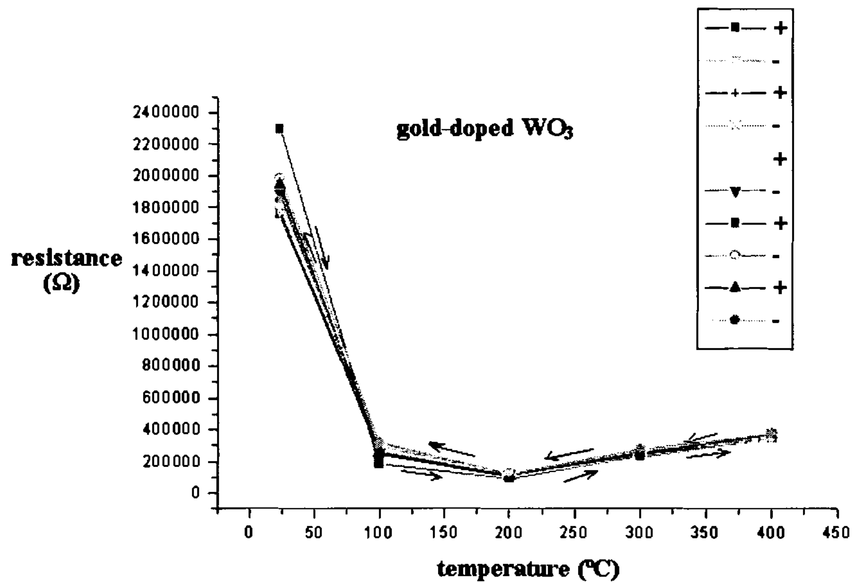

(b)

Figure 42 : The hysteresis of the variation of a gold-doped WO_3 sensor's resistance as a function of temperature.(a)temperatures from 200°C to 400°C.(b) temperatures

from 23°C to 400 °C. The direction of the arrow is the trace of temperature. '+' means the temperature increases,' – 'means the temperature decreases.

From Figure 42(a), one can observe some hysteresis. The major issue here is that when one increases the temperature from 200°C to 400°C the first time, one observes hysteresis due possibly to species' adsorption and desorption processes on the surface or some other processes. When one increase and decrease temperature several times, the increasing curve and decreasing curve tend to be the very close and this can be see very clearly from Figure 42(b).

4.3.2 Resistance of an undoped WO_3 sensor as a function of temperature

As in the case of samples for resistance measurement of the gold-doped sensor, the undoped sensor used for the resistance measurement is from a different batch as that was used for the I/V measurements. The constant voltage source is 2.5V. The variation of resistance with temperature of an undoped WO_3 sensor is presented in Figure 43 and 44. The range of temperature is room temperature to 400°C.The temperature is changed every two hours.

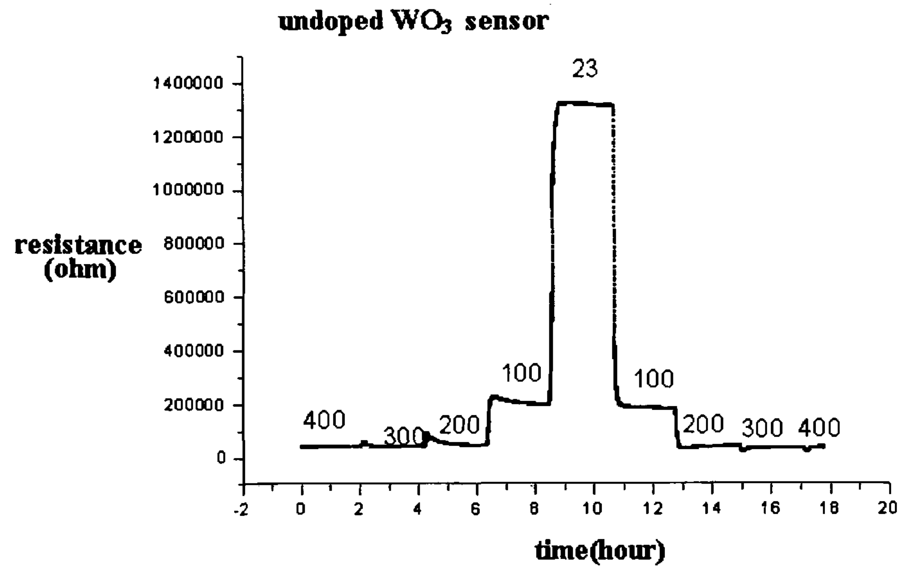

Figure 43: The variation of an undoped WO_3 sensor's resistance with temperature. X-axis is time and the temperature is changed every two hours. The temperature is decreased from 400°C to room temperature in steps of 100°C and then increased room temperature to 400°C in steps of 100°C. The voltage is 2.5Volts.

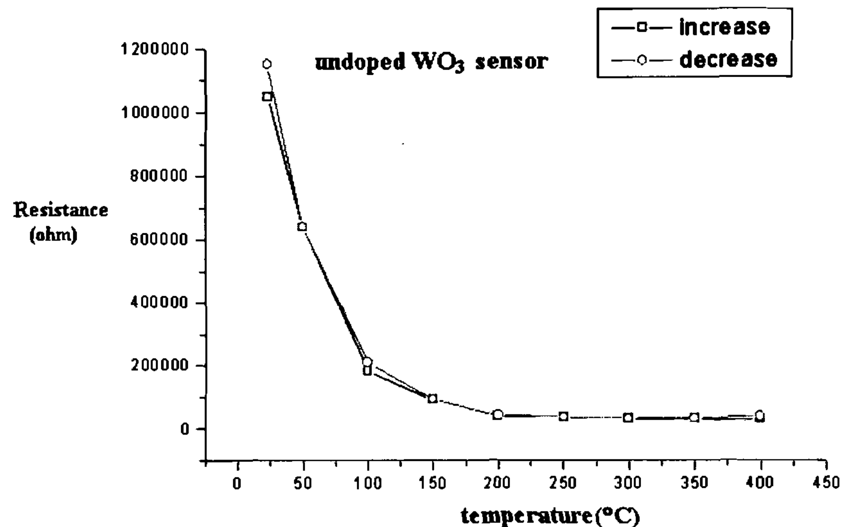

Figure 44: The variation of an undoped WO_3 sensor's resistance with temperature. The range of temperatures used is from 23°C to 400°C in steps of 50°C.

The data in Figure 43 and 44 were taken after several " heat up" and "cool down" cycles in order to eliminate possible species' adsorption and desorption processes. In the undoped WO_3 sensor there is minimal hysteresis.

4.4 H_2S Gas Effect

The I/V and R/V characteristics when the sensor is exposed to a certain target gas was also examined. H_2S gas is one of the target gases used. The experiments were done both on gold-doped WO_3 sensors and undoped WO_3 sensors. Since these samples are from different batches as those used to do the previous measurements the baseline resistance may be slightly different. After the deposition process, these samples were annealed in compressed air for 24 hours at 400°C. The target gas concentration used for the I/V measurement is 30 PPM, no humidity and the total gas flow rate is 300 SCCM.

4.4.1 The resistance of gold-doped WO_3 sensor as a function of voltage under H_2S gas exposure

For the I/V measurement in H_2S gas exposure, the range of voltages used was –20V to 20V in steps of 10mV which is the same as the I/V measurement in compressed air. The temperature for the I/V measurements were 23°C, 100°C, 200°C and 300 °C. Figures 45 and 46 present the I/V characteristics and the corresponding resistance versus voltage relationship in compressed air and 30PPM H_2S gas exposure respectively.

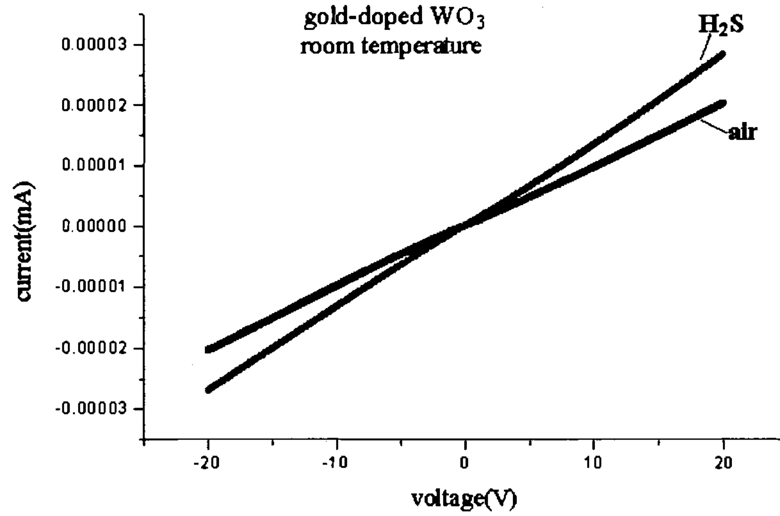

(a)

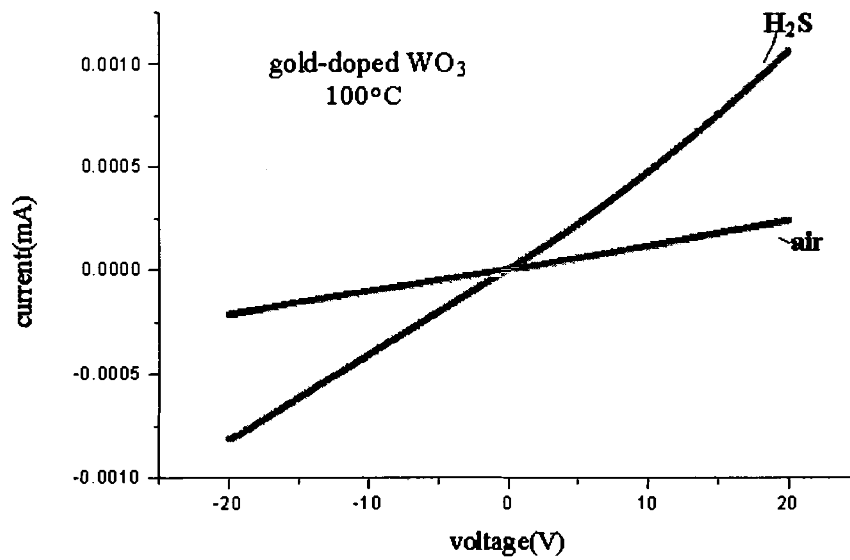

(b)

Figure 45: I/V characteristics of a gold-doped WO_3 sensor under compressed air and H_2S gas exposure. The H_2S gas concentration is 30 PPM. The heater temperature is (a) 23°C, (b)100°C, (c) 200°C and (d) 300°C.

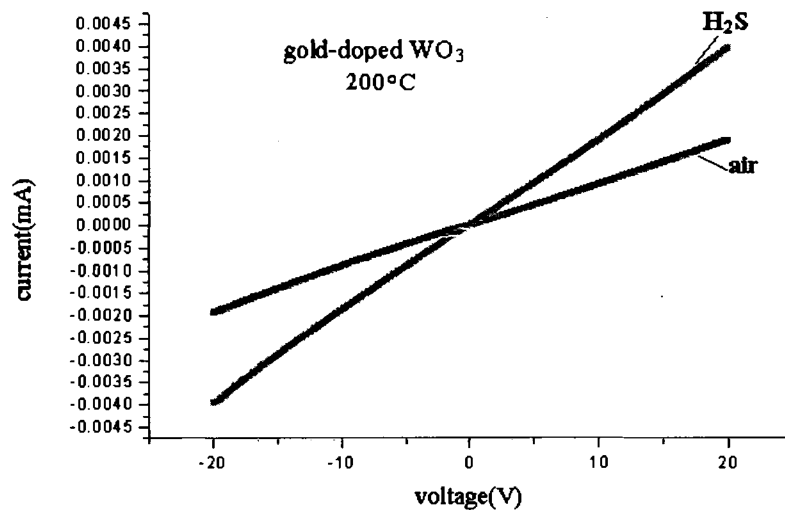

(c)

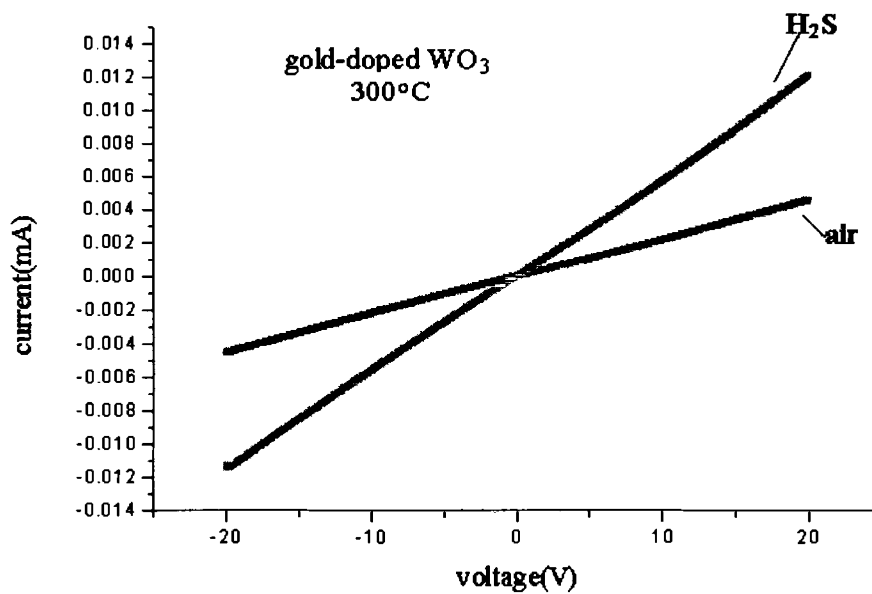

(d)

Figure 45 continues.

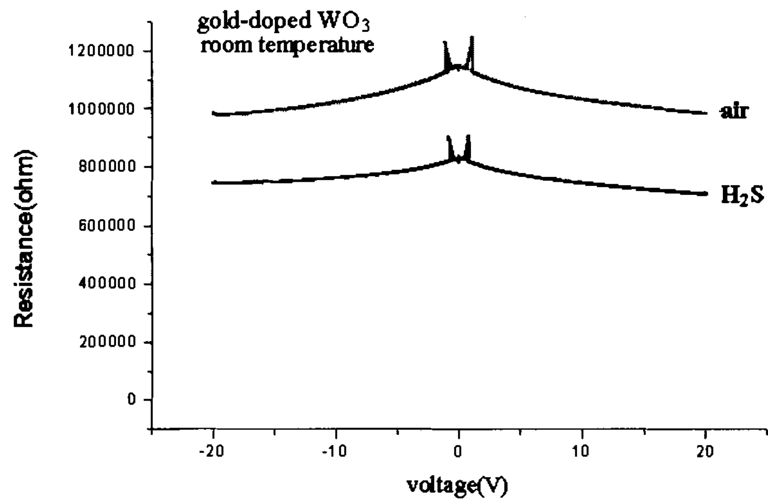

(a)

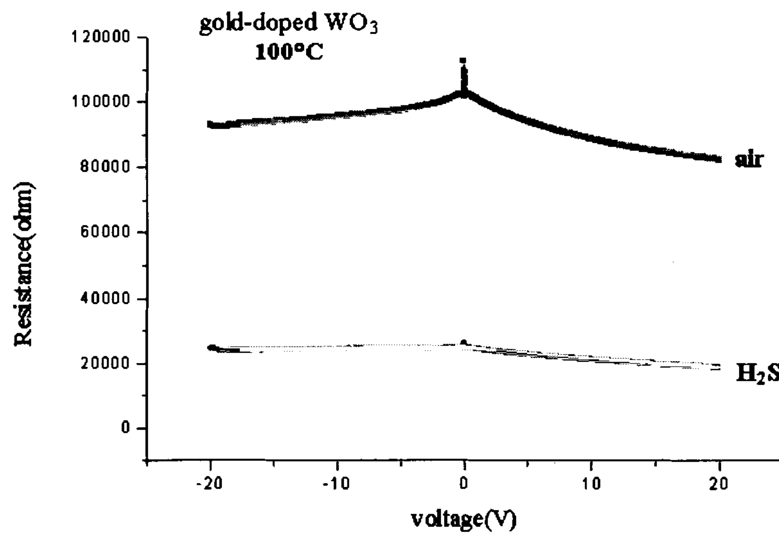

(b)

Figure 46 : R/V characteristics of a gold-doped WO_3 sensor under compressed air and H_2S gas exposure. The H_2S gas concentration is 30 PPM. The heater temperature is (a) 23°C, (b) 100°C, (c) 200°C and (d) 300°C.

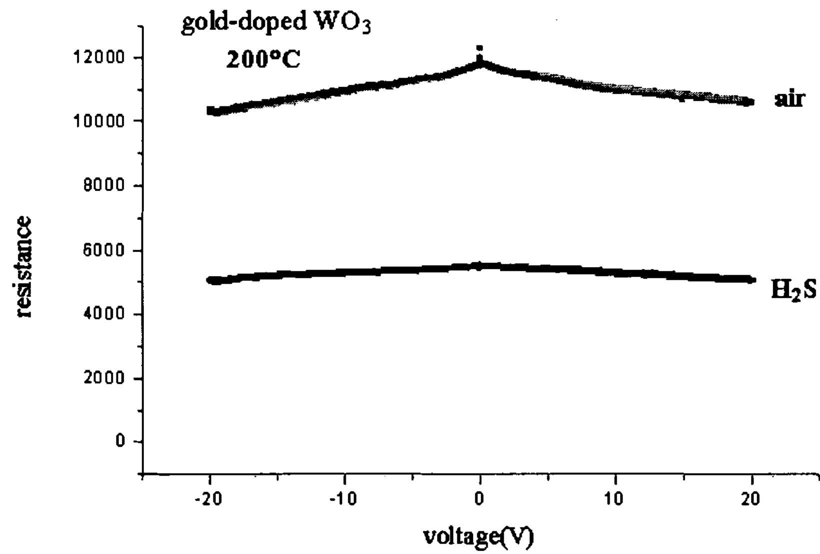

(c)

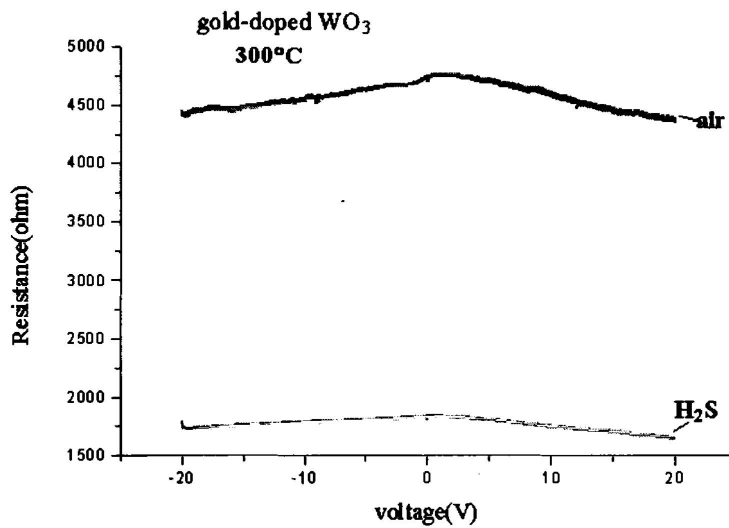

(d)

Figure 46 continues.

From Figures 45 and 46, one can clearly see that the resistance of gold-doped sensor measured under H_2S gas exposure is smaller than the resistance measured in

the compressed air. When the temperature increases, the resistance difference in H_2S gas exposure and compressed air also increases.

The hysterisis of I/V characteristics of gold-doped sensor under H_2S gas exposure and compressed air at 250°C was also examined. The voltage range is from –20V to 20V. The measurement was first made in compressed air. The second step was in H_2S gas exposure. The third step was in compressed air again. The fourth step was in H_2S gas exposure. Figure 47 presents the I/V characteristics and the corresponding R/V characteristics.

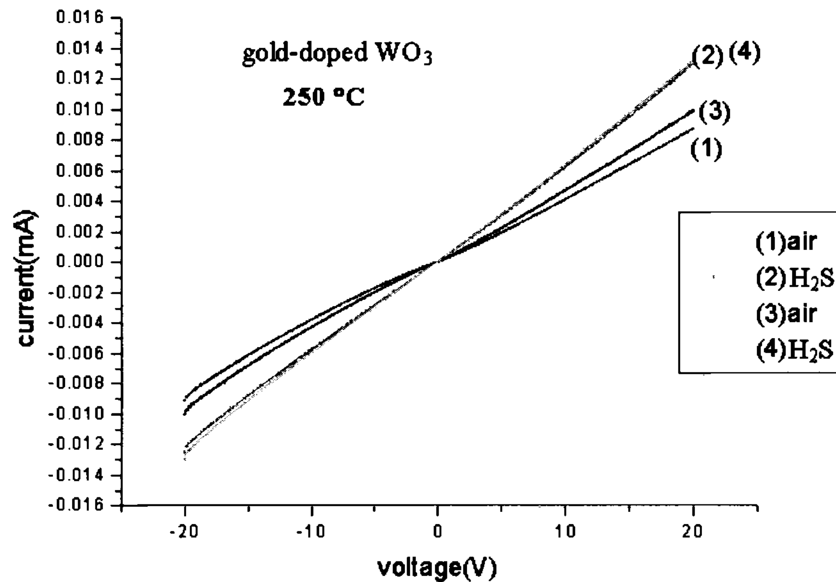

(a)

Figure 47: The hysteresis behavior of I/V characteristics and the variation of resistance as a function of voltage under H_2S and compressed air. The sensor is a gold doped WO_3 sensor. The environment temperature is 250 °C. The curve (1) and (3) were taken in compressed air and curve (2) and(4) were taken in H_2S gas exposure.

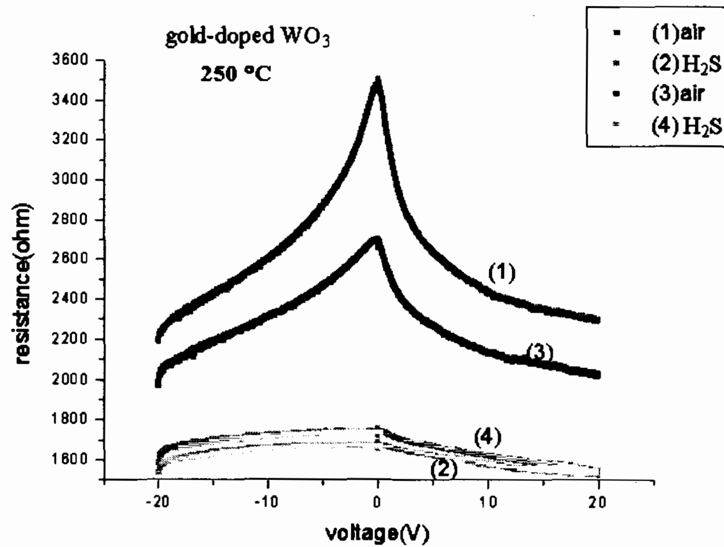

(b)

Figure 47 continues.

4.4.2 WO_3 sensor's resistance as a function of voltage under H_2S gas exposure for the undoped WO_3 sensor

The measurement procedure used to examine the I/V characteristics of the undoped WO_3 sensor was the same as the gold-doped sensor. The undoped sensor used for I/V measurement in synthetic air are from different batches. Figures 48 and 49 present the I/V characteristics and the corresponding resistance versus voltage relationship in compressed air and H_2S gas exposures respectively.

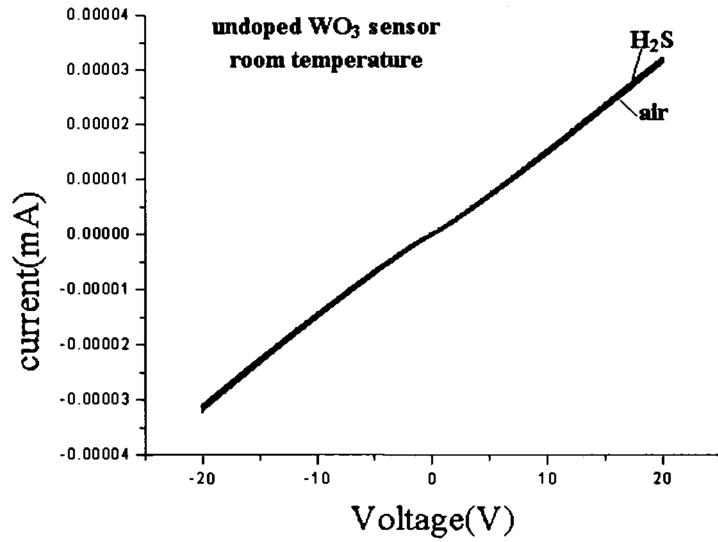

(a)

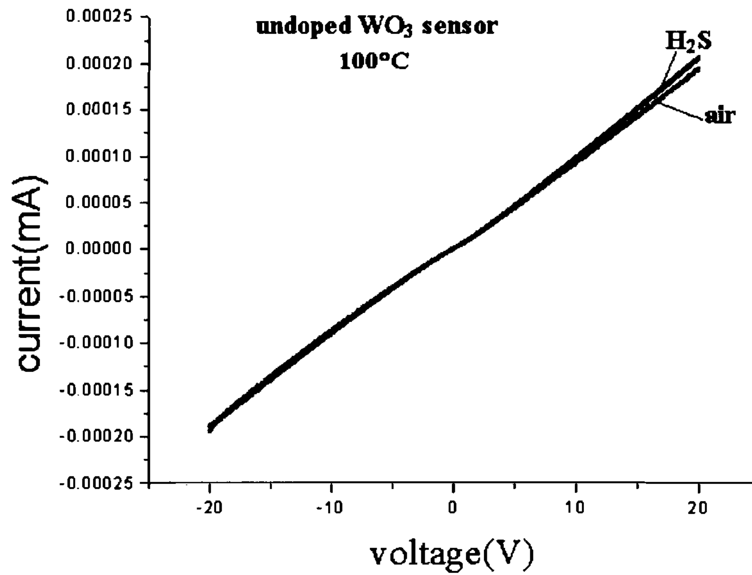

(b)

Figure 48: I/V characteristics of an undoped WO_3 sensor under compressed air and H_2S gas exposure. The H_2S gas concentration is 30 PPM. The heater temperature is (a) 23°C, (b)100°C, (c) 200°C and (d) 300°C.

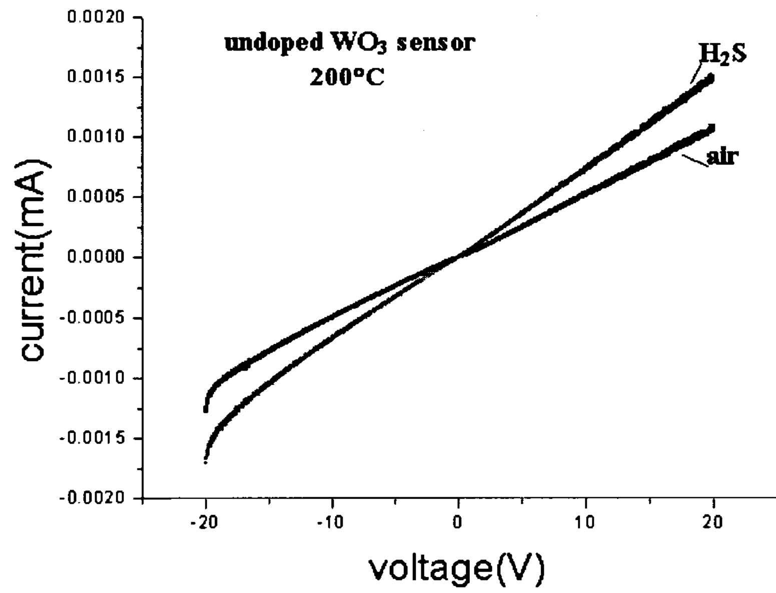

(c)

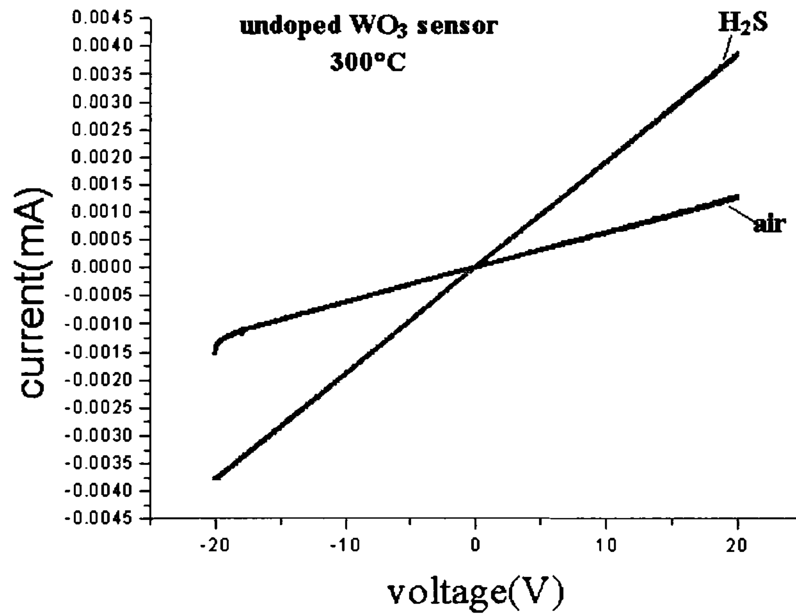

(d)

Figure 48 continues.

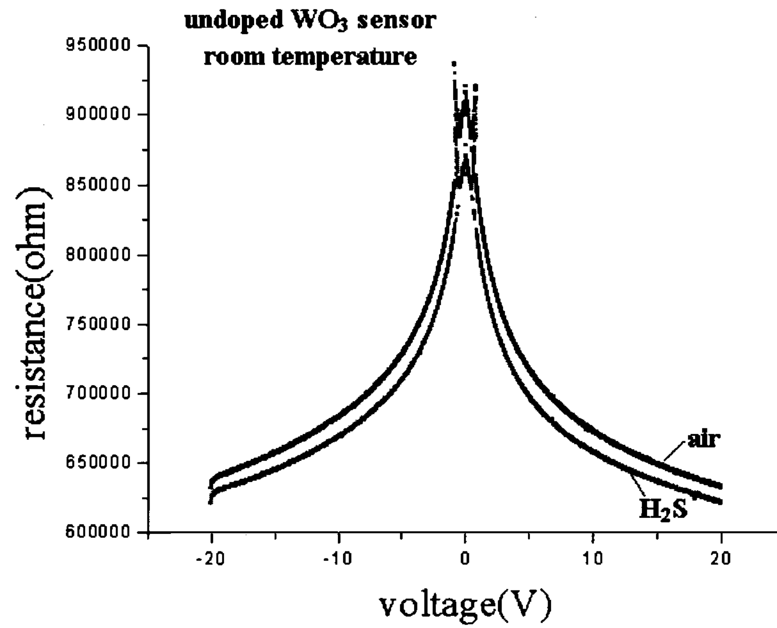

(a)

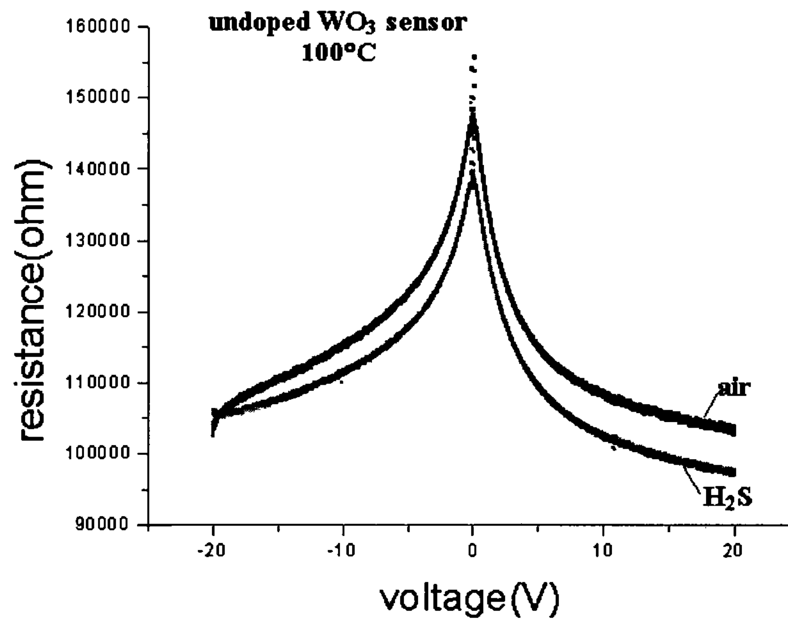

(b)

Figure 49 : The variation of an undoped WO_3 sensor's resistance with voltage under compressed air and H_2S exposure. The gas concentration is 30ppm. The heater temperature is (a) 23°C, (b) 100°C, (c) 200°C and (d) 300°C.

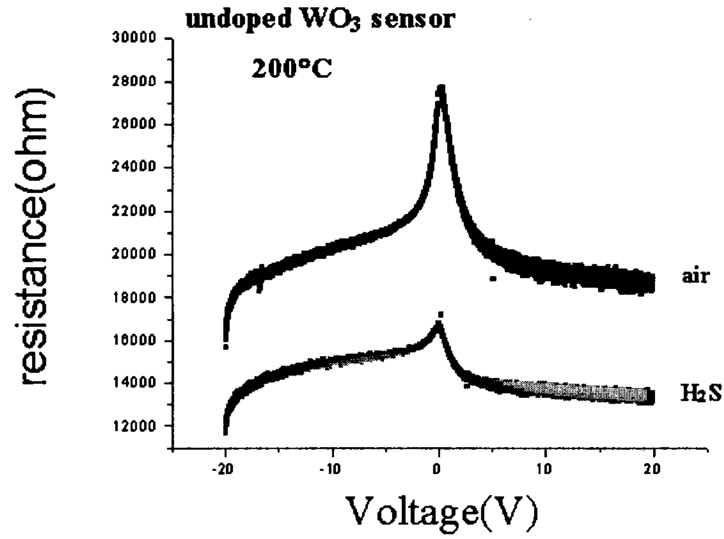

(c)

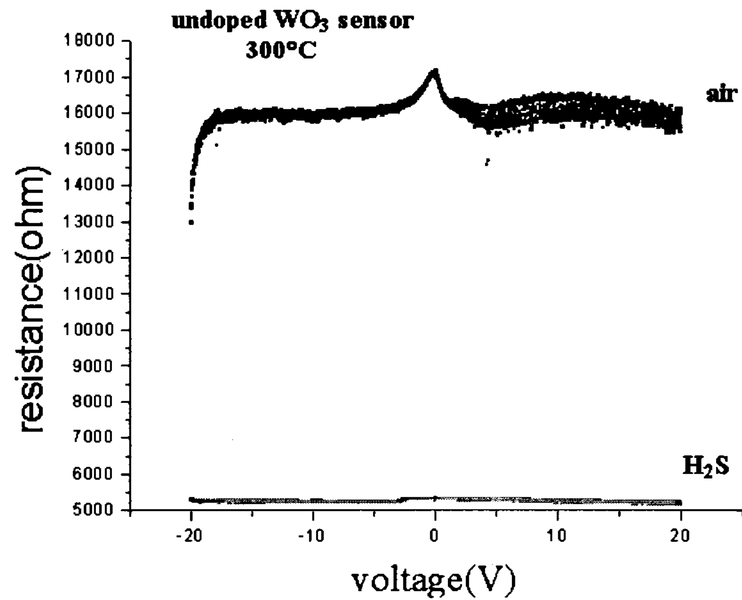

(d)

Figure 49 continues.

As mentioned before, the slope of the I/V curve is the inverse of the device resistance. Since H_2S is a reducing gas, it will cause the device resistance to decrease. From Figures 48 and 49, one can clearly see that the resistance measured under H_2S gas exposure is smaller than the resistance measured in compressed air.

When the temperature increases, the difference in resistance measured in the two different media also increases.

Let's examine the hysterisis of I/V characteristics under H_2S gas exposure and compressed air at a temperature of 250°C. The voltage starts from –20V to 20V. The measurement was first made in the compressed air and the second was in an H_2S gas exposure. The third step was in compressed air again . The fourth step was in H_2S gas exposure. Figure 50 presents the I/V characteristics and the corresponding R/V characteristics.

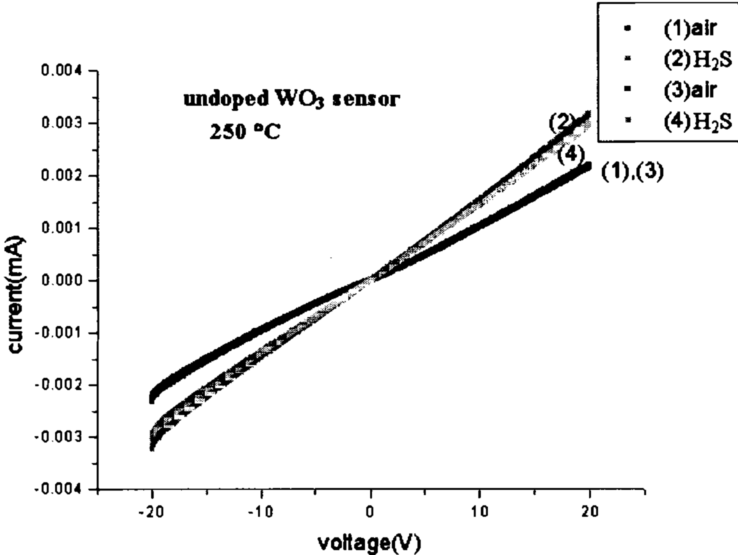

(a)

Figure 50: The hysterisis behavior of I/V characteristics and the variation of resistance as a function of voltage under H_2S and compressed air. The sensor is an undoped WO_3 sensor. The environment temperature is 250 °C. The curve (1) and (3) were taken in compressed air and curve(2) and(4) were taken in H_2S gas exposure.

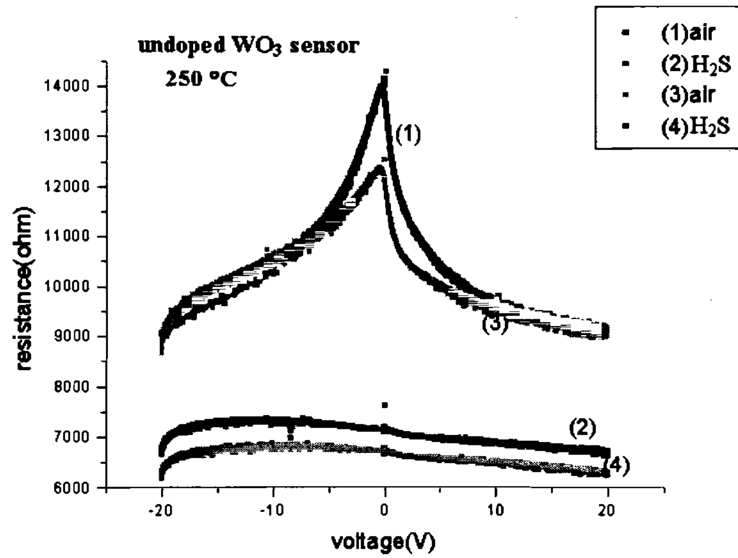

(b)

Figure 50 continues.

From the above figures, one can observe some hysteresis for the I/V characteristics taken in different gas exposures. Compared to the gold-doped sensor, the hysteresis behavior is much smaller for the undoped sensor.

4.5 Sensitivity vs. Voltage

The sensitivity, S, of a sensor is an extremely critical feature of the sensor properties when one is working with precise control systems or the sensing of potentially dangerous measurands. Mathematically, it may be defined by the following relation,

$$S = \left| \frac{X_r - X_A}{X_A} \right|,$$

(47)

where

X_r = the sensor response when the measurand is present

and

X_A = the ambient sensor response in the absensce of the measurand.

Now if one examines the sensor's response using the sensor's resistance, then

$$\Delta R = X_r - X_A,$$

where $X_r \Rightarrow R_r$ (sensor resistance measured when sensor exposed to H_2S gas) ,

$X_A \Rightarrow R_A$ (sensor resistance measured in compressed air).

Then the sensitivity of the sensor can be expressed as

$$S = \frac{\Delta R}{R_A}$$

Figures 51 and 52 show the variation of gold doped and undoped WO_3 sensor's sensitivity as a function of voltage respectively. The measurand is 30 PPM H_2S and the range of voltages used is –20V to 20V in steps of 10mV. The temperatures are room temperature (23°C), 100°C, 200°C and 300°C.

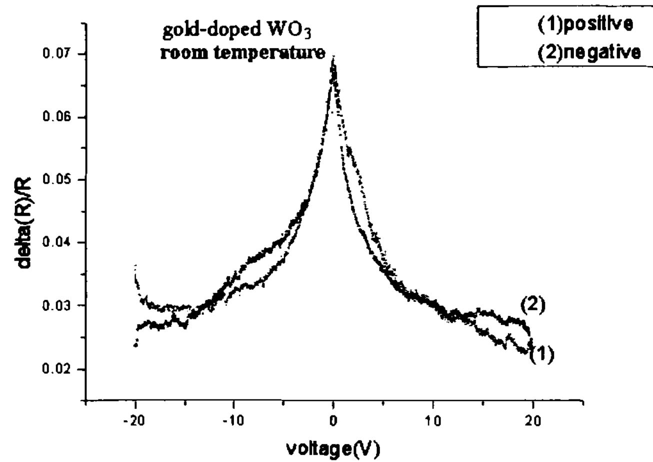

(a)

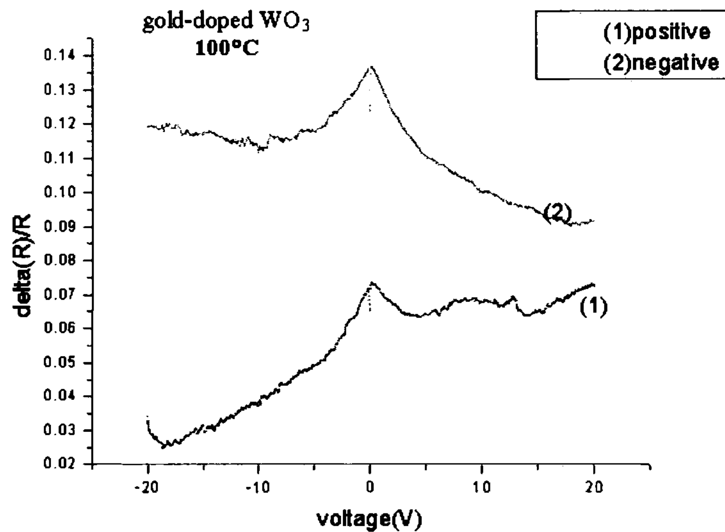

(b)

Figure 51: (a) The variation of sensitivity as a function a voltage, the sensor is gold-doped WO_3. (1) positive means the voltage starts from -20V and increases to 20V. (2) negative means the voltage starts from 20V and goes the other way to –20V. (a), (b), (c) and (d) curve represents the sensitivity at room 23°C, 100°C, 200°C and 300°C respectively.

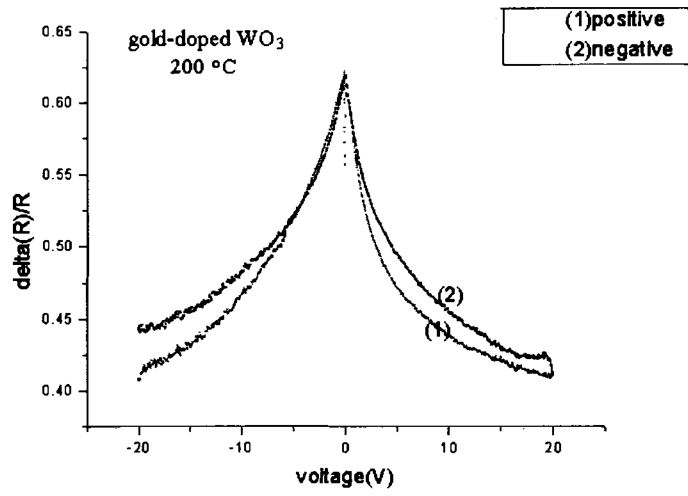

(c)

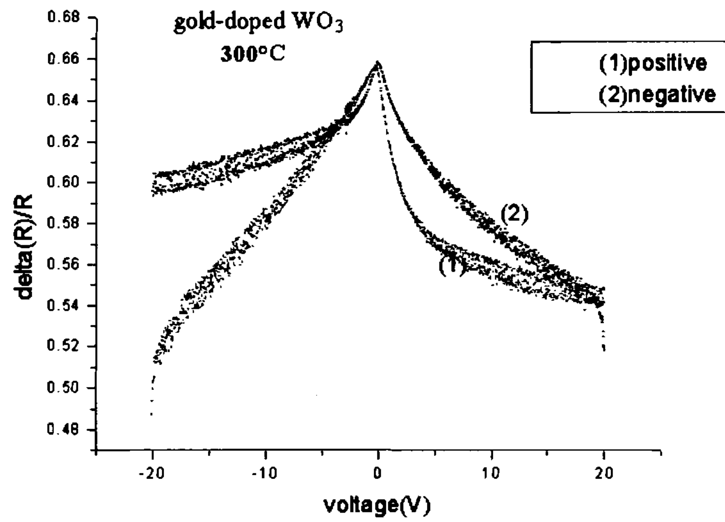

(d)

Figure 51 Continues .

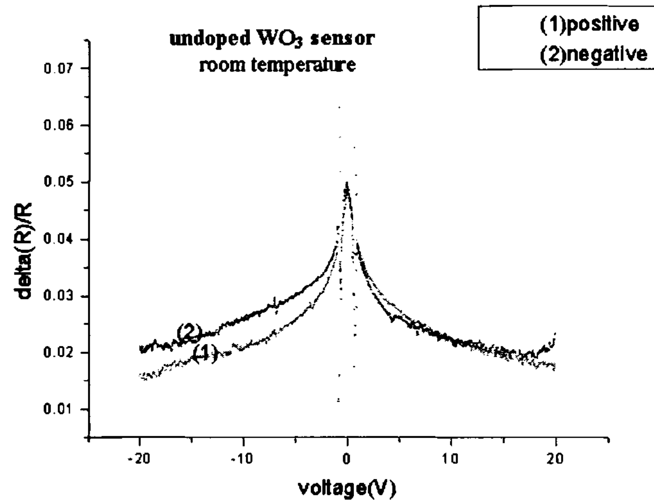

(a)

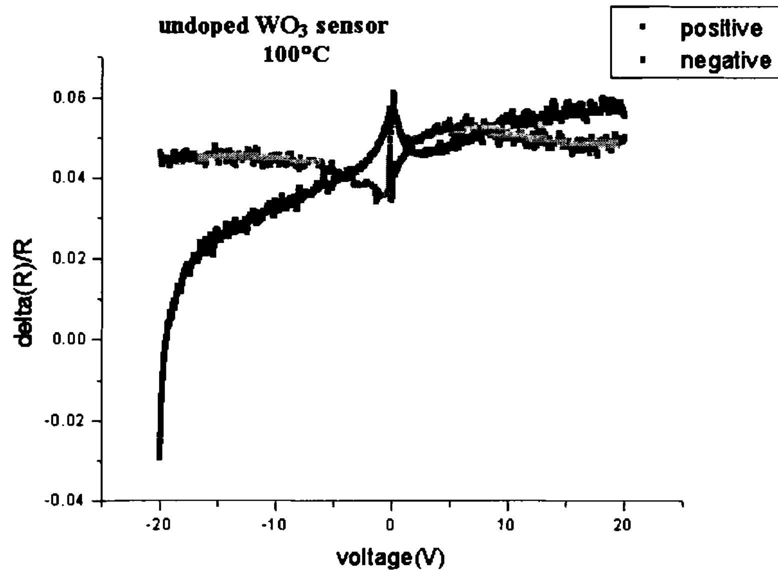

(b)

Figure 52: The variation of sensitivity as a function of voltage, the sensor is undoped WO_3. (1) positive means the voltage starts from -20V and increases to 20V. (2) negative means the voltage starts from 20V and goes the other way to –20V. (a), (b), (c) and (d) curve represents the sensitivity at room 23°C, 100°C, 200°C and 300°C respectively.

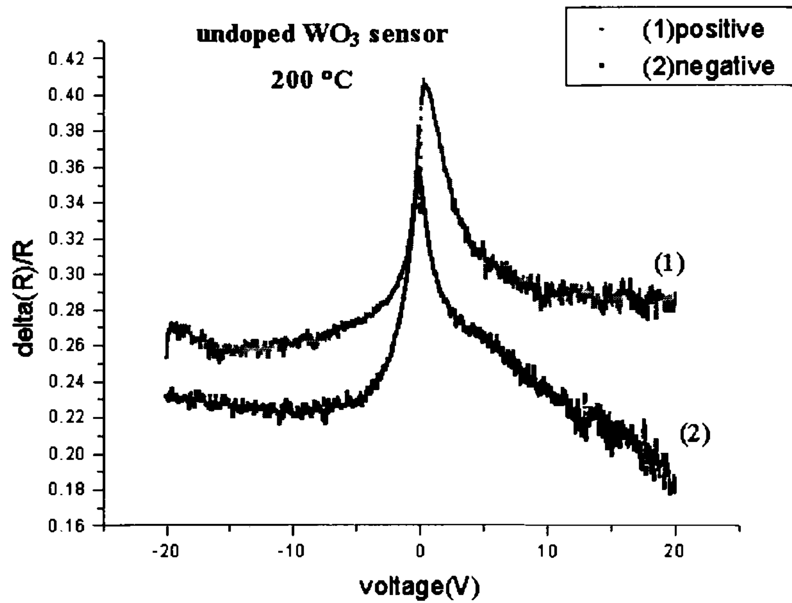

(c)

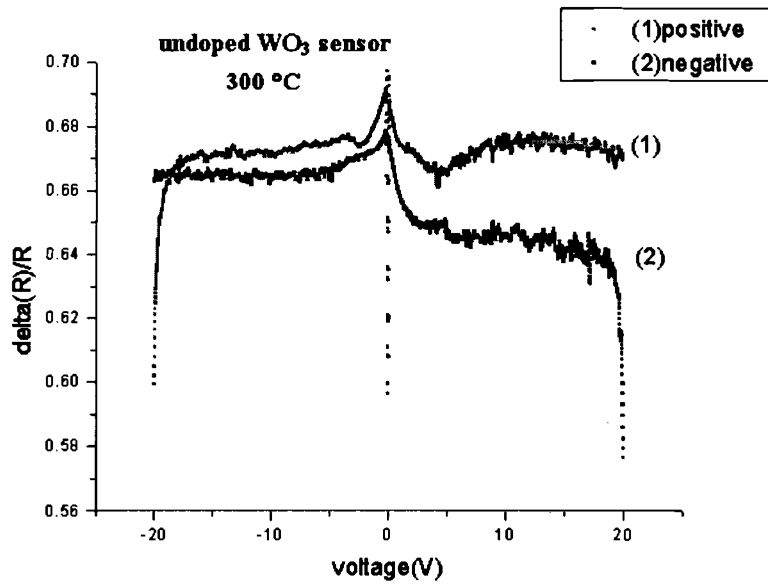

(d)

Figure 52 continues.

It is interesting to point out that the sensitivity of the gold-doped WO_3 sensor is almost double the value of the undoped WO_3 sensor even though the data was

taken under the same experimental environment. Figure 53 shows information about the hysterisis for undoped and gold-doped WO_3 sensors respectively.

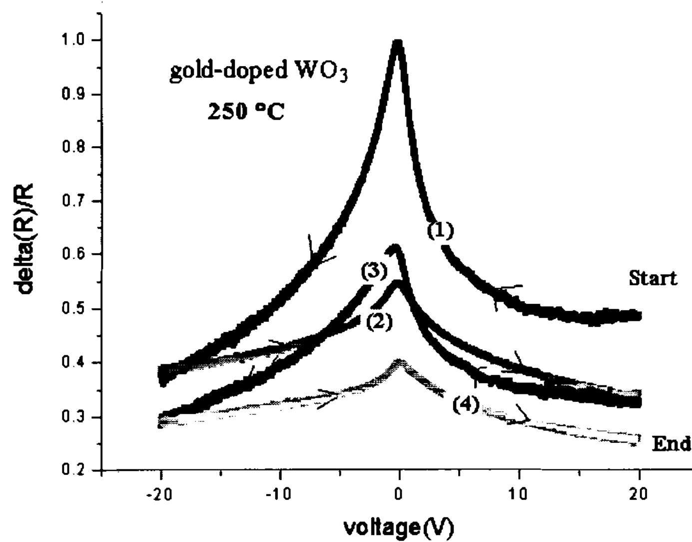

(a)

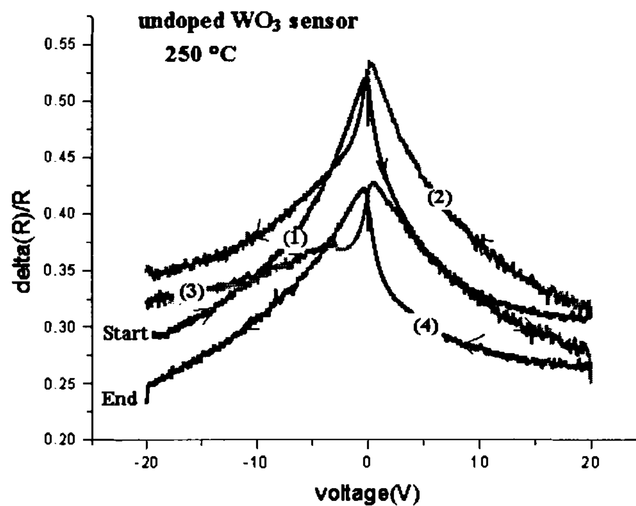

(b)

Figure 53: The hysterisis behavior of sensitivity as a function of voltage. The film is undoped WO_3 film. The environment temperature is 250 °C. The arrow direction is the trace of the voltage. (1),(2),(3) and (4) are the order of the measurement.

One can observe the hysteresis behavior on both gold-doped and undoped sensor. From Figure 53, one can also observe these curve are not perfectly symmetric and there is a voltage polarity effect.

4.6 Ethylene Effect

Ethylene is also a reducing gas which is emitted when the fruit is in the ripening process. Using the WO_3 thin film sensor to detect ethylene is another application in the Laboratory of Surface Science and Technology, which is supported by Department of Agriculture. The I/V characteristics of a gold-doped WO_3 sensor is measured and presented in Figure 54 when exposed to an ethylene concentration of 5PPM at 400°C. Figure 55 shows the corresponding variation of resistance as a function of voltage. The sensitivity as a function of different temperature is examined and presented in Figure 56, which include temperatures at 300°C, 350°C, 375°C, 400°C, 425°C, 450°C, 500°C. The voltage range is from –20V to 20V in steps of 10mV. The sensor has the same fabrication parameters as those used to do the I/V measurement in air and H_2S, but one needs to keep in mind that it is also from the different batches from those used before.

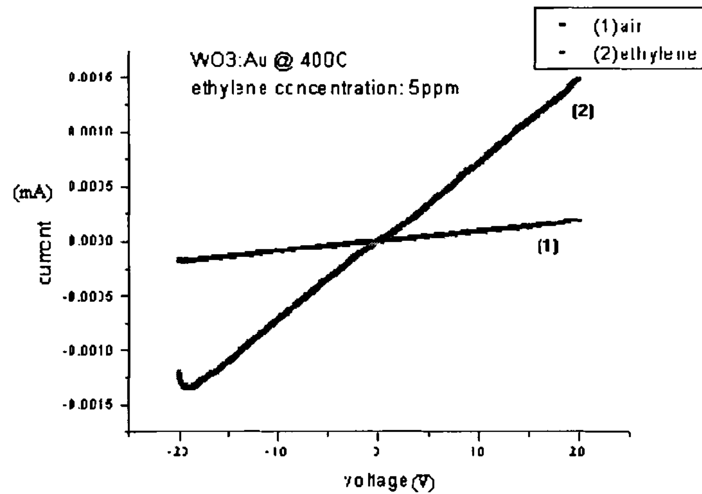

Figure 54: I/V characteristics of gold –doped WO_3 sensor, (1) taken under the synthetic air, (2) taken under the ethylene exposure and the concentration is 5 parts per million. The examining temperature is 400 °C.

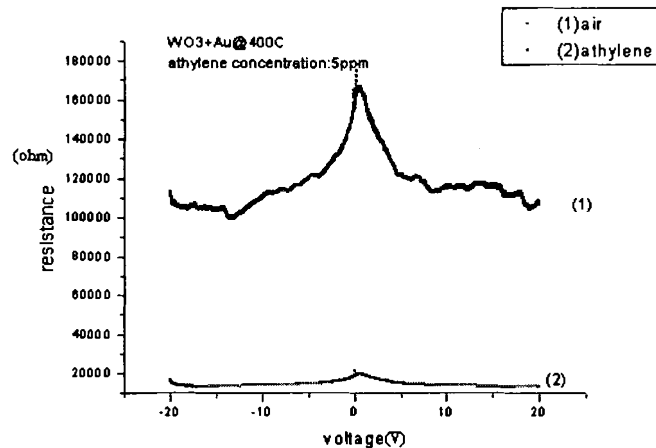

Figure 55: R/V characteristics of gold-doped WO_3 sensor, (1) taken under the compressed air, (2) taken under the ethylene exposure and the concentration is 5 parts per million. The temperature is 400 °C.

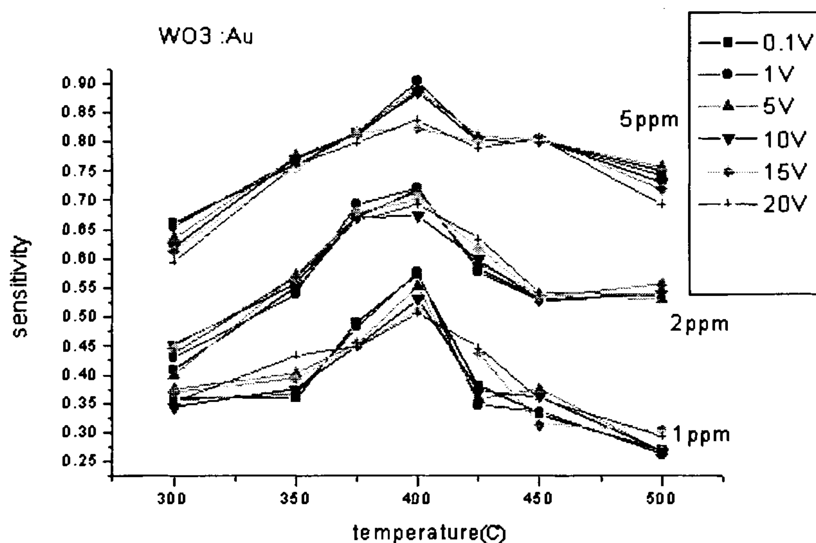

Figure 56: Variation of the sensitivity of gold-doped WO_3 as a function of temperature, voltage and ethylene concentration.

4.7 AC Measurement

The previous I/V experiments were done in the DC case. If an AC voltage was applied one would have two parameters including frequency and voltage amplitude to adjust which is double the parameters(voltage amplitude) in the DC case. Potentially the AC results should allow one to more accurately to determine critical sensing parameters such as selectivity. The frequency range used for the present work is from 0 to 10Mhz. The voltages used are 0.5V, 1V, 2V and 3V. The undoped WO_3 thin film sensor for the AC measurement used the same formula as those for the DC measurements but it came from different batches. After the deposition process, the film was annealed at 400°C in an oven for 24 hours just as those used for DC measurements. Figures 57 and 58 show the real and imaginary parts of the impedance as a function of frequency respectively. The experiment was done in the compressed air at 350°C.

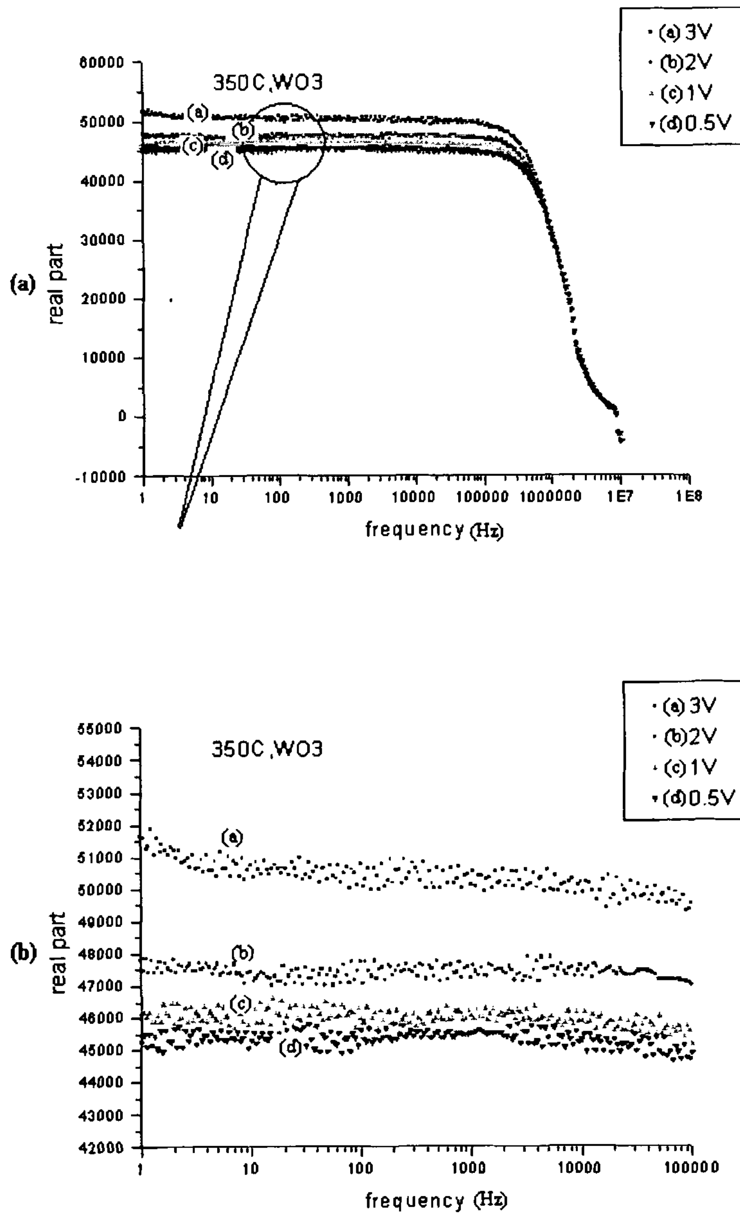

Figure 57: The real part of the impedance of undoped WO_3 sensor as a function of frequency at different voltages. The temperature is 350°C.(a) full scale (b) zoomed part.

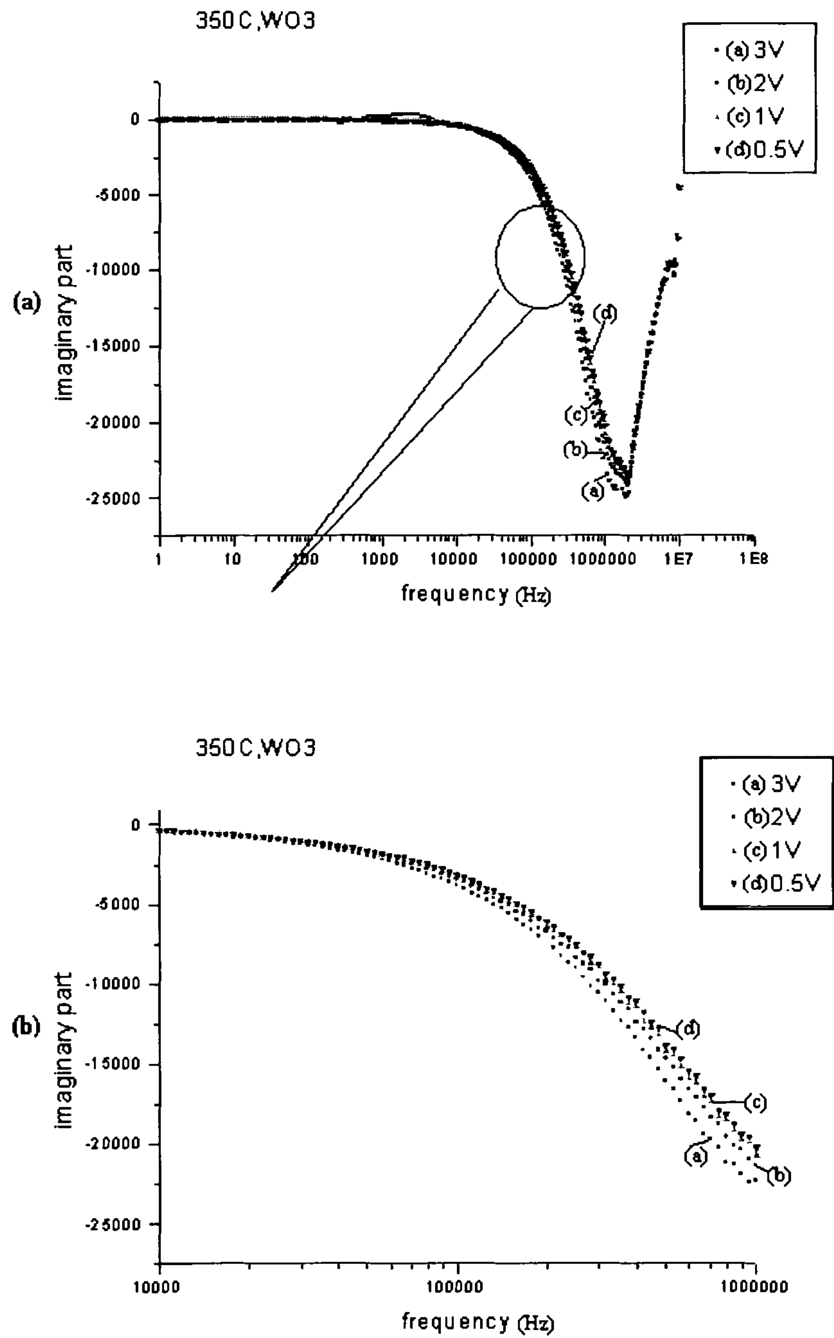

Figure 58: The imaginary part of the impedance of undoped WO_3 sensor as a function of frequency at different voltages. The temperature is 350°C.(a) full scale ,(b) zoomed part.

One can observe that at higher frequency, there are some changes for both the real and the imaginary parts of the impedances at different voltages.

4.8 Experimental Results Discussion and the Comparison with Theory for the I/V Characteristics of WO_3 Films

4.8.1 Discussion

In Chapter 2, a simplified equivalent circuit model of an SMO sensor (see Figure 25) is given. But from Figure 35, the actual electrode structure used for the present work is interdigital electrodes instead of a simple two-electrode structure. According to the actual structure, the equivalent circuit is represented as in Figure 59. It actually consists of 6 parallel branches. In order to make some simplification one can assume that all the branches are identical. Considering the case of one branch, if one applies a total voltage *V* across it, one obtains a current, *I*. Since these 6 branches are in parallel, if the total voltage applied is still *V*, one should expect the same current *I* will flow through each of the branches and the total current for the whole network should be *6I*. If the conduction between each electrode pair is the same, one can still use the equivalent circuit as in Figure 25. The only differences are the diodes represent the parallel combination of 6 diodes and the film resistance between the individual IDTs is 1/6th of the film resistance.

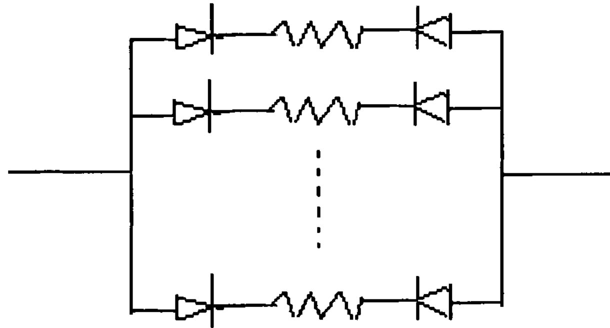

Figure 59: The equivalent circuit model for the sensor structure shown in Figure 35.

As mentioned before, there are four major carrier transport mechanisms that may occur between the metal and n-type semiconductor, namely, thermionic emission, drift and diffusion and tunneling. Since the donor concentration(oxygen vacancies) in the film is quite high, carrier transport via drift and diffusion does not occur(see section 2.3.3). The key factor which determines whether thermionic emission or tunneling takes place is the depletion width between the metal and semiconductor. For high donor concentrations (see equation(32)) tunneling probably occurs while for lower donor concentration thermionic emission occurs. Therefore the donor concentration of the semiconductor is an important film parameter that will determine the electron transport mechamism.

If one considers a two electrode configuration as shown in Figure 7, the current voltage relationship can be expressed as follows,

$$V = R_C I + f(I) + g(I) + h(I) \tag{48}$$

where the first term, $R_C I$, on the right hand side is the voltage across the crystallites , the second term, $f(I)$, is the voltage across the intercrystallite boundaries , the third term,

$g(I)$,is the voltage across the forward biased Schottky contact and the fourth term, $h(I)$,is the voltage across the reverse biased Schottky contact.

Electron transport between the IDTs can occur in several different ways. The electron transport between the metal semiconductor interfaces (MSI) and crystallite boundaries (CB) may be governed by thermionic emission, tunneling or combinations thereof. This gives rise to the following 4 possible scenarios:

(i) Thermionic emission for MSI and CB.

(ii) Tunneling for MSI and CB.

(iii) Thermionic emission for MSI and tunneling for CB.

(iv) Thermionic emission for CB and tunneling for MSI.

Since the respective depletion widths in CB (see equation 5; note $x_0 = \left[\frac{2V_s\varepsilon}{qN_D}\right]^{1/2}$) and MSI (see equation 32) are controlled by the donor concentration (oxygen vacancies in the film) scenarios (iii) and (iv) probably do not occur. Therefore only scenarios (i) and (ii) will be considered.

In the case of thermionic emission for MSI and CB, according to equation (13c), the voltage across the crystallite boundaries can be expressed as follows,

$$V_{CB} = \frac{kTn'L}{qwdMn_1}\exp\left(\frac{q\phi_b}{kT}\right)I = R_{CB}I. \tag{49}$$

where R_{CB} represents the total resistance for the crystallite boundaries. Equation (49) implies that the I/V characteristics of the crystallite boundaries is a linear function.

For the Schottky contact part, the reverse resistance is much larger than the forward resistance hence most of the voltage across the Schottky contacts will occur across the reverse biased contact. That means that one can ignore the *g(I)* term and only consider the *h(I)* term. According to equation (42) and note that for reverse bias V is negative and the resulting current should be negative, then the absolute value of reverse biased voltage should be as follows,

$$h(I) = |V_{RB}| = \left|\ln\left(-\frac{I}{I_0}+1\right)\right|\frac{nkT}{q}, \tag{50}$$

where I is the absolute value of the current and n is the ideality factor discussed in section 2.3.3. Noting that $R_C << R_{CB}$, $h(I) >> g(I)$ and substituting equations (49) and (50) into equation (48) one obtains,

$$V = R_{CB}I + h(I) = R_{CB}I + \left|\ln\left(-\frac{I}{I_0}+1\right)\right|\frac{nkT}{q}. \tag{51}$$

Since the electrode sensor configuration is symmetric, the I/V characteristics are symmetric with respect to the applied voltage, V, therefore resulting in the I/V characteristics having the general variation as shown in Figure 60.

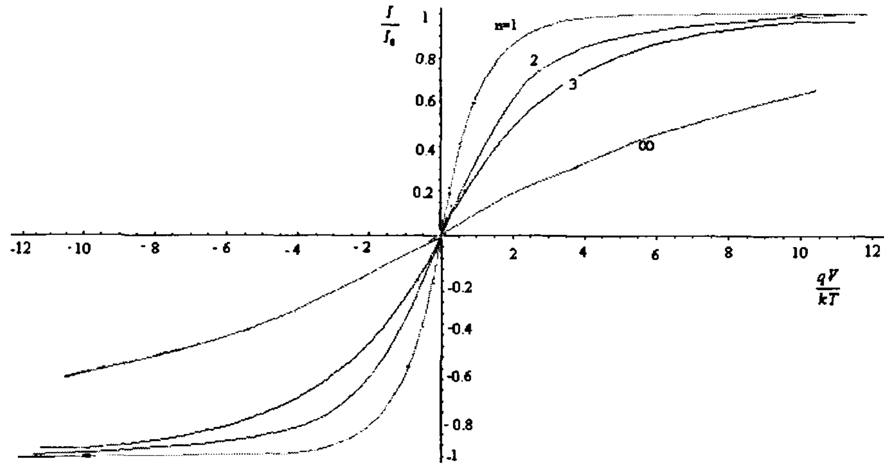

Figure 60: I/V characteristics based on thermionic emission theory. n is the ideality factor.

For the case of a heavily doped semiconductor a thin depletion width [refer to equation 32] occurs resulting in the electrons tunneling through the potential barrier. The second term in equation (48) is no longer a linear function and tunneling occurs. This results in an I/V characteristics for the crystallite boundaries (see equation 46) which can be expressed as follows,

$$I = I_{01}\left\{\exp\left(\frac{qV_{CB}}{nkT}\right) - \exp\left[\left(\frac{1}{n}-1\right)\frac{qV_{CB}}{kT}\right]\right\}. \tag{53}$$

where I_{01} is the saturation current and $V_{CB} = \frac{V}{N_1}$, is the voltage across the crystallite boundary and n is the ideality factor, typically greater than one according to the curve fitting results from Rideout and Crowell [26]. Choosing V_{CB} to be an absolute value,

one can ignore the second term since $\left[\left(\frac{1}{n}-1\right)\frac{qV_{CB}}{kT}\right] < 0$ and the second term is much smaller than the first term. The voltage across a single crystallite boundary can then be expressed as,

$$V_{CB} = f(I) = \frac{nkT}{q}\ln\left(\frac{I}{I_{01}}\right). \tag{54}$$

and the total voltage across all the crystallite boundaries becomes,

$$V = N_1 V_{CB} = N_1 \frac{nkT}{q}\ln\left(\frac{I}{I_{01}}\right). \tag{55}$$

For the forward biased Schottky contact, a similar form for the voltage drop across the forward voltage, V_{FB}, results, namely,

$$V_{FB} = g(I) = \frac{nkT}{q}\ln\left(\frac{I}{I_{02}}\right), \tag{56}$$

where I_{02} is the saturation current associated with the Schottky barrier.

For the reverse bias Schottky contact, the first term in equation (46) is much smaller than the second term since $\frac{-qV_{RB}}{nkT} < 0$ (noting that V_{RB} is the absolute value of reverse biased voltage). Neglecting the first term and solving for the reverse bias voltage, V_{RB} ,one obtains,

$$V_{RB} = h(I) = \frac{nkT}{q(n-1)}\ln\left(\frac{I}{I_{02}}\right), \tag{57}$$

where I is the absolute magnitude of the current.

For the tunneling effect, the contacts between metal semiconductor and crystallite boundaries are of low resistance (Rideout and Crowell[26]) and the term R_C for the resistance of the crystallite can not be neglected. Equation (48) then becomes

$$V = R_C I + N_1 V_{CB} + V_{FB} + V_{RB}. \tag{58}$$

Substituting equation (55)-(57) into equation (58) one obtains,

$$V = R_C I + \left[N_1 \frac{nkT}{q} \right] \ln\left(\frac{I}{I_{01}}\right) + \frac{kT}{q} \frac{n^2}{n-1} \ln\left(\frac{I}{I_{02}}\right). \tag{59}$$

In order to obtain the general variation of the I/V characteristics due to tunneling, one can assume $I_{01} = I_{02} = I_0$ resulting in the I/V characteristics shown in Figure 61.

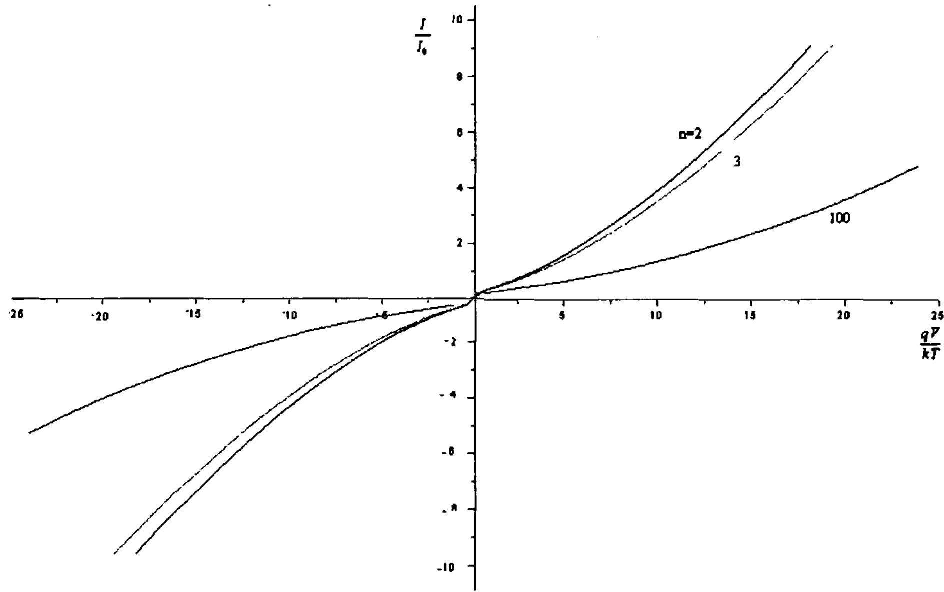

Figure 61: I/V characteristics based on the thermionic field emission (tunneling) theory.

As a result of the theory presented, two types of I/V characteristics are predicted, one based on thermionic emission(Figure 60) and one based on tunneling(Figure 61). For a similar range of applied voltages the I/V characteristics of both models are shown in Figure 62 for the same ideality factor.

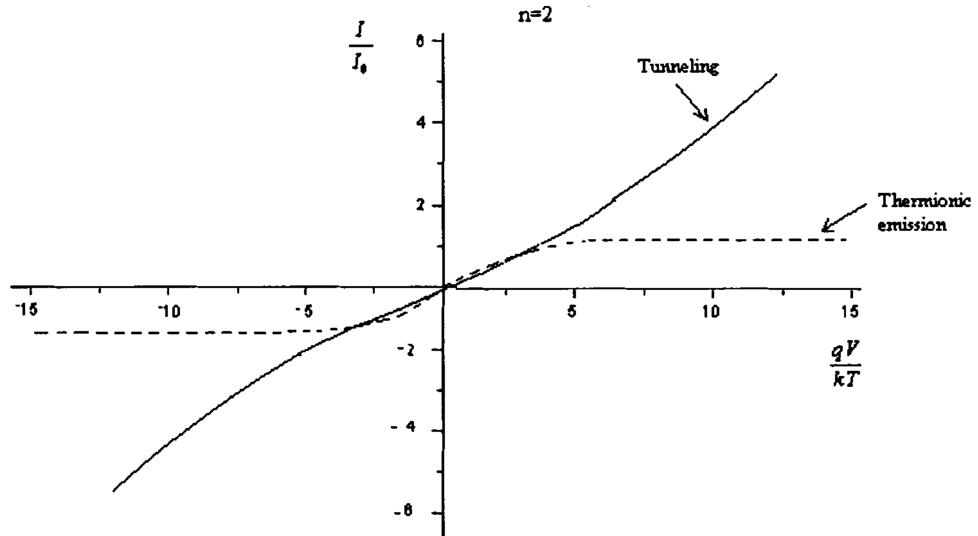

Figure 62: I/V characteristics of both models, solid line based on tunneling, dotted line based on thermionic emission. The ideality factor for both models is n=2.

Examing figure 62 one can easily differentiate the I/V characteristics of the two models for high voltages, however, for low voltages the variations are similar. However, if one uses ohm's law, $R = \frac{V}{I}$, the corresponding resistance versus voltage curve can be obtained and is shown in Figures 63 and 64 for the thermionic emission and tunneling models respectively. Note the resistance, R, is represented from Figures 61 and 62 as $qV/kT \big/ (I/I_0)$.

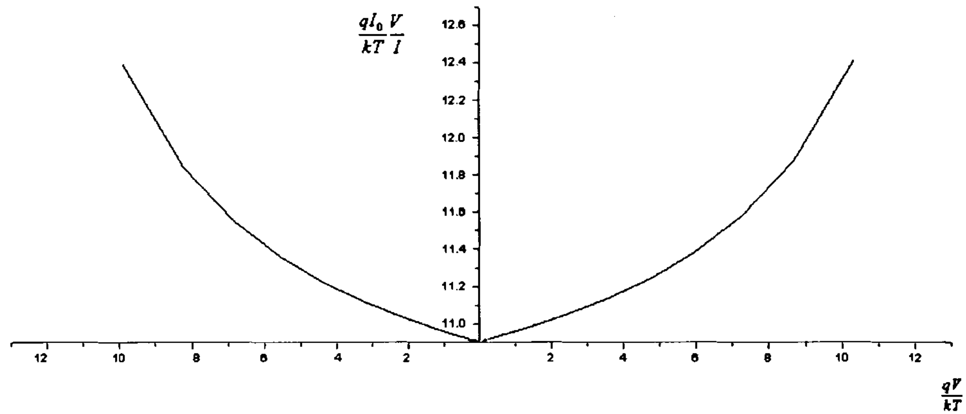

Figure 63: R/V characteristics based on the thermionic emission model.(n=2)

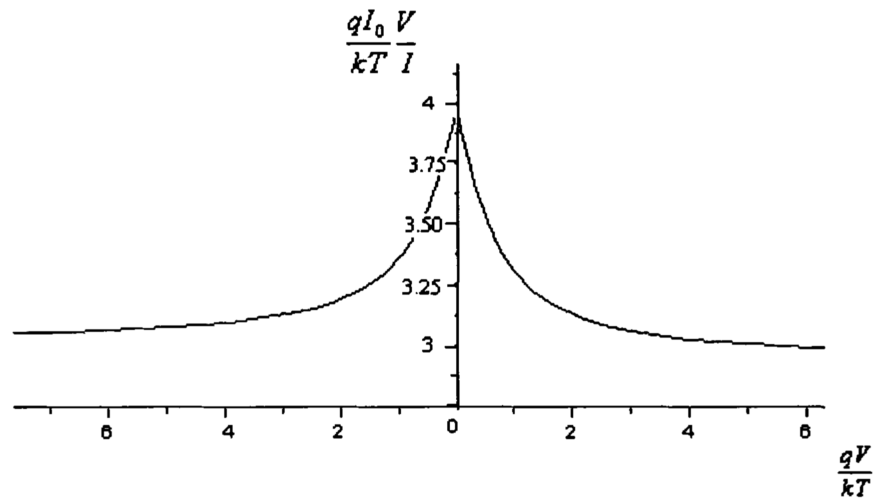

Figure 64: R/V characteristics based on the tunneling model.(n=2)

The R/V characteristics for each model are quite different. In particular from Figure 63 and 64, the resistance increases with increasing voltage based on the thermionic emission and the resistance decreases with increasing voltage based on tunneling effect. Clearly the R/V characteristics offer a sensitive measure as to which electron transport model is most appropriate.

4.8.2 Comparison of Experimental Results with Theory

The experimental data which was shown in the previous section are taken in synthetic air. Since air includes 20% oxygen, one should consider the effects of oxygen adsorption. When oxygen adsorbs on the crystallite surface the following reactions take place,

$$e^- + O_2 \Leftrightarrow O_2^-, \tag{60a}$$

and

$$\begin{aligned} O_2 &\Leftrightarrow 2O, \\ e^- + O &\Leftrightarrow O^- \end{aligned} \tag{60b}$$

The most predominate interaction is the formation of O^- on the surface represented by equation(60b). The O^- on the surface will change the barrier height [29] and could also affect the depletion width. That's the typically situation of metal oxide semiconductor. The observation that WO_3 acts as a selective oxidation catalyst [30] suggests that the concentration of O^- species on WO_3 at reactive temperature.

According to WO_3's molecular structure, if there is one oxygen vacancy in the WO_3 film, there are two free electrons which will contribute to the conductivity. Noting that $\sigma = ne\mu$, the following relationship between the oxygen vacancy concentration, N_d, n and σ result,

$$N_d \approx \frac{n}{2} = \frac{\sigma}{2e\mu}. \tag{61}$$

The experimental results presented in section 4.2 to 4.6 include the I/V characteristics of a gold-doped and undoped film exposed to compressed air and two

target gases. Each set of I/V curves are approximately close to a linear function except in the lower voltage region where it is nonlinear. Examining the experimental I/V characteristics represented in Figures 36,38,45,47a ,48 and 50a it is not clear as to whether the thermionic emission or tunneling effect model is most appropriate. However, if one examines the experimental R/V characteristics presented in Figures 37,39,46,47b,49 and 50b it is obvious that the variation of the experimental R/V characteristics is similar that shown in Figure 64. One then concludes that the tunneling model is the most appropriate model for electron transport in the semiconducting metal oxide sensor.

Since the tunneling is the dominant behavior, one can adjust the parameter R_C, I_{01}, I_{02}, n and N_1 according to equation (59) to get the best fit for the I/V characteristics. Figure 65 presents the fitting results of the I/V characteristics of undoped WO_3 at 200°C.[The experimental data was presented in Figure(48C)]

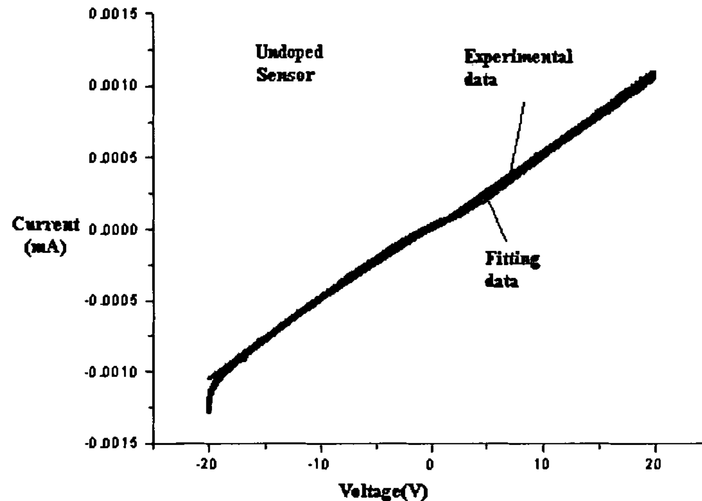

Figure 65: Comparison of the experimental and theoretical I/V curves for the undoped WO_3 sensor at 200°C.

Since the actual electrode structure is an IDT, one needs to take into consideration the parallel effect. The resistance of the crystallites, R_C, is 1/6 of the whole crystallite resistance and the other parameters represent the effect of the 6 parallel diodes.

Figure 66 shows the curve fitting for the R/V characteristics based on Figure 65.

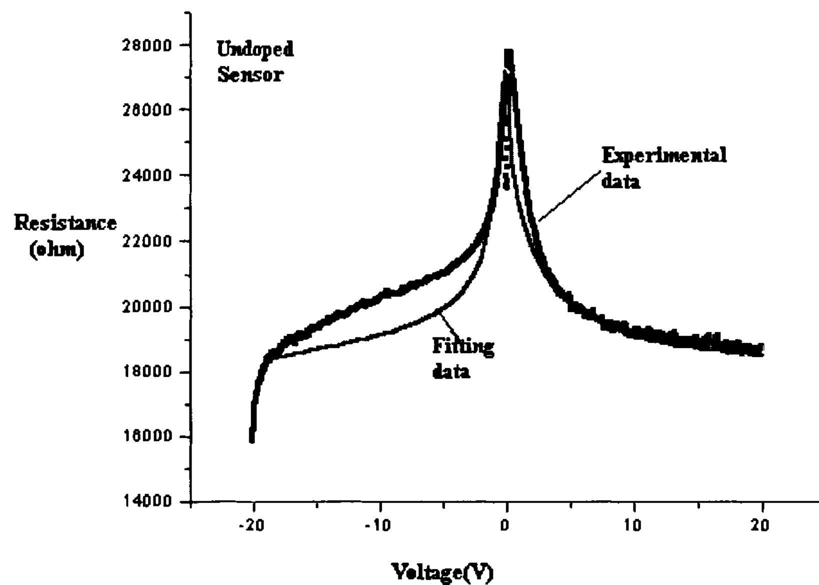

Figure 66: Comparison of the experimental and theoretical R/V curves for the undoped WO_3 sensor at 200°C.

Figure 67 presents the comparison of the I/V and R/V experimental and theoretical results for the gold-doped sensor at 200°C [The experimental data was presented in Figure(45C) and (46C)] . Figure 68 shows the comparison of the experimental and theoretical I/V and R/V results for the undoped sensor exposed to H_2S gas at 200°C [The experimental data was presented in Figure (48C) and (49C)] while Figure 69

shows a similar comparison for the gold-doped sensor exposed to H_2S gas at 200°C. [The experimental data was presented in Figure(45C) and (46C)].

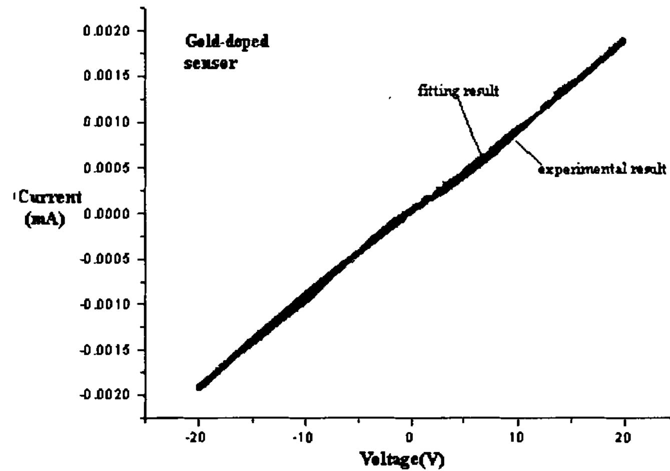

(a)

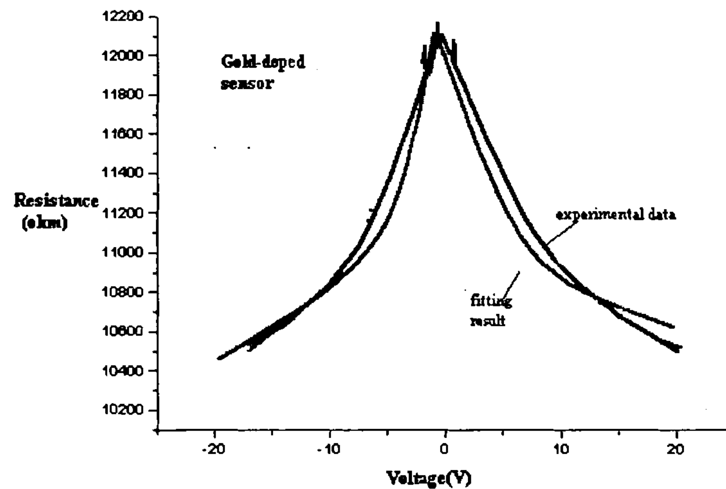

(b)

Figure 67: (a) Comparison of the experimental and theoretical I/V curves for the gold-doped sensor at 200°C. (b) the corresponding R/V comparison for the gold-doped sensor at 200°C.

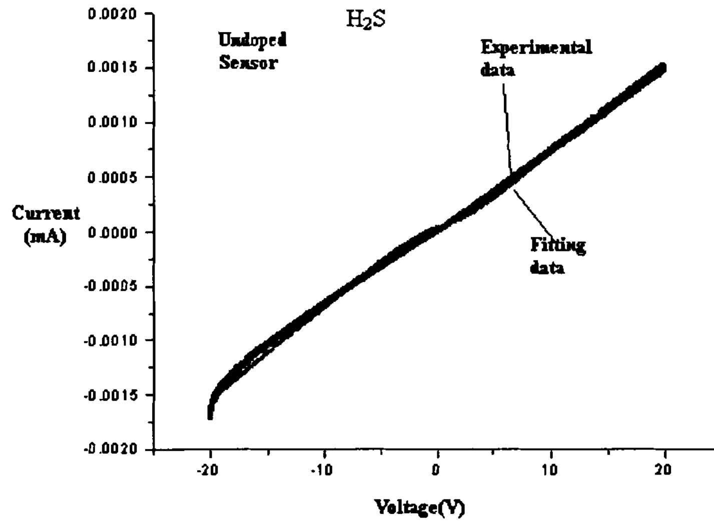

(a)

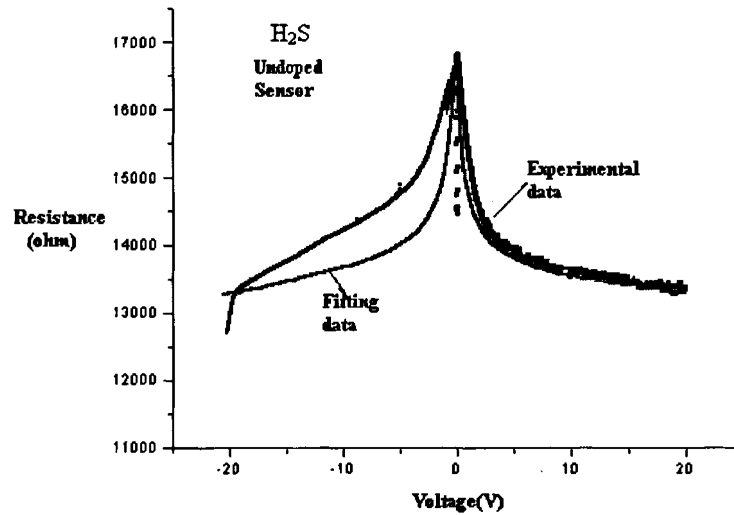

(b)

Figure 68: (a) Comparison of the experimental and theoretical I/V curves for the undoped sensor exposed to H_2S gas at 200°C. (b) the corresponding R/V comparison for the undoped sensor exposed to H_2S at 200°C.

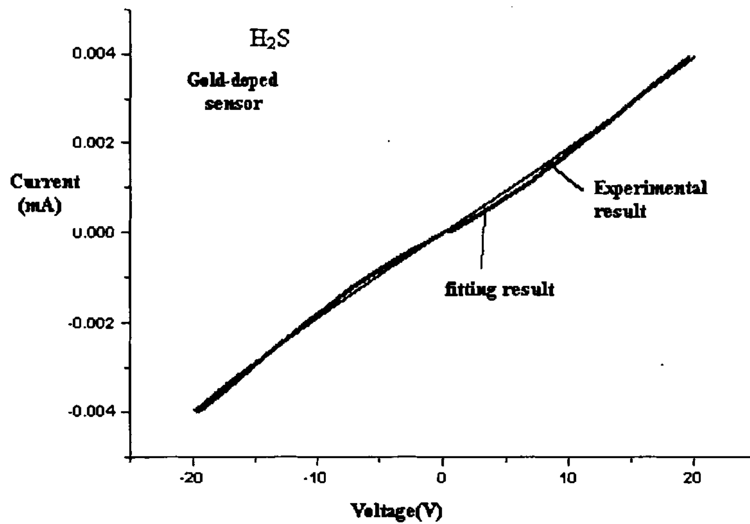

(a)

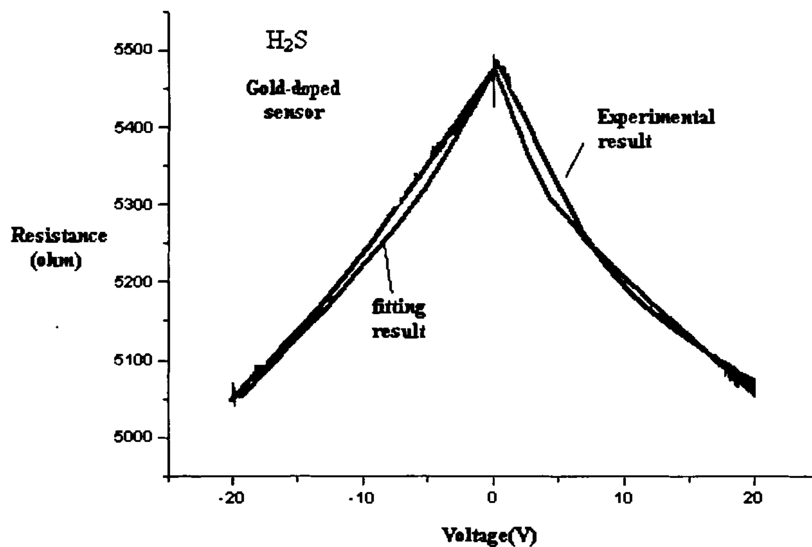

(b)

Figure 69: (a) Comparison of the experimental and theoretical I/V curves for the gold-doped sensor exposed to H_2S gas at 200°C. (b) the corresponding R/V comparison for the gold-doped sensor exposed to H_2S at 200°C.

Table 2 shows the fitting parameter for Figure 65 to 69.

Sensor	gas	T	I_{01}(A)	I_{02}(A)	n	N_1	R_c(ohm)
gold-doped	air	200°C	8.07E-07	1.93E-07	1.34	15	9458
gold-doped	H_2S	200°C	1.8E-06	2.1E-07	1.401	15	4776
undoped	air	200°C	3.64E-7	7.80E-06	1.798	17	20113
undoped	H_2S	200°C	5.97E-7	1.89E-7	1.883	17	13955

Table 2: Fitting parameters for Figures 65 to 69.

The curve fitting wasn't done for the ethylene gas since the experimental results were similar in shape to the curves associated with the H_2S gas exposures.

The fitting results were obtained using the build-in curve fitting tools in Origin. One defines your own function [equation (59) for the present work] and the built-in tool uses the least-square error method to fit the experimental results. For the present work, the $V>0$ part of the experimental result is used for curve fitting and since the supposed geometry is symmetric, the I/V and corresponding R/V curve should be symmetric. Since the actual device may be not exactly symmetric, the fitting results may cause some deviation for the $V<0$ part of the experimental results.

The experimental results clearly confirm that the electron transport model is tunneling. The experimental results are not only similar in shape to the theoretical results but also the theoretical model can be shown to fit the experimental results quite well. In particular for the I/V characteristics the fit is extremely close while for the R/V characteristics only minor deviations occur at low voltages. Deviations occurring for $V<0$ were due to the fact that the geometry was not exactly symmetric due to the resolution of manufacturing process and the curve fitting was done for $V>0$ results. Deviations may also be attributed to the fact that the parameters I_{01}, I_{02} and n

may be slightly dependent upon voltage, temperature and film parameters such as donor concentration and number of crystallites. In the present case these parameters are treated as being constant.

5. SUMMARY, CONCLUSIONS AND FUTURE WORK

5.1 Summary

The current versus voltage characteristics of undoped and gold –doped WO_3 thin film sensors were studied both experimentally and theoretically. A one channel gas delivery system was built to determine the I/V characteristics. The voltage range for the tests was from –20V to 20V and the temperature range was from room temperature to 400°C. The experimental results for the I/V characteristics were taken in compressed air and in two different target gases, hydrogen sulfide(H_2S) and ethylene(CH_2). The experimental results show that the I/V characteristics are linear at high voltages and nonlinear at lower voltages for both the doped and undoped sensors under different gas exposures. In addition to the I/V characteristics, the corresponding R/V characteristics were also examined in both compressed air and the same target gases as the I/V characteristics. The experimental results show that the resistance is higher in the lower voltage region and lower in the high voltage region. The resistance versus temperature characteristics were examined using the gold-doped film and undoped film. The range of temperature was room temperature to 400°C and the examination voltage was 2.5Volts. The experimental result shows that the resistance decreases with increasing temperature for the undoped WO_3 thin film sensor while this is not true for the gold-doped sensor. The resistance of the gold-doped sensor decreases with increasing temperature until around 200°C, after that it increases with increasing temperature. For both of the sensors, there is no hysteresis behavior. This is due to species' adsorption and desorption processes on the surface.

The sensitivity of the WO_3 sensor was also examined for H_2S and ethylene target gases. The sensitivity data of the gold-doped sensor exposed to 5PPM H_2S show that the sensitivity increases from 4% to around 70% with increasing temperature from room temperature to 300°C. Similar sensitivity data taken using undoped sensors show that the sensitivity of undoped sensor is lower than the gold-doped sensor. For the 5PPM ethylene target gas, the sensitivity data of the gold-doped sensor shows that the sensitivity increases from 60% to 90% with increasing temperature from 200°C to 400°C. When one decreases the ethylene concentration from 5PPM to 1PPM, the sensitivity decreases and the range is from 35% to 50% with increasing temperature from 200°C to 400°C.

Three theoretical models were presented to describe the carrier transport mechanisms between the metal and semiconductor interfaces and intercrystallite boundaries. The first one is the drift and diffusion model which is suitable for wide depletion widths ($>10^{-4}$cm). The second one is the thermionic emission model which is appropriate when the depletion region is moderate (compared to the electron mean free path). In this case the electrons have enough energy to go over the potential barrier. The third one is the thermionic field emission (tunneling effect model)which is applicable for very thin depletion widths (less than 100Å) . In this case electrons are treated as waves and will tunnel through the potential barrier instead of jumping over the potential barrier. These transport mechanisms were discussed in detail and the I/V characteristics based on each of the models were presented.

According to the structure of the WO_3 sensor, a simplified equivalent circuit was formulated. It includes forward and reverse biased Schottky diodes which

represent the contact region between the electrodes and the film and a resistor which represent the sum of crystallite resistance and the intercrystallite resistance between the individual crystallites.

The actual electrode structure used for the present work is interdigital electrodes instead of a simple two-electrode structure. It actually consists of 6 parallel branches. If the conduction between each electrode pair is the same, one can still use the simplified equivalent circuit. The only differences are the diodes represent the parallel combination of 6 diodes and the film resistance between the individual IDTs is 1/6th of the film resistance.

In addition to the I/V measurement in the DC case, preliminary work also was done on I/V characteristics in the AC case. The experimental data shows that there are obvious changes for both the real and the imaginary parts of the impedances as one varies voltage and frequency.

According to the electron transport mechanisms through the boundaries (M/S and intercrystallite boundaries) and the crystallites, two kinds of I/V and corresponding R/V characteristics were predicted, one based on thermionic emission theory and the other based on tunneling theory. The I/V experimental results are approximately close to a linear function except in the lower voltage region where it is nonlinear. The R/V results are more sensitive and nonlinear.

Finally, the theoretical results are carefully compared to the experimental results for both the I/V and R/V characteristics and conclusions were drawn as to what model was the most appropriate for electron transport through the semiconducting metal oxide sensor.

5.2 Conclusions

Comparing the experimental results of the I/V characteristics and the corresponding R/V characteristics taken in synthetic air or target gases such as H_2S with the theoretical curve predicted by thermionic emission and tunneling theories, it is obvious that the tunneling effect is the dominant electron transport mechanism in the WO_3 thin film sensor. Each set of I/V experimental results are approximately close to a linear function except in the lower voltage region where it is nonlinear. The corresponding R/V results are more sensitive which clearly show the nonlinear relationship. According to the structure of the thin film sensor, the crystallite resistance is a constant value. The part that causes the nonlinear behavior is the boundaries which include the metal semiconductor (M/S) interfaces and the boundaries between the crystallites.

The depletion width is the key parameter which determines which transport mechanism is most applicable between the boundaries. By controlling the argon oxygen ratio in the R-F magnetron sputtering process one can change the oxygen vacancy concentration and hence the donor concentration. Since the depletion width depends upon the donor concentration one can adjust the depletion width of the film by precisely controlling the argon oxygen ratio. This will in turn determine the behavior of the I/V and R/V characteristics. In principle this will allow one to apriori design a semiconducing metal oxide sensor and predict the behavior of the I/V and R/V characteristics.

In the case of target gases, they will interact with the film and change the film conductivity, barrier heights between the M/S boundaries and intercrystallite

boundaries and could also affect the depletion width. In the present work, however target gases and/or oxygen does not change the behavior of the I/V and R/V characteristics. The experimental results clearly show that tunneling is the possible electron transport mechanism in the metal-semiconductor and crystallite boundaries.

All the SMO sensors used in the present work were annealed in dry air at 400°C for 24 hours. The annealing process stabilizes the film in terms of the structure and electrical properties. The structure of the film is polycrystalline after the annealing process. According to the experimental results of resistance versus temperature and the I/V curves taken at different temperatures one can conclude that the temperature will change the donor concentration and carrier mobility in the film. Since the crystallite resistance directly depends upon the donor concentration and carrier mobility, the temperature will definitely change the crystallite resistance. For the crystallite boundaries and the interface between metal and semiconductor (M/S) the temperature will also change the depletion width due to the fact that the donor concentration of the film is temperature dependent. The different temperature used in the present work however did not affect the I/V and R/V characteristics significantly.

The Sensitivity is another interesting parameter to examine. According to the I/V and the corresponding R/V characteristics examined in H_2S and ethylene one can see clearly that the reducing target gases will interact with the film and cause the resistance to decrease. In addition one can also observe that the variation of the resistance in the lower voltage region is much bigger than that in the higher voltage region. According to the definition of sensitivity one could conclude that the lower

voltage region is the most sensitive region for both H_2S and ethylene gas detection using the WO_3 thin film sensor.

5.3 Future Work

Although the present work represents significant research on the I/V and R/V characteristics of undoped and gold-doped WO_3 under different temperatures and gas exposures, many questions still remain unanswered. These questions are related to both theory and experiments.

(i)Amorphous film studies.

Since polycrystalline films were used for the present work, one can not neglect the effect of crystallite boundaries. However if the amorphous films were used the effect of the crystallite boundaries will be eliminated. The equivalent circuit will be simpler and the only nonlinear component to be considered is the M/S contacts. As a result one would obtain a simple sensor structure one may use for applications. Also one could explore in more depth the M/S junction behavior.

(ii) Schottky device study

More research should be done on the electron transport mechanisms at the metal semiconductor junction which includes both the forward and reversed biased junctions. In particular Schottky devices designed specifically for sensing should be fabricated. Doping levels in the metal oxide should be varied in order to obtain Schottky device in which thermionic or tunneling occurs. The advantage and disadvantages of these prototype sensors should be studied in detail. The effect of

contacts should also be considered and both amorphous and polycrystalline films should be deposited. An example of a contact variation would be a single electrode for one contact and a point contact for the other. This would ensure that only one significant M/S junction would occur. Positive results on this type of sensor could result in a entirely novel sensor configuration which would be distinctly different than the Schottky sensors and variations introduced by Lundstrom et al.[30]

(iii)Studies using different Ar/O_2 ratio and annealing process.

If one precisely changes the Ar/O_2 ratio in the film deposition process, one can get different donor concentration levels. Since the width of the depletion region depends upon the donor concentration one can change the depletion width by changing the Ar/O_2 ratio. Since the depletion width is a key factor to determine the I/V characteristics one can actually get the desired I/V characteristics by changing the Ar/O_2 ratio. Extensive studies should be presented for different Ar/O_2 ratio of a prototype sensor which have two point contacts and a polycrystalline film. In this case the dominant nonlinearity would be introduced by the crystallite boundaries. Prototype sensors should be made in which careful control of electron transport by doping and crystallite size by annealing are studied. Possible novel sensors may result from these studies.

(iV) Equivalent circuit model and electrode configuration

The electrodes configuration used for the present work is interdigital electrodes. The equivalent circuit model one used in the present work is correct if one assumes that all the interdigital fingers are exactly the same. In reality, it is not easy to get all the interdigital fingers exactly the same. More fingers result in more

asymmetry. In order to simplify the problem, one should consider a two-electrodes case. The two electrode configuration is simpler and one can get a better understanding and the curve fitting using the equivalent circuit will be more realistic. Another issue is the separation between the electrodes, one can change the separation of the electrodes and see the difference of I/V characteristics.

(V) AC studies

The present work barely scratches the surface relative to AC studies. In the present work significant research has been performed on the I/V and R/V characteristics at DC (zero frequency). Extensive studies at different frequencies are needed. It was shown that both the magnitude and phase of impedance varies as a function of both temperature and frequency. Extensive studies relating to the dependence of impedance on not only temperature and frequency but also voltage amplitude should be performed. In the AC case capacitive effects at M/S junctions and crystallite boundaries will appear. These effects may be more significant in different frequency ranges. This work, although extensive,may result in a novel class of impedance based sensor which would have sensor properties far superior to any presently known sensor. For example, one may envision a single sensor in which a frequency range may be tuned to be selective to a particular gas.

Finally, some general comments will be made relative to the possible future sensors. The present work points to the following future sensors,

(i) Apriori design of a DC semiconducting metal oxide sensor in which I/V and R/V characteristics can be predicted.

(ii) Development of a novel class of Schottky sensors.

(iii) Development of a novel class of impedance based sensors.

The number of specific problems and research topics in each of these three types of sensors is numerous and involves both theoretical and /or experimental work.

REFERENCES

[1] W.H.Brattain and J.Bardeen, "Surface Properties of Germanium", Bell Syst. Tech. J., 32 (1953)1.

[2] T.Seiyama, A.Kato, K.Fujiishi and M.Negatani, Anal.Chem.34, (1962)1502.

[3] T.Seiyama and S.Kagawa, Anal.Chem. 38, (1966) 1069.

[4] J.Janata and M. Josowicz, Anal. Chem. 70 (1998) 179R-208R.

[5] N.Taguchi, US Patent 3,625,756 (Dec. 1971).

[6] Z.Xu, J.F.Vetelino, R.Lec and D.C.Parker, J.Vac.Sci.Technol. A8, (1990) 3634.

[7] Z.Xu, "Electrical Properities of Thin Tungsten Trioxide Films", MS Thesis, Electrical Engineering,University of Maine(1990).

[8] T. Tshihara, H. Fujita and Y. Takita , Sensors and Actuators B, 52(1998)100-106.

[9] R.Lalauze, C.Pijolat, S.Vincent and L.Bruno, Sensors and Actuators B, 8(1992) 237-243.

[10] U.Weimar and W. Göpel, Sensors and Actuators B, 26-27(1995)13-18.

[11] J.Cutierrez, L.Ares, J.I.Robla, M.C.Horillo, I.Sagago, J.Agapito, and L.Lopez, Sensors and Actuators B, 4 (1991)359.

[12] H.Nemoto and I.Oda, Adv.Ceram. 2, (1981) 167.

[13]L. L.Kazmerski, Polycrystalline and Amorphous Thin and Films and Devices(1980), Academic Press, A subsidiary of Harcourt Brace Jovanovich, Publishers.

[14] M.J.Cohen, J.S. Harris, and J.R.Waldrop, Proc. GaAs Conf., St.Louis. Inst. Phys. Conf. Ser.45, (1979) 263.

[15]N.F.Mott and R.W.Gurney, Electronic Processes in Ionic Crystals, Oxford, New York(1940)Chap.5, Eq.30.

[16] W.Schottky and E.Spenke, "Quantitative Treatment of the Space Charge and Boundary-layer Theory of the Crystal Rectifier", Wiss.Veroff.siemens-Werken 18, (1939) 225-291.

[17] A.Beiser, Concepts of Modern Physics 5th Ed. NewYork: McGraw Hill, (1995)309.

[18] D. Sauer and E. M. Stuve, Changes in Work Function, http://www.mcallister.com/papers/stuve.html.

[19] D.A.Buchanan and H.C.Card, "On the Dark Current in Germanium Schottky-Barrier Photodetectors", IEEE Trans.Electron Devices ED-29, (1982) 154-157.

[20] B.L.Sharma, Metal-Semiconductor Schottky Barrier Junctions and Their Applications. 27, New York: Plenum Press (1984).

[21] John F.Vetelino,Solid State Electronics,University of Maine, (1982) 151.

[22] John.F.Vetelino, Solid State Electronics, University of Maine,(1982)196-219.

[23] S.M.Sze, Physics of Semiconductor Devices (1969) New York,Wiley-Interscience. (1969)381-383.

[24] H.A.Bethe, "Theory of the boundary layer of crystal rectifiers", MIT Radiation Laboratory Report 12-43(1942).

[25] C.R.Crowell and V.L.Rideout, Solid-St.Electron,12, (1969) 89.

[26] W.A.Harrison, Phys.Rev. 123,(1961) 85.

[27] U. Weimar, W.Gopel, "A.C. measurements on tin oxide sensors to improve selectivities and sensitivities", Sensors and Actuators B 26-27(1995) 13-18.

[28] G. Bernhardt, C.Silvestre, N.LeCursi, S. Moulzolf, D.Frankel, K.Chung and R.J.Lad , Int.Meeting on Chemical Sensors, Sensors and Actuators, Basel, Switzerland, (2000) 368-374.

[29] W.Shockley, Phys.Rev. 56, (1939) 317.

[30] M.CHE, "Charaterization and Reactivfity of Mononuclear Oxygen Species on Oxide Surfaces", Advances in Catalysis, Volume 31(1983).

[30] I.Lundstrom, M.Armgarth,A.Spetz and F.Winquist, Sensors and Actuators, 10(1986)399-421.

APPENDIX A: Deviation of Diffusion Theory (Equation 38)

The diffusion theory is derived from the assumptions that (1) the barrier height is much larger than kT;(2) the effect of electron collisions within the depletion region is included and (3) the carrier concentration at $x=0$ and $x=W$ are unaffected by the current flow.

Since the current in the depletion region depends on the local field and the concentration gradient, the current density equation is follows,

$$J_n = q\left[n(x)\mu E + D_n \frac{\partial n}{\partial x}\right]. \qquad \text{(A-1)}$$

Since the mobility can be expressed in terms of the diffusion coefficient, D_n, using the Einstein relation, $\mu = qD_n/kT$ and $E = -\partial V(x)/\partial x$, equation(A-1) can be transformed into

$$J_n = qD_n\left[-\frac{qn(x)}{kT}\frac{\partial V(x)}{\partial x} + \frac{\partial n}{\partial x}\right]. \qquad \text{(A-2)}$$

Under the steady-state condition, the current density is independent of x, and (A-2) can be integrated using $exp[-qV(x)/kT]$ as an integrating factor. One can obtain

$$J_n \int_0^W \exp\left[-\frac{qV(x)}{kT}\right]dx = qD_n \int_0^W \left[-\frac{qn(x)}{kT}\frac{\partial V(x)}{\partial x}\exp\left(-\frac{qV(x)}{kT}\right) + \frac{\partial n}{\partial x}\exp\left(-\frac{qV(x)}{kT}\right)\right]dx$$

$$= qD_n \int_0^W \left\{n(x)\exp\left(-\frac{qV(x)}{kT}\right)' + n(x)'\exp\left(-\frac{qV(x)}{kT}\right)\right\}dx$$

$$= qD_n \int_0^W \left[n(x)\exp\left(-\frac{qV(x)}{kT}\right)\right]' dx$$

$$= qD_n \left\{n(x)\exp\left[-\frac{qV(x)}{kT}\right]\right\}_0^W$$

(A-3)

Referring to equation (30) and (31), one can get

$$qV(W) = 0,$$
$$qV(0) = -q(V_i - V). \qquad \text{(A-4)}$$

Referring to equation (26) and figure 19, one can get

$$n(W) = N_c \exp\left(-\frac{q\phi_n}{kT}\right),$$
$$n(0) = N_c \exp\left(-\frac{q\varphi_B}{kT}\right). \qquad \text{(A-5)}$$

where $x=0$ is in the metal and n-type semiconductor boundary and $x=W$ is in the bulk of semiconductor.

Substitution of equation (17), (A-4) and (A-5) into equation (A-3) yields

$$J_n = qN_c D_n \left[-\exp\left(\frac{-qV}{kT}\right)+1\right]\exp\left(-\frac{q\phi_B}{kT}\right)\exp\left(\frac{qV_i}{kT}\right) / \int_0^W \exp\left[-\frac{qV(x)}{kT}\right]dx.$$

(A-6)

According to equation (30), the potential distribution can be expressed as ,

$$qV(x) = q\phi(x) = -\frac{qN_d}{2\varepsilon}W^2\left(1-\frac{x}{W}\right)^2 = -\frac{qN_d}{2\varepsilon}(W-x)^2 = -\frac{qN_d}{2\varepsilon}W^2 + \frac{q^2 N_d}{\varepsilon}\left(Wx - \frac{x^2}{2}\right)$$

(A-7)

Substituting (A-7) into equation (A-6) and expressing W in terms of V_i-V (equation 32) one obtains,

$$J_n = \frac{qN_cD_n\left[-\exp\left(-\frac{qV}{kT}\right)+1\right]\exp\left(-\frac{q\phi_B}{kT}\right)\exp\left(\frac{qV_i}{kT}\right)}{\int_0^W \exp\left[\frac{qN_d}{2\varepsilon kT}W^2 - \frac{q^2N_d}{kT\varepsilon}\left(Wx - x^2/2\right)\right]dx}$$

$$= \frac{qN_cD_n\left[-\exp\left(-\frac{qV}{kT}\right)+1\right]\exp\left(-\frac{q\phi_B}{kT}\right)\exp\left(\frac{qV_i}{kT}\right)}{\exp\left[\frac{qN_d}{2\varepsilon kT}W^2\right]\int_0^W \exp\left[-\frac{q^2N_d}{kT\varepsilon}\left(Wx - x^2/2\right)\right]dx}$$

$$= \frac{qN_cD_n\left[-\exp\left(-\frac{qV}{kT}\right)+1\right]\exp\left(-\frac{q\phi_B}{kT}\right)\exp\left(\frac{qV_i}{kT}\right)}{\exp\left(\frac{qV_i}{kT}\right)\exp\left(\frac{-qV}{kT}\right)\int_0^W \exp\left[-\frac{q^2N_d}{kT\varepsilon}\left(Wx - x^2/2\right)\right]dx}$$

$$= \frac{qN_cD_n\left[\exp\left(\frac{qV}{kT}\right)-1\right]\exp\left(-\frac{q\phi_B}{kT}\right)}{\int_0^W \exp\left[-\frac{q^2N_d}{kT\varepsilon}\left(Wx - x^2/2\right)\right]dx}$$

(A-8)

For the denominator, the second term can be dropped since the linear term is dominant because $x<<W$, then J_n can be approximated as,

$$J_n = \frac{qN_cD_n\left[\exp\left(\frac{qV}{kT}\right)-1\right]\exp\left(-\frac{q\phi_B}{kT}\right)}{\int_0^W \exp\left[-\frac{q^2N_d}{kT\varepsilon}Wx\right]dx}$$

$$= \frac{qN_cD_n\left[\exp\left(\frac{qV}{kT}\right)-1\right]\exp\left(-\frac{q\phi_B}{kT}\right)}{-\frac{kT\varepsilon}{q^2N_dW}\left[\exp\left(-\frac{q^2N_dW^2}{kT\varepsilon}\right)-1\right]} = \frac{qN_cD_n\left[\exp\left(\frac{qV}{kT}\right)-1\right]\exp\left(-\frac{q\phi_B}{kT}\right)}{\frac{kT\varepsilon}{q^2N_dW}\left[1-\exp\left(-\frac{2q(V_i-V)}{kT}\right)\right]} \quad \text{(A-9)}$$

$$= \frac{q^2D_nN_c}{kT}\left[\frac{q(V_i-V)2N_d}{\varepsilon_s}\right]^{1/2}\exp\left(-\frac{q\phi_B}{kT}\right)\left\{\frac{\exp\left(\frac{qV}{kT}\right)-1}{1-\exp\left[-\frac{2q(V_i-V)}{kT}\right]}\right\}.$$

Since $q(V_i-V)>>kT$ is one of the conditions on which the present theory is based, the exponential term in the demoninator can be neglected for all reverse reverse voltage and for all small forward voltages, equation (A-9) reduces to

$$J_n \approx \left\{\frac{q^2 D_n N_c}{kT}\left[\frac{q(V_i - V)2N_d}{\varepsilon_s}\right]^{1/2} \exp\left(-\frac{q\phi_B}{kT}\right)\right\}\left[\exp\left(\frac{qV}{kT}\right)-1\right] = I(0)\left[\exp\left(\frac{qV}{kT}\right)-1\right],$$

(A-10)

where

$$I(0) = \left\{\frac{q^2 D_n N_c}{kT}\left[\frac{q(V_i - V)2N_d}{\varepsilon_s}\right]^{1/2} \exp\left(-\frac{q\phi_B}{kT}\right)\right\}.$$

(A-11)

The absolute value of electric field at the metal semiconductor interface, E_m, can be obtained from equation (29) or expressed aS

$$E_m = \frac{qN_d}{\varepsilon}W = \left[\frac{q(V_i - V)2N_d}{\varepsilon_s}\right]^{1/2}.$$

(A-12)

yielding

$$J_n = q\mu E_m N_c \exp\left(-\frac{\phi_B}{kT}\right)\left[\exp\left(\frac{qV}{kT}\right)-1\right]. \quad \text{(A-13)}$$

APPENDIX B: Deviation of Equation (39)

The thermionic emission theory is derived from the assumption that (1) the barrier height is larger compared to KT, (2)electron collisions within the depletion region are neglected.

Assuming that the electrons inside the semiconductor have a Maxwell-Boltzmann distribution function

$$f(E) = \exp\left[\frac{(E_f - E)}{kT}\right]. \quad \text{(B-1)}$$

Since $E = m^*(V_x^2 + V_y^2 + V_z^2)/2$ one can obtain the velocity distribution function from (B-1),

$$f_V = A_V \exp\left[-\frac{m^*(V_x^2 + V_y^2 + V_z^2)}{2kT}\right]. \quad \text{(B-2)}$$

The normalization constant , A_V, is found from the condition

$$\int_{-\infty}^{\infty}\int_{-\infty}^{\infty}\int_{-\infty}^{\infty} f_V dV_x dV_y dV_z = 1. \quad \text{(B-3)}$$

Substitute (B-2) into (B-3) and using the following relation (which can be found in any table of integrals)

$$\int_{-\infty}^{\infty} \exp(-ax^2)dx = \left(\frac{\pi}{a}\right)^{1/2}. \quad \text{(B-4)}$$

one obtains

$$f_V = \left[\frac{m^*}{2\pi kT}\right]^{3/2} \exp\left[-\frac{m^*(V_x^2 + V_y^2 + V_z^2)}{2kT}\right]. \quad \text{(B-5)}$$

One can also rewrite this expression as

$$f_V = f_{Vx} f_{Vy} f_{Vz}, \tag{B-6}$$

where f_{Vx}, f_{Vy} and f_{Vz} are the distribution functions for velocity components V_x, V_y and V_z respectively.

$$f_{Vy} = \left[m^* / 2\pi kT \right]^{1/2} \exp\left[-m^* V_z^2 / 2kT \right]. \tag{B-7}$$

$$f_{Vy} = \left[m^* / 2\pi kT \right]^{1/2} \exp\left[-m^* V_y^2 / 2kT \right]. \tag{B-8}$$

$$f_{Vz} = \left[m^* / 2\pi kT \right]^{1/2} \exp\left[-m^* V_z^2 / 2kT \right]. \tag{B-9}$$

The average velocity $\langle V_x \rangle$ of electrons moving in the x direction which is perpendicular to the interface is,

$$\begin{aligned} \langle V_x \rangle &= \int_0^\infty V_x f_{Vx} dV_x = \left[m^* / 2\pi kT \right]^{1/2} \int_0^\infty V_x \exp\left[-m^* V_x^2 / 2kT \right] dx \\ &= \left[2kT / \pi m^* \right]^{1/2} \int_0^\infty V_x \exp(-V_x^2) dx = \left[kT / 2\pi m^* \right]^{1/2}. \end{aligned} \tag{B-10}$$

Using the same procedure, one can calculate the average electron velocity,

$$\langle V \rangle = \int_0^\infty V f_V d^3V = \left[8kT / \pi m^* \right]^{1/2} = 4 \langle V_x \rangle. \tag{B-11}$$

According to Figure 20, the minimum energy for electrons to exceed the height of the potential barrier is:

$$q\phi = q(V_i - V), \tag{B-12}$$

where V_i is the built-in potential of the junction and V is the applied voltage which can be V_F in the case of forward bias and V_R in the case of reverse bias. According to equation (26) the number of electrons, n* per unit area which have sufficient energy to move over the barrier from the semiconductor into the metal is as follows,

$$n^* = n_0 \exp\left(\frac{-q(V_i - V)}{kT}\right). \tag{B-13}$$

where n_0 repesents the electron concentration in the neutral semiconductor outside the depletion region. According to equation (26),

$$n_0 = N_c \exp\left[-\frac{\phi_n}{kT}\right].$$

and since $\phi_B=qV_i+\phi_n$ from equation (B-13) one can obtain

$$n^* = N_c \exp\left[-\frac{(\phi_B - qV)}{kT}\right]. \tag{B-14}$$

Supposing that all the incident electrons cross over into the metal and none is reflected back the current I_{SM} due to passing of electrons from the semiconductor to the metal is given by

$$I_{SM} = qn^* S\langle V_x \rangle = qn^* S\frac{\langle V \rangle}{4} = \frac{qS\langle V \rangle}{4} N_c \exp\left\{-\left(\frac{\phi_B - qV}{kT}\right)\right\}. \tag{B-15}$$

For unbiased junction under thermal equilibrium no net current can flow. Consequently the current given by (B-4) must be balanced by an opposite current I_{MS} due to crossing of electrons from the metal into the semiconductor making $I=I_{SM}+I_{MS}=0$ and

$$I_{MS} = -\frac{qS\langle V \rangle}{4} N_c \exp\left\{-\left(\frac{\phi_B}{kT}\right)\right\}. \tag{B-16}$$

In the presence of applied bias V, the barrier for electron flow from the metal to semiconductor remains practically unchanged at ϕ_B and so is the current $I_{MS}=-I_0$. The current I_{SM}, however, is given by equation (C-15) and combining this equation with equation(C-16) one obtains

$$I = I_0\left[\exp\left(\frac{qV}{kT}\right) - 1\right]. \qquad \text{(B-17)}$$

substituting $\langle V \rangle$ and $N_c=2(2\pi m^* kT/h^2)^{3/2}$ (referring to equation(24)) the current I_0 can be written as

$$I_0 = SAT^2 \exp\left[-\frac{\phi_B}{kT}\right], \qquad \text{(B-18)}$$

where
$$A = \frac{4\pi \mathrm{m}^* qk^2}{\mathrm{h}^3}.$$

BIOGRAPHY OF THE AUTHOR

Huilin Ren was born in Hangzhou, Zhejiang Province, the People's Republic of China, on February 24,1973. After graduation from Laiyang No.1 High School in 1992, she enrolled at the Shandong University of Technology, Jinan, China, and graduated in 1996 with a Bachelor's degree in Electrical Engineering. She began her graduate study at the University of Maine in January 1999.

Huilin Ren is a candidate for the Master of Science degree in Electrical Engineering from The University of Maine in August, 2001.